Spring 2021

Development of in-situ radiometric inspection methods for quality assurance in laser powder bed fusion

Cody S. Lough

DEVELOPMENT OF IN-SITU RADIOMETRIC INSPECTION METHODS FOR QUALITY ASSURANCE IN LASER POWDER BED FUSION

by

CODY SHANNON LOUGH

A DISSERTATION

Presented to the Graduate Faculty of the

MISSOURI UNIVERSITY OF SCIENCE AND TECHNOLOGY

In Partial Fulfillment of the Requirements for the Degree

DOCTOR OF PHILOSOPHY

in

MECHANICAL ENGINEERING

2021

Approved by:

James A. Drallmeier, Advisor
Edward C. Kinzel
Robert G. Landers
Douglas A. Bristow
Joseph W. Newkirk

PUBLICATION DISSERTATION OPTION

This dissertation consists of the following four articles, formatted in the style used by the Missouri University of Science and Technology:

Paper I, "In-Situ Optical Emission Spectroscopy of Selective Laser Melting," on pages 5–23 was published in *Journal of Manufacturing Processes*.

Paper II, "Correlation of SWIR Imaging with LPBF 304L Stainless Steel Part Properties," on pages 24–60 was published in *Additive Manufacturing*.

Paper III, "Local Prediction of Laser Powder Bed Fusion Porosity by Short-Wave Infrared Imaging," on pages 61–100 will be submitted to *Journal of Materials Processing Technology*.

Paper IV, "Rapid Thermal History Prediction for Laser Powder Bed Fusion by Experimentally Informed Superposition Model," found on pages 101–112 will be submitted to *Manufacturing Letters*.

ABSTRACT

Laser Powder Bed Fusion (LPBF) metal Additive Manufacturing (AM) fabricates 3D metal parts layer-by-layer. The process enables production of geometrically complex parts that are difficult to inspect with traditional methods. The LPBF parts experience significant geometry driven thermal variations during manufacturing. This creates microstructure and mechanical property inhomogeneities and can stochastically cause defects. Mission critical applications require part qualification by measuring the defects non-destructively. The layer-to-layer nature of LPBF permits non-intrusive measurement of radiometric signals for a part's entire volume. These measurements provide thermal features that correlate with the local part health. This research establishes Optical Emission Spectroscopy (OES) and Short-Wave Infrared (SWIR) imaging radiometric inspection methods that infer the final material state in LPBF. The instruments' signals are correlated with bulk and local part properties to evaluate prediction capabilities. A probability framework defines the SWIR camera's local defect detection successes and limitations. Finally, a superposition thermal model based on SWIR data predicts laser scan path driven thermal history effects for process correction applications.

ACKNOWLEDGMENTS

I first want to thank Dr. Edward C. Kinzel for introducing me to the world of research and his guidance throughout my graduate career. His outreach while I was an undergraduate truly changed my professional direction by putting me on the path to graduate school. This achievement would not be possible without Dr. Kinzel's excellent leadership, professional example, and technical expertise. I thank Dr. James A. Drallmeier for his oversight and willingness to help me complete my graduate degree. I thank Dr. Robert G. Landers and Dr. Douglas A. Bristow for their input on my project. I particularly appreciate all the time Dr. Landers spent reviewing my work. I also thank Dr. Joseph W. Newkirk for sharing his knowledge whenever a question arose.

I am grateful to Honeywell Federal Manufacturing & Technologies for providing the equipment and supporting my work. I appreciate the project leads' time and feedback. I am thankful to Missouri University of Science and Technology for awarding me a Chancellor's Distinguished Fellowship.

Finally, I am thankful to my family for their love and support. I especially want to thank my wife, Avery, and my parents, Shannon and Sheri. Their encouragement is a foundational part of my life.

TABLE OF CONTENTS

Page

LIST OF ILLUSTRATIONS

PAPER I Page

PAPER II

LIST OF TABLES

1. INTRODUCTION

1.1. BACKGROUND

Laser Powder Bed Fusion (LPBF) is a powder bed based Additive Manufacturing (AM) process that fabricates 3D metal parts layer-by-layer [1]. In LPBF, an f–θ lens, or dynamic focusing optical system, focuses a galvanometer guided laser beam on the powder bed. The laser scans the powder bed with prescribed processing parameters (e.g. laser power, scan speed, hatch distance), and thus fuses the metal, along paths determined by the part's geometry. This procedure repeats after spreading a new powder layer with scan pathing updates based on the part's next geometry slice. The LPBF methodology provides the ability to manufacture complex geometry parts at length scales of hundreds of millimeters with feature resolutions limited by the melt size, which is typically sub-millimeter [2]. A wide range in structures (e.g. thick wall, thin wall, lattice) can compose a single LPBF part. The various structure types have unique optimal laser parameter sets and mechanical behavior [3]. A part's complicated geometry combined with its varying local part properties make non-destructive inspection difficult. Typically, high value LPBF part inspection occurs after manufacturing and consists of micro-CT (μCT) scanning to obtain x-ray image based volumetric data sets [4]. This method permits the identification of local porosity that can negatively impact the part's performance [5].

As LPBF manufacturing's prevalence and its mission critical part production increase, inspection procedures must provide further insight into the local part properties with minimal process impacts. The layer-to-layer and laser driven thermal nature of LPBF presents an opportunity to inspect parts during manufacturing (i.e. in-situ) by non-

intrusively measuring radiometric information [6]. Radiometric instruments (e.g. thermal cameras, pyrometers, photodiodes, and spectrometers) can produce a volumetric data sets based on the local thermal history for a part by combining measurements from each layer [7]. The radiometric information can be correlated to several part properties (e.g. porosity, microhardness, yield strength, etc.) [8]. Additionally, in-situ radiometric inspection can distinguish the thermal history variances caused by a part's geometry [9]. The technique should simultaneously inspect the various part structure types that have significant differences in thermal history and mechanical properties. These abilities require the instrumentation to spatially monitor the thermal history, and the features from their measurements must have high sensitivity to LPBF process variances.

Optical Emission Spectroscopy (OES) and thermography are both promising techniques that can spatially measure signals emitted during LPBF. Optical Emission Spectroscopy spectrally resolves light emitted from excited atoms. OES is established for both laser welding [10] and blown powder AM [11] where slow process dynamics and large laser powers produce high signal to noise ratios. OES measurements have been shown to provide information related to the blown powder AM part's quality including material composition [12] and porosity [13]. One study explored implementing OES principles during LPBF [14]. The fast dynamics and low powers in LPBF make OES implementation difficult, which limits the significant contribution it can provide. Further development of OES for LPBF will allow it to be used for in-situ part inspection. Thermography is the use of instrumentation to perform spatiotemporal temperature measurements. Thermography can be active where a heat is applied to identify defects in parts [15], or passive to measure emission from parts like during AM [16]. Short-Wave

Infrared (SWIR) thermal cameras measure wavelengths corresponding peak emission at most metal's melting temperatures. This allows measurement of features at temperatures critical to microstructure formation. Short-Wave cameras have been used to measure melt pool size [17] and cooling rates [18] in LPBF. Work remains to evaluate the correlation between SWIR measurements and LPBF part properties as well as determine the SWIR thermal feature's ability to predict part state locally.

An additional benefit of in-situ radiometric inspection is an experimental understanding of what contributes to thermal history variances. Wide ranging thermal models from analytical to high fidelity have made progress understanding this for LPBF from a theoretical standpoint [19–21]. Superposition models are process correction oriented and make part scale simulations feasible [22,23]. This idea combined with SWIR imaging measurements leads to the unique opportunity to perform superposition thermal modeling with experimental data. This modeling approach would allow quantitative prediction of how scan pathing affects the thermal history.

1.2. RESEARCH OBJECTIVES

This dissertation's main objective is to establish in-situ radiometric inspection methods for LPBF that address the knowledge gaps that exist for current systems in the literature. These knowledge gaps and the work to address them are given in each of the dissertation's four papers. The first paper's objective is to study the ability to correlate OES signals with local LPBF part information and determine what build conditions affect those signals. The second paper's objective is to define the capability of various SWIR imaging thermal features to correlate with LPBF part properties including yield strength

and porosity. The third paper's objective is to quantify the ability to locally predict porosity by SWIR imaging for nominal LPBF manufacturing scenarios. The fourth, and final, paper's objective is to quantify the scan path driven thermal history variance captured by a superposition thermal model based on SWIR data.

PAPER

I. IN-SITU OPTICAL EMISSION SPECTROSCOPY OF SELECTIVE LASER MELTING

Cody S. Lough[1], Luis I. Escano[2], Minglei Qu[2], Christopher C. Smith[1], Robert G. Landers[1], Douglas A. Bristow[1], Lianyi Chen[2], Edward C. Kinzel[3]

[1]Department of Mechanical and Aerospace Engineering, Missouri University of Science and Technology, Rolla, MO 65409

[2]Department of Mechanical Engineering, University of Wisconsin-Madison, Madison, WI 53706

[3]Department of Aerospace and Mechanical Engineering, University of Notre Dame, Notre Dame, IN 46556

ABSTRACT

The variances in local processing conditions during Selective Laser Melting (SLM), a powder bed Additive Manufacturing (AM) process, can cause defects that lead to part failure. The nature of SLM permits in-situ monitoring of radiometric signals emitted from the part surface during the process, including optical emission from excited alloying elements. Using Optical Emission Spectroscopy (OES) to measure the spectral content of light emitted gives insight into the chemistry and relative intensities of excited species vaporized during SLM processing. The contribution from investigating the use of in-situ OES to gain information about local processing conditions during SLM is reported in this paper. A spectrometer is split into the SLM system laser beam path to measure visible light emitted from the melt pool and plume during the processing of 304L

stainless steel. The in-line configuration allows signal collection regardless of the laser scan location. The spectroscopic information is correlated to the melt pool size and features of SLM samples for various build conditions (i.e., process parameters, build chamber atmosphere type and pressure).The limitations that exist in OES implementation for certain build chamber conditions are discussed. The results in this paper are initial progress towards the use of OES in SLM part qualification and controls applications.

1. INTRODUCTION

Selective Laser Melting (SLM) is a powder bed based Additive Manufacturing (AM) process in which three-dimensional parts are built layer-by-layer. One challenge in SLM is that the temperature history varies with the part geometry and process parameters. The local variance in thermal history is a source of defects as well as general inhomogeneity in properties such as the melt pool size, density, and yield strength. Qualifying AM parts is critical for high-value applications. The layer-to-layer nature of AM presents an opportunity to collect radiometric information for the volume of the part by combining measurements taken from the top surface of each layer. The radiometric information is a function of the local melt pool thermodynamic state and can be potentially correlated to local part properties. These measurements then provide the opportunity to validate parts in-situ, and if processed in real-time, can be used for feedback-based control. Optical Emission Spectroscopy (OES) spectrally resolves light emitted from excited atoms. The emission wavelength depends on atomic transitions

while the intensity depends on the atomic concentrations, excitation temperature, and to a lesser extent pressure.

Optical Emission Spectroscopy has previously been implemented in laser welding processes to provide information about the chemical species during the process and calculate the temperature and electron density in the vapor plume [1-3]. The spectroscopic data has been correlated with weld features, such as the melt pool depth to width ratio, and used to control the welding depth [4]. These OES methods have been extended and further developed to monitor the blown-powder metal Direct Energy Deposition (DED) process. The spectroscopic data was used to calculate plume temperatures, predict compositions, identify defects, and monitor clad quality [5-7].

Although OES has been established in blown-powder AM, there are fewer reports applying OES to powder-bed based AM. Dunbar et al. mounted a spectrometer at a fixed location in the build chamber of an SLM system and reported emission signal as a function of defocusing the process laser [8]. Dunbar and Nassar imaged the whole build plate onto a system of photodiodes with band-pass filters to measure the normalized strength of the chromium emission and correlated this signal with porosity of an Inconel 718 part created with SLM [9].

Implementing OES as a process monitoring tool in powder-bed based SLM can be more challenging when compared to blown-powder AM. In DED, the melt pool is stationary relative to the machine frame while in powder bed based SLM, the galvo-scanner steered laser beam creates a moving melt pool. However, the melt pool is stationary from the point-of-view of the process laser. When the spectrometer collects light from along the beam path, the integration volume follows the melt pool and allows

measurement of spectral information from any point on the build plate. It should be noted that most SLM systems use optics optimized for the process laser (typically Near Infrared) and this has the potential to introduce chromatic aberration near the periphery of the build plate, which is a function of dispersion as illustrated in Figure 1. These effects can be corrected with calibration, or via the use of achromatic optics. The platform allows basic OES and supports the inclusion of additional interrogation lasers for more advanced measurements (e.g., Laser Induced Incandescence, Scattering, or Breakdown Spectroscopy). Additionally, the framework has the potential to generate 3D point cloud data sets containing information derived from spectroscopic measurements. These data sets can be used to track layer-to-layer differences in local processing conditions including the melt pool size and elemental depletion, or segregation, which can affect the properties of the SLM parts.

In this paper, OES is performed during SLM with the spectrometer collection optics inserted into the beam path of the process laser. OES results for SLM of 304L stainless steel under various build conditions are reported, including the species in the vapor plume and relative emission intensities. The in-situ OES measurements, which correspond to the local processing conditions, are correlated with the melt pool properties of samples (melt pool size and morphology). This is significant because relating OES measurements to the melt pool features links information collected in-situ to a critical part feature that can contain defects due to under, or over melting [10] and establishes the density and surface roughness of SLM parts [11]. With further development, the in-situ spectroscopic measurements can be used in the qualification of parts during manufacturing and has potential for in-process control of SLM since they are effectively

monitoring the local melt pool attributes. Beyond the general framework and correlations, the paper also reports on the effects of the build chamber atmosphere and pressure on the melt-pool geometry and OES signal. These results have implications for understanding the SLM process and future implementations of in-situ OES.

2. EXPERIMENTAL APPROACH

Experiments were performed using a home-built SLM system and an Andor Technology SR-750 spectrometer. The SLM system used an IPG Photonics YLR-500 continuous wave fiber laser (λ = 1070 nm) with an IPG D30 collimator. The laser beam x-y position was controlled by a SCANLAB hurrySCAN and the laser was focused by a 340 mm focal length *f-θ* lens (measured $1/e^2$ beam diameter of 145 μm). Spectroscopic data was collected using a 600 *l*/mm diffraction grating installed in the spectrograph and an Andor Technology iStar 734 series ICCD (system spectral range 400-700 nm, spectral resolution ~0.1 nm). The spectrometer operated without intensity calibration, which is justified by comparing emission lines over a narrow wavelength range. The spectrometer was coupled to the SLM system by inserting the collection optics into the process laser beam path using a dichroic mirror (Thorlabs DMLP900) as illustrated in Figure 1 (a). The reflectance of the dichroic mirror is plotted in Figure 1 (b). This shows the optic did not significantly impact relative optical emission line intensity measurements since the reflectance is greater than 98.5% across the visible wavelengths. The collection optics consisted of an optical fiber (Andor SR-OPT-8014) coupled to the spectrometer by using an f/# matcher (Andor SR-ASM-0018). The optical fiber was attached to a collimator

(Thorlabs F220SMA) and the collimated light was then expanded before the dichroic mirror by using a Keplerian beam expander comprised of two plano-convex lenses (Thorlabs, f_1 = 50 mm and f_2 = 100 mm).

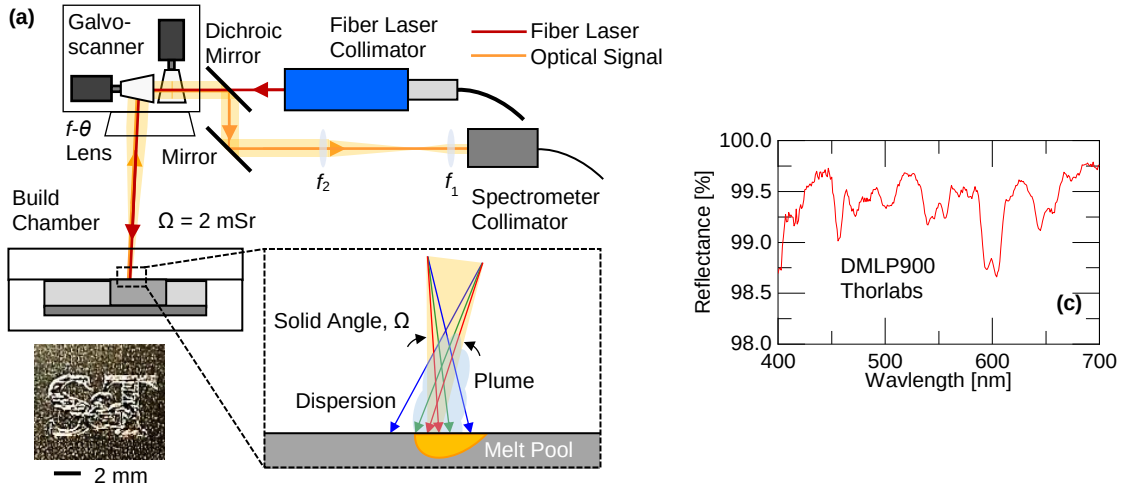

Figure 1. (a) Schematic of SLM system optical components with spectrometer inserted into SLM laser beam path, (b) interrogation of the plume above the melt pool illustrating the solid angle and dispersion (colors correspond to qualitative over focus relative to process laser wavelength for wavelengths from blue to red) and (c) reflectance of dichroic mirror [15].

There is a potential concern that one may obtain a limited solid angle, Ω, and dispersion (previously mentioned) when inserting the spectrometer optics into the beam path. The optical system solid angle determines the light collection efficiency during OES. For the OES method using the optical system illustrated in Figure 1, the solid angle was limited by the galvo-scanner aperture size (20 mm diameter) and the value was determined to be approximately 0.002 steradians. Despite limiting the intensity of the collected radiation, as well as the cross-section of the interrogation volume, experiments show that sufficient signal is received by the spectrometer to evaluate the melt pool. The

issue of dispersion is illustrated in Figure 1 (b) for SLM processing at the center of the build plate where shorter wavelengths (blue) are over focused while longer wavelengths (red) are closer to focused relative to the focus of the process laser. This affects the relative intensities of optical emission lines; however, this can be addressed. In SLM, the melt pool and interrogation volume position is determined by the scanner and is known, which allows a wavelength specific correction to be applied in-situ when required. Alternatively, dynamic focusing optics could be added to the spectrometer beam path as the optical system is developed further. In this work, the optics were aligned using 632.8 nm light at the center of the build plate and samples were not processed at the substrate edges to avoid the impacts of dispersion. Also, the effects of dispersion were negligible since measurements of relative emission intensities used in developing relationships with sample properties were made over a small wavelength range.

Experiments were conducted to generate OES data while performing SLM with various laser powers and build chamber conditions (atmosphere type and pressure). The process windows for the experiments are listed in Table 1, where the build chamber atmosphere type in the varied laser power and pressure studies was argon. The laser power values were selected to develop correlations between experimental OES and melt pool size measurements for processing conditions that can be successfully used to manufacture parts. The build chamber atmosphere types were selected to understand the influences of typical processing environments used in powder bed fusion on OES signals that need to be considered when developing this measurement system for process monitoring and control (near atmospheric pressure air is included to demonstrate the effects of oxygen in the system as extreme case). In particular, the pressure is varied from

0.2 to 800 Torr in an Ar atmosphere, which can significantly affect both the melt pool geometry and behavior of the vaporization/ionization processes determining both the recoil pressure and the OES signal.

Table 1. Experimental process windows.

Laser Power [W]	Build Chamber Atmosphere	Build Chamber Pressure [Torr]
200	Air: 730 Torr	0.2
250	Argon: 730 Torr	100
300	Nitrogen: 730 Torr	200
350	Argon: 0.2 Torr	300
400		400
		500
		600
		700
		800

In all the experiments, the laser was scanned in a raster pattern at a constant scan speed (675 mm/s) and hatch spacing (85 μm). The emission signals reported in the following section are processed time series spectral data averaged over laser melting 5×5 mm2 areas of a single, 50 μm thick 304L stainless steel powder layer. The powder size and chemistry of the 304L stainless steel lot used in this work were reported in [16]. The D50, or median particle size of the 304L stainless steel powder on a volume basis was ~28 μm and the chemical composition is listed in Table 2. The signals measured during processing the single layers contained an incandescent background with optical emission lines superimposed. Each frame of the time series OES data was processed by excluding the optical emission lines to fit the background with an eighth-order polynomial. This fit was subtracted from the original data, including optical emission signals, to remove any

effects of the incandescent background. The processed OES signals were then averaged over the 5×5 mm2 layer area to produce representative emission spectra corresponding to the respective SLM processing conditions.

Table 2. Chemical composition of 304L stainless steel powder in weight percent.

C	Cr	Cu	Fe	Mn	N	Ni	O	P	S	Si
0.018	18.4	<0.1	Balance	1.4	0.06	9.8	0.02	0.012	0.005	0.63

The melt pool sizes of the single layer samples produced by processing with the various conditions were measured through optical microscopy (Hirox KH-8700) after metallographic sample preparation (mounted, polished to 0.05 μm, and electrolytically etched with 60/40 nitric acid). The measured melt pool sizes for the samples processed with various laser powers were then correlated to corresponding emission line intensities. Experiments with various build chamber atmosphere types and pressures were conducted to explore the effects of these static environmental conditions on OES signals generated during SLM of 304L stainless steel.

3. RESULTS AND DISCUSSION

The relative intensities for optical emission lines are

$$I_{mn} \propto N_m \cdot A_{mn} \cdot h \cdot \nu_{mn} \quad (1)$$

where I_{mn} is the intensity, N_m is the upper state population, A_{mn} is the transition probability, h is the Planck constant, and v_{nm} is the frequency (m and n denote the upper

and lower energy levels, respectively) [5]. Figure 2 contains the average optical emission spectra for 304L collected during processing in an argon build chamber atmosphere with laser power varied from 200 to 400 W. The averages are from time series OES data sampled at 14 Hz during processing, which resulted in at least 9 frames of spectra for each laser power. The species of the emission lines measured during SLM of 304L stainless steel were identified by consultation of the NIST database [12]. The optical emission lines in Figure 2 correspond to neutral chromium, iron, and manganese, with chromium having the most apparent emission signal.

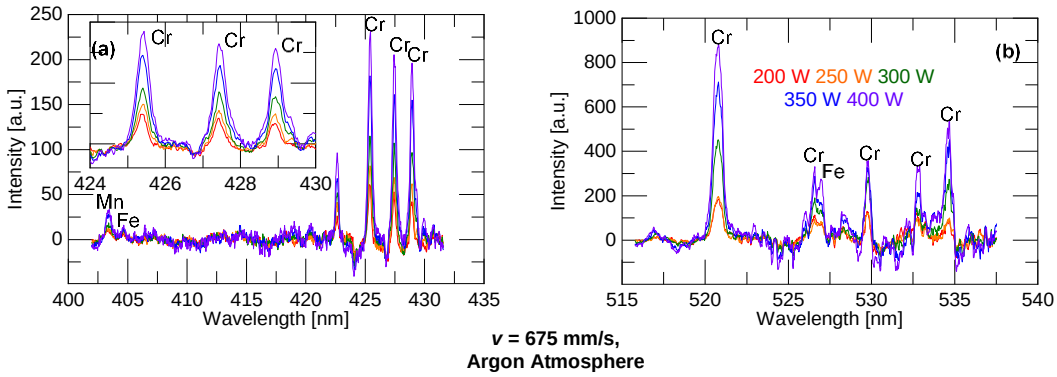

Figure 2. Average optical emission spectra of 304L stainless steel for wavelength ranges plotted from (a) 400 to 435 nm and (b) 515 to 540 nm measured during SLM with various laser powers.

The results in Figure 2 show the overall optical emission signal intensity increases for processing with higher laser powers. This increase in emission signal intensity was most likely due to the higher laser powers leading to more vaporization of the 304L stainless steel alloying elements from larger melt pools and higher temperatures. The strongest intensity corresponded to chromium emission around λ = 520.6 nm. The

average and standard deviation of intensity values of at λ = 520.6 nm were determined for correlation with the melt pool size. Figure 3 (a) is the plot of the intensity at λ = 520.6 nm for processing 304L in an argon atmosphere with the various laser powers. In Figure 3, the variance in the average intensity over the respective layers is most likely due to combined effects of the raster pattern scan path and the sampling frequency. The raster pattern scan path leads to increased dwell time where the laser goes around corners. The increased dwell time could result in more vaporization at the corners and higher temperatures, which would directly correspond to larger measured intensities. The measurement frequency results in under sampling of emission intensities for the middle of the raster pattern scan path where the melt pool reaches steady state. It is expected that increased sampling for this portion of the manufacturing process will reduce the magnitude of the emission intensity variance across the part. The longer dwells at the part edges, combined with the low sampling frequency, amplify the increase in variance for the measured intensity, especially for higher laser powers.

Figure 3 (b) is the correlation of the average chromium emission intensity around λ = 520.6 nm with the average melt pool size (i.e., the depth, *D*, and half width, *W*, defined in the optical micrograph) across single layer samples processed with the various laser powers. Figure 3 (b) shows larger melt pools correspond to higher chromium emission intensities; however, the standard deviations in both measurements (error bars) result in some overlap. The results in Figure 3 (b) strongly suggest a dependence of the melt pool depth on the recoil pressure caused by material vaporization during processing. It is expected that a larger recoil pressure (increased vaporization) would correspond to a melt pool depth increase. This result was qualitatively tracked by the OES measurements

where the higher emission intensities from increased vaporization correspond to deeper melt pools. The fits of the melt pool properties as a function of the chromium emission intensity show that the half width is slightly more sensitive than the depth for the samples processed by the home-built SLM system. Overall, these results demonstrate a strong relationship between local processing conditions obtained through OES and SLM sample properties.

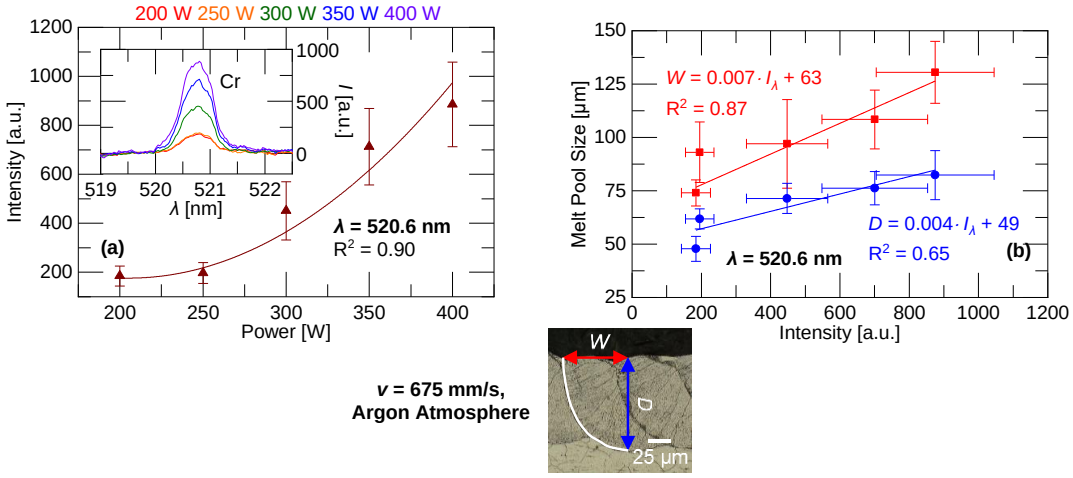

Figure 3. (a) Average intensity of chromium emission around λ = 520.6 nm and (b) average melt pool size of single layers plotted versus average intensity of chromium emission for corresponding layers.

In addition to their dependence on laser power, OES signals also depend on the build chamber atmosphere type and pressure. Experiments show that these parameters have significant effects on OES implementation in the SLM process. Figure 4 (a) contains the average OES signals for processing single layers of 304L stainless steel with various build chamber atmosphere types including air, argon, and nitrogen, all at a pressure of 730 Torr, and a low pressure argon atmosphere (0.2 Torr). The single layer

samples were processed in the various atmospheres using a laser power of 300 W. Figure 4 (a) shows the average optical emission line intensities measured during processing in an air atmosphere are much stronger than the signals collected in the argon, nitrogen, and low pressure argon atmospheres. The higher signal intensity when processing in air could be due to increased material vaporization leading to larger element populations in the plume. The increased vaporization would be reflected in a more keyhole mode like appearance of the melt pool, or an increased melt pool depth due to larger keyhole formation during laser melting. Micrographs of the melt pool cross-sections (Figure 4 (b-e)) show conduction mode melting dominates regardless of chamber atmosphere. However, the average melt pool depth when processing in air is larger, supporting the idea of increased vaporization leading to the stronger OES signal. The increased OES signal strength for air could also be explained by the oxidation of the vaporized chromium and iron. The exothermic oxidation process adds heat to the vapor plume above the melt pool, increasing both the excitation temperature and the resulting signal intensity measured through OES [13]. The OES signals are not amplified from the oxidation process during SLM in the inert argon, nitrogen, and low pressure argon environments. The similar emission intensities for the argon and nitrogen atmospheres reported in Figure 4 (a) correspond to similar average melt pool sizes in the respective single layer samples.

In Figure 4 (a), there were no apparent emission lines measured for processing with the build chamber atmosphere at a pressure of 0.2 Torr. This result occurred during processing in chamber pressures lower than 300 Torr. Figure 5 (a) shows the dependence of optical emission signal measured during SLM processing on the build chamber

pressure. The build chamber atmosphere type for OES data collection during this experiment was argon. In Figure 5 (a), the emission line intensities increase with increasing chamber pressure (0.2 to 800 Torr). The weaker, or lack of optical emission signals, for processing with the chamber pressures of 0.2 to 300 Torr were a result of less interaction of the laser with the plume. This was caused by the lack of vapor plume confinement for the lower pressure atmospheres, leading to the quick expansion of the vaporized alloying elements away from the laser exposure location. The increase in optical emission signals for the pressures ranging from 400 to 800 Torr were due to an increased plume confinement at the higher pressures, resulting in longer laser interaction times for the vaporized alloying elements. [14]

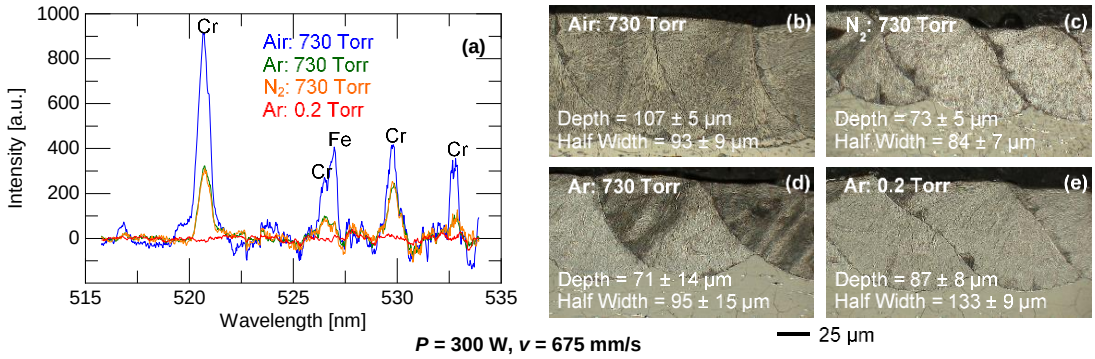

Figure 4. (a) OES signal collected during SLM processing with different build chamber atmospheres and (b-e) representative micrographs of 304L stainless steel single layer cross-sections processed in various atmospheres.

Figure 5 (b) is the intensity of the neutral chromium emission around λ = 520.6 nm as a function of chamber pressure. An increase in intensity variation is observed for pressures greater than 500 Torr. Photographs of parts for selected pressures (100, 400,

and 700 Torr) are included in Figure 5 (b). Lower chamber pressures resulted in qualitatively better surface finishes for the layers and this result demonstrates that higher surface finish quality correspond to weaker optical emission signal intensities. The chamber pressure also affected the size and morphology of the melt pools in the single layer samples as shown in Figure 5 (c-e). Low pressures resulted in deeper and less wide melt pools, while higher pressures led to shallower and wider melt pools with more variance in the half width dimension. The increase in optical emission signal variation and change in melt pool morphology at higher chamber pressures are also due to increased plume confinement. The confinement at higher pressures leads to increased variation in optical emission signals due to more plume-laser interaction. As a result, the laser is attenuated and defocused leading to the shallower and wider melt pools observed.

The results in Figures 4 and 5 show that the build chamber atmosphere type and pressure significantly impact the measured OES signals and melt pool properties of the SLM samples. Understanding the reported effects of the processing environment on the measurements is critical for the development of OES as a process monitoring tool for qualification and controls applications. Also, a limitation for this method exists in the case of low chamber pressures. OES did not provide meaningful information about emission signal for chamber pressures less than 400 Torr. The effects of laser processing parameters and build chamber environment on emission signal intensity and sample properties will be explored further in future work.

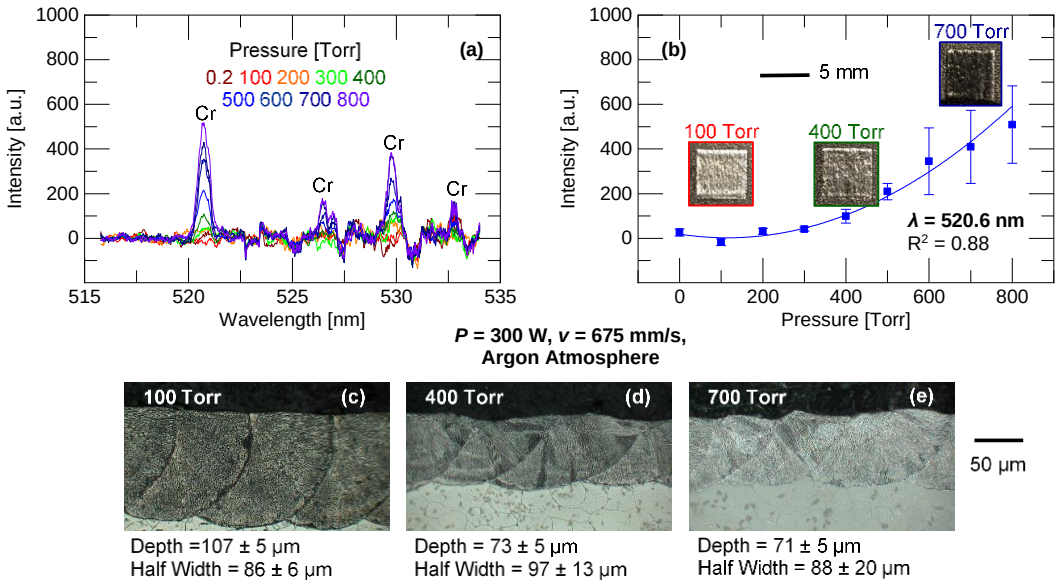

Figure 5. (a) OES signal collected during SLM processing with different build chamber pressures, (b) intensity of chromium emission around λ = 520.6 nm, and (c-e) representative micrographs of 304L stainless steel single layer cross-sections processed with various pressures.

4. SUMMARY AND CONCLUSIONS

This paper reported in-situ OES measurements of local processing conditions through the interrogation of the SLM melt pool and plume during movement in a stationary global reference frame. The measurement system was used to explore the effects of SLM processing conditions including laser power and build chamber atmosphere type and pressure on OES signals. The intensity of chromium emission was found to correlate well with the melt pool size. This result demonstrated a relationship between radiometric measurements from OES and a meaningful sample property, which points to the ability to implement the method in SLM part qualification and controls. The OES results in this paper also show optical emission signals heavily depend on build

chamber atmosphere type and pressure, with higher chamber pressures resulting in stronger measured intensities and low pressures leading to a limitation in measurement capability. The pressure results corresponded to a change in the surface finishes of the layers and melt pool sizes and morphologies. These effects are critical to understand in the development of OES as an SLM process monitoring tool.

In general, the use of OES as a process monitoring tool provides meaningful information about the local process conditions in SLM and is helpful for system development. The spectrometer is readily adaptable to take measurements during SLM of different materials with different processing conditions for decision making. Future work will involve expanding the experimental process windows to explore the influence of scan speed on the measured optical emission signals and manufacturing multi-layer parts to demonstrate the correlation of properties including density and yield strength to information from OES signals. Further improvements of the process and the correlations of OES signals to sample properties will allow the possibility of this measurement method to be used in SLM part qualification and feedback control applications.

ACKNOWLEDGMENT

This work was funded by Honeywell Federal Manufacturing & Technologies under Contract No. DE-NA0002839 with the U.S. Department of Energy. The United States Government retains and the publisher, by accepting the article for publication, acknowledges that the United States Government retains a nonexclusive, paid up,

REFERENCES

[1] Collur MM, Debroy T. Emission spectroscopy of plasma during laser welding of AISI 201 stainless steel. Metall Mater Trans B 1989;20:277–86. https://doi.org/10.1007/BF02825608.

[2] Szymański Z, Kurzyna J, Kalita W. The spectroscopy of the plasma plume induced during laser welding of stainless steel and titanium. J Phys D Appl Phys 1997;30:3153–62. https://doi.org/10.1088/0022-3727/30/22/014.

[3] Kawahito Y, Matsumoto N, Mizutani M, Katayama S. Characterisation of plasma induced during high power fibre laser welding of stainless steel. Sci Technol Weld Join 2008;13:744–8. https://doi.org/10.1179/136217108X329313.

[4] Sibillano T, Rizzi D, Mezzapesa FP, Lugarà PM, Konuk AR, Aarts R, et al. Closed loop control of penetration depth during CO2 laser lap welding processes. Sensors 2012;12:11077–90. https://doi.org/10.3390/s120811077.

[5] Song L, Mazumder J. Spectroscopy during direct metal deposition process. IEEE Sens J 2012;12:958–64.

[6] Nassar AR, Spurgeon TJ, Reutzel, EW. Sensing defects during directed-energy additive manufacturing of metal parts using optical emissions spectroscopy. Solid Free Fabr 2014 Proc 25th Annu Int 2014:278–87.

[7] Ya W, Konuk AR, Aarts R, Pathiraj B, Huis In 'T Veld B. Spectroscopic monitoring of metallic bonding in laser metal deposition. J Mater Process Technol 2015;220:276–84. https://doi.org/10.1016/j.jmatprotec.2015.01.026.

[8] Dunbar AJ, Nassar AR, Reutzel EW, Blecher JJ. A real-time communication architecture for metal powder bed fusion additive manufacturing. Solid Free Fabr 2016 Proc 27th Annu Int 2016:67–80.

[9] Dunbar AJ, Nassar AR. Assessment of optical emission analysis for in-process monitoring of powder bed fusion additive manufacturing. Virtual Phys Prototyp 2018;13:14–9. https://doi.org/10.1080/17452759.2017.1392683.

[10] Scime L, Beuth J. Melt pool geometry and morphology variability for the Inconel 718 alloy in a laser powder bed fusion additive manufacturing process. Addit Manuf 2019;29:100830. https://doi.org/10.1016/j.addma.2019.100830.

[11] Criales LE, Arısoy YM, Lane B, Moylan S, Donmez A, Özel T. Laser powder bed fusion of nickel alloy 625: Experimental investigations of effects of process parameters on melt pool size and shape with spatter analysis. Int J Mach Tools Manuf 2017;121:22–36. https://doi.org/10.1016/j.ijmachtools.2017.03.004.

[12] Kramida A, Ralchenko Y, Reader, J. NIST atomic spectra database (ver. 5.6.1). National Institute of Standards and Technology, Gaithersburg, MD 2018.

[13] Shin J, Mazumder J. Composition monitoring using plasma diagnostics during direct metal deposition (DMD) process. Opt Laser Technol 2018;106:40–6. https://doi.org/10.1016/j.optlastec.2018.03.020.

[14] Farid N, Wang H, Li C, Wu X, Oderji HY, Ding H, et al. Effect of background gases at reduced pressures on the laser treated surface morphology, spectral emission and characteristics parameters of laser produced Mo plasmas. J Nucl Mater 2013;438:183–9. https://doi.org/10.1016/j.jnucmat.2013.03.022.

[15] Thorlabs. Unpolarized performance of 900 nm longpass dichroic mirror.

[16] Sutton AT, Kriewall CS, Leu MC, Newkirk JW, Brown B. Characterization of laser spatter and condensate generated during the selective laser melting of 304L stainless steel powder. Addit Manuf 2020;31:100904. https://doi.org/10.1016/j.addma.2019.100904.

II. CORRELATION OF SWIR IMAGING WITH LPBF 304L STAINLESS STEEL PART PROPERTIES

Cody S. Lough[1], Xin Wang[1], Christopher C. Smith[1], Robert G. Landers[1], Douglas A. Bristow[1], James A. Drallmeier[1], Ben Brown[2], Edward C. Kinzel[3]

[1]Department of Mechanical and Aerospace Engineering, Missouri University of Science and Technology, Rolla, MO 65409

[2]Kansas City National Security Campus, Kansas City, MO 64147

[3]Department of Aerospace and Mechanical Engineering, University of Notre Dame, Notre Dame, IN 46556

ABSTRACT

In the Laser Powder Bed Fusion (LPBF) process, the local thermal history can vary significantly over a part as the heat transfer characteristics and the laser scan path are geometry dependent. The variations introduce the potential for defects that lead to part failure, some of which are difficult to identify non-destructively with common ex-situ evaluation techniques. These defects include significant microstructural and mechanical property differences in the part interiors. In this paper, thermal features are extracted from in-situ Short-Wave Infrared (SWIR) imaging measurements to compile voxel based part representations and understand how the complexities in the thermal history affect part performance. The deviations in thermal features due to different laser processing parameters and complex scan pathing are explored. Empirical correlations are developed to map thermal features with the engineering properties (bulk yield strength, area percentage porosity, and local state) of 304L stainless steel parts manufactured by

LPBF. Processing modes (insufficient melting and keyholing) are determined by mapping part property measurements with multiple thermal features. Generating the relationships between thermographic measurements and resulting SLM part properties lays the foundation for in-situ part qualification.

1. INTRODUCTION

Laser Powder Bed Fusion (LPBF) is a powder bed based Additive Manufacturing (AM) process in which 3D metal parts are produced layer-by-layer. Within a layer, a laser scans and fuses the metal powder bed in areas determined by the geometry of the part slice corresponding to that layer. The ability to manufacture complicated geometries with LPBF results in the generation of complex laser scan patterns and cooling paths dependent on the previously processed material. For a fixed process parameter set, the differences in part cross-sectional area within a layer and the changes in geometry as the part is manufactured lead to inhomogeneity in the thermal history and, thus, significant variations in the part microstructure and mechanical properties [1]. The variations in the thermal history experienced by parts during fabrication potentially introduce significant defects. Finding the differences in the local part properties and locating defects can be challenging using ex-situ characterization. Spatially monitoring the thermal history and its variations during processing with in-situ non-intrusive thermography can provide an understanding of LPBF processes and establishes a framework for addressing this problem.

Previous studies have used various non-intrusive instruments, including visible/high-speed cameras [2-12], infrared cameras [13-30], pyrometers [31,32], and photodiodes [41-43], to perform measurements of the part's thermal profile and features during AM processes. These thermal features are related to the local processing conditions experienced by AM parts while they are being manufactured. Studies have been performed to utilize the features from the measured thermal imaging and photodiode data to develop reconstructions of part geometries [33-40]. These efforts were a part of understanding how the thermal history varies throughout the part in working towards validation of AM processes. Few researchers have worked to relate in-situ thermographic measurements to AM part properties. Some correlations between data measured using photodiodes and the resulting part mechanical properties and density/porosity have been developed. Bisht et al. related melt pool intensity data measured with an off-axis photodiode during the Direct Metal Printing (DMP) to the ultimate strength and plastic elongation of Ti-6Al-4V ELI specimens [41]. Coeck et al. correlated 3D maps generated by in-situ photodiode measurements of melt pool events taken during DMP with the Ti-6Al-4V ELI part density obtained by Computed Tomography (CT) scanning [42]. Alberts et al. used a system of in-line photodiodes to monitor the melt pool during LPBF of Inconel 718 where time series data were combined with laser position to generate 2D maps, and measurements from various processing conditions were correlated with part density by plotting both parameters as a function of the energy input [43]. Data sets from visible and some types of infrared cameras have also been related to melt pool information, or part properties. Demir et al. used an in-line process monitoring system consisting of visible and Near Infrared (NIR) detectors to measure light emitted during

LPBF of 8Ni300 maraging steel, which was reported as a function of energy input, and correlated the signals with part porosity [44]. Foster et al. demonstrated that melt pool characteristics determined from in-situ monitoring during LPBF (Renishaw AM250) of Inconel 718 with a Mid-Wave Infrared (MWIR) camera could be used with information from comprehensive ex-situ characterization to possibly detect process failures [45]. Yoder et al. captured Near Infrared (NIR) images after each layer during Electron Beam Melting (EBM) of Ti-6Al-4V to detect porosity and show variations in part properties for various build conditions [46]. Lu et al. detected and correlated features in optical images taken after recoating with part density, yield, and ultimate strength for LPBF of 316L stainless steel with various laser parameters [47].

The studies performed to correlate features from thermographic signals with part properties, including mechanical strength and density/porosity, have used mapped photodiode data, averaged inline camera data, or processed single frame images. While these thermographic measurements have been shown to correlate well with part properties, they are effectively single point, or single frame, measurements and, thus, are limited since they do not contain information from the entire thermal history. Recording spatiotemporal thermal data during LPBF has the potential to provide more insight into the process. This is possible because events that impact the final part microstructure (i.e., re-melting, cooling rates, thermal gradients) are measurable. Thermal cameras should work well in developing the correlations since they permit the mapping of complex features (e.g., spatial and temporal derivatives, integration features) that are more closely related to the final part microstructure than the data from single point intensity measurements, or images taken after a layer is completed.

Infrared cameras with various wavelength sensitivities including NIR (0.7-1.1 μm) [13-19,44,46], SWIR (0.9-1.7 μm) [20-23], MWIR (3-5 μm) [24,25,45], and Long-Wave Infrared (LWIR, 8-14 μm) [26-30] have been used to monitor AM. Cameras operating in the NIR, SWIR, and MWIR capture fast dynamic events at high temperatures. Typical LWIR cameras (microbolometer based) can capture events that occur at lower temperatures, but have much slower framerates making them appropriate for monitoring thermal stress, but not melt pool dynamics. SWIR cameras have advantages over the alternative thermal cameras. For example, at the melting point of 304L stainless steel (~1720 K), the sensitivity of the radiance with respect to the blackbody temperature in the SWIR wavelength band is ~4 times higher than NIR, ~3 times higher than MWIR, and ~32 times higher than LWIR. This is because the Planck distribution peaks at the melting temperature in the SWIR band. Additionally, as in the visible and NIR range, conventional silica based optics and windows can be used throughout the SWIR range, whereas glass is absorbing in the MWIR and LWIR. A SWIR camera was selected for this work since they capture the fast melt pool dynamics during LPBF through measurement of wavelengths that correspond to peak emission at the temperatures (i.e., liquidus, solidus, and below solidus) that are critical during microstructure formation in LPBF of stainless steel.

This paper develops correlations between information extracted from in-situ SWIR imaging measurements and part properties for LPBF of 304L stainless steel. The SWIR measurements are processed by a voxel based framework to generate 3D reconstructions of part geometries that are composed of extracted thermal features. In this work, a voxel is a 3D pixel with values that directly correspond to the local thermal

history a part experienced during manufacturing. The thermal features extracted included the apparent melt pool area, the time above threshold, the maximum radiance, the maximum radiance decrease rate, and the radiance sum above threshold. Local voxel value averages of the various thermal features are correlated with the energy input during LPBF and resulting part properties including the yield strength and the bulk area percentage porosity. Multiple thermal features are combined to distinguish LPBF processing modes. The thermal features in a full 3D reconstruction of a sample manufactured with an embedded feature is correlated with the local state of the part indicated by ex-situ micro-computed tomography (μCT) scanning. The correlations developed in this paper indicate the potential for the prediction of local LPBF part properties in efforts towards qualification based on in-situ SWIR imaging measurements.

2. EXPERIMENTAL SETUP

A Renishaw AM250 was used to manufacture 304L stainless steel cylindrical tensile test specimens (ASTM E8) and various samples for layer-to-layer SWIR imaging. The Renishaw AM250 processes parts by scanning an SPI Lasers fiber laser (maximum power is 200 W and wavelength is 1,070 nm) with a point-to-point exposure strategy. In this strategy, the laser steps discretely by the point distance, d_p, and then turns on for the exposure time, t_e. This is performed in a raster pattern with the distance between laser scans defined as the hatch spacing, d_h. At the conclusion of the laser raster, two border scans are performed. The process repeats with a rotation of the laser raster pattern from layer-to-layer. The 304L stainless steel tensile specimens were manufactured using this

laser scan strategy with various laser process parameter sets to generate a range in thermal histories and mechanical properties. The parameter sets are listed in Table 1 and included combinations of the laser power from 100 W to 200 W (increments of 25 W) and the exposure time varied from 50 µs to 125 µs (increments of 25 µs). The point distance (d_p = 60 µm) and the hatch spacing (d_h = 85 µm) were held constant.

Table 1. Process parameter set combinations used to manufacture tensile specimens and partitions in recording sample.

Parameter Set	***P* [W]**	**t_e [µs]**	***F* [J/mm^2]**
1	100	50	1.3
2		75	2.0
3		100	2.6
4		125	3.3
5	125	50	1.6
6		75	2.4
7		100	3.3
8		125	4.1
9	150	50	2.0
10		75	2.9
11		100	3.9
12		125	4.9
13	175	50	2.3
14		75	3.4
15		100	4.6
16		125	5.7
17	200	50	2.6
18		75	3.9
19		100	5.2
20		125	6.5

The process parameter combinations can be simplified to the optical energy per unit area by computing the fluence

$$F = \frac{P \cdot t_e}{A_b} \tag{1}$$

where P is the laser power, t_e is the exposure time, and A_b is the laser beam area. The fluence values for the various process parameter sets are listed in Table 1 and ranged from 1.3 J/mm^2 to 6.5 J/mm^2. In addition, a recording sample was manufactured with tensile specimens to efficiently measure the differences in thermal history generated by the various process parameter sets through SWIR imaging. The designs for the tensile specimens and the various parameters recording sample can be seen in Figure 1 (a) and Figure 1 (c), respectively.

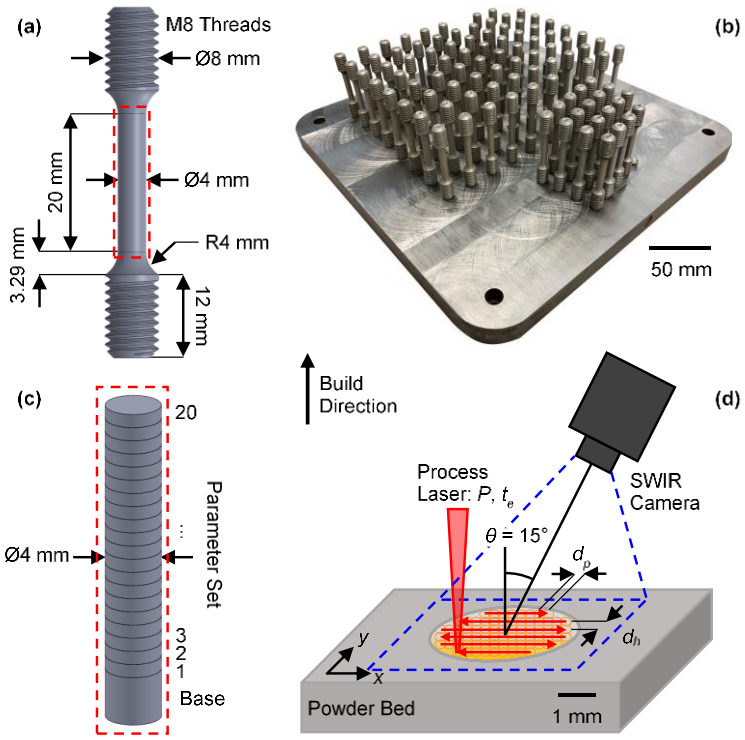

Figure 1. (a) ASTM E8 tensile specimen design, (b) build image showing specimen layout, (c) various process parameters recording sample for SWIR imaging data collection, and (d) schematic of SWIR camera observation during manufacturing recording sample with annotations for the AM250 process parameters.

As illustrated in Figure 1 (a) and (c), the cross-sectional geometry of the recording sample corresponded to the gauge length of the ASTM E8 tensile specimens. The recording sample was partitioned perpendicular to the build direction and consisted of a 100 layer base and 20 sections, each containing 18 layers and having unique process parameter sets. The design and plan for manufacturing the various parameters recording sample assumed the thermal history did not vary significantly with build height for a near constant layer-to-layer time and the thermal history of parts with the same cross-sectional geometry and process parameter set was similar. A schematic of the SWIR Camera observation during LPBF of a layer in the recording sample is included in Figure 1 (d). The SWIR camera used in this work was a FLIR SC6201 camera (sensitive: 0.9-1.7 μm, filtered: 1.45 ± 0.05 μm). The camera was installed in a staring configuration above the build chamber to observe the build plate through a custom window. The 640×512 camera pixel array was reduced to an 80×80 pixel window enabling high frame rate recording (~2500 Hz). The *x*-direction instantaneous field of view of the SWIR camera was ~130 μm/pixel. The *y*-direction instantaneous field of view was ~135 μm/pixel due to the observation angle ($\theta = 15°$) of the SWIR camera shown in Figure 1 (d). A non-uniformity correction (NUC) was performed to account for differences in the SWIR measurements across the imaging area due to the observation angle, vignetting from the viewing window, and variance in pixel sensitivities. The SWIR camera was not calibrated for temperature and raw data is reported as radiance values of arbitrary units (a.u.); however, an estimate of the measurable temperature range was determined. The floor temperature was approximately 800 K. This was found by heating a LPBF manufactured blackbody with the process laser and comparing thermocouple data with SWIR imaging radiance

measurements. The upper limit of the measureable temperature range was greater than the liquidus temperature of 304L stainless steel (~1720 K). This was determined through observation of the radiance corresponding to apparent phase transition during solidification and the lack of saturation in the raw radiance data for normal LPBF processing conditions. The goal of this work was to develop relationships between thermal features extracted from the radiance measurements and bulk part properties of the 304L stainless steel samples corresponding to the various process parameters by using a voxel based approach.

The part properties determined for the LPBF of 304L stainless steel were the yield strength, σ_y, and area percentage porosity, φ. The tensile specimens' yield strengths were tested on an Instron 5969 following ASTM E8 standards [48]. Averages and standard deviations for the yield strength of the specimens were calculated using the results from 5 samples. The locations of each parameter sets' 5 tensile specimens was randomized and the LPBF build layout is shown in Figure 1 (b). The tensile specimens' porosities were measured through image analysis of 25 representative optical micrographs taken after metallographic sample preparation (sample sectioned, mounted in Bakelite, ground, and polished to 0.05 μm using diamond suspension). The image processing procedure used to determine area percentage porosity followed ASTM E2109 [49], and was similar to the methods found in [50].

3. SWIR CAMERA DATA PROCESSING

3.1. INTRODUCTION TO THERMAL FEATURE EXTRACTION

Figure 2 (a-c) is an example of raw time series radiance data that was measured from the middle of the raster scan path in the recording sample for three of the process parameter sets. The parameter sets were the minimum (Figure 2 (a)), nominal (Figure 2 (b)), and maximum fluence inputs (Figure 2 (c)). The inset images of the apparent melt pool included in Figure 2 (a-c) correspond to the frame when the center pixel was at maximum radiance. The raw data in Figure 2 provides insight into the LPBF process for each of the process parameter sets with qualitative comparisons of the melt pool images showing larger areas and radiances for the higher fluence inputs. Additionally, an increase in maximum radiance with increasing fluence input is visible in the plots of the time-series data. While qualitative differences are observed in the time series radiance data, meaningful quantitative relationships can be developed with this information and the LPBF part properties through thermal feature extraction. This method is a computationally inexpensive approach of processing the time series SWIR imaging measurements that permits the efficient observation of differences in the thermal history of parts for correlation development with both the fluence input and engineering properties.

The extraction of thermal features results in the reduction of a multi-frame recording to a single image representation for each layer. The concatenation of the 2D thermal feature data for each layer builds a 3D voxel based reconstruction of the sample. The voxel thermal feature values in the sample reconstruction retains information directly

related to the local thermal history for development of correlations with a significantly smaller amount of data. For example, this approach resulted in the compression of ~100 GB of time series data for the entire volume of a cylindrical ASTM E8 tensile specimen into ~3 MB of voxel based data reconstruction.

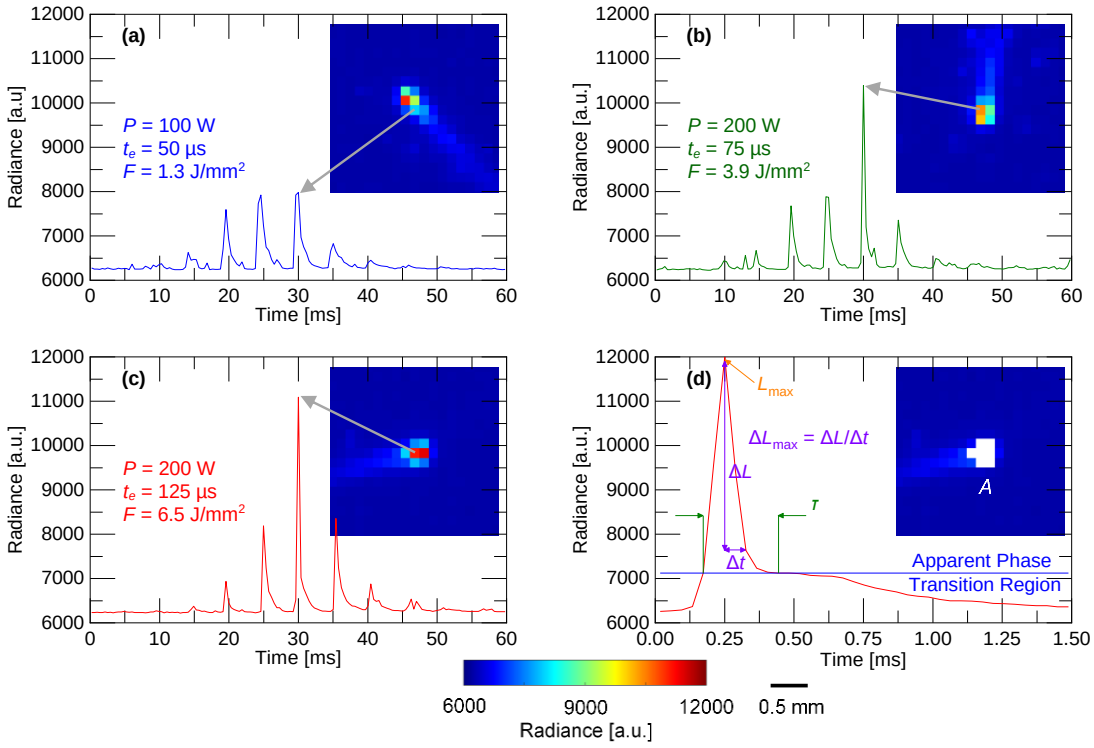

Figure 2. (a-c) Time series radiance data for various process parameter sets, and (d) time series data showing apparent phase transition region with illustrations of selected thermal features.

The thermal features extracted for this work included the apparent melt pool area, A, the time above threshold, τ, the maximum radiance, L_{max}, the maximum radiance decrease rate, ΔL_{max}, and the radiance sum above threshold, ΣL. These thermal features

were selected to compare common measurements used in the literature that are obtainable by various instrumentation. Thermal cameras are used to take single frame images, or information is extracted from the spatiotemporal data (melt pool size/area, maximum radiance, features analogous to maximum radiance decrease rate). Some researchers extract features that correspond to the time above threshold, or radiance sum above threshold. Photodiodes are used to spatially map a feature corresponding to the maximum radiance. The results in this work will show that the features are strongly related; however, the time above threshold has advantages making it the feature of major interest. The advantages include a high signal to noise ratio, smoothness of the data, and high correlation strength with fluence and mechanical properties.

The thermal features were extracted from both the spatial and temporal domains of the SWIR imaging data. The spatial feature of the apparent melt pool area is

$$A(t) = \left| \left\{ (x, y) : L(x, y, t) \geq threshold \right\} \right| \tag{2}$$

where $L(x, y, t)$ denotes the radiance measurement of the pixel (x, y) at time t and $|\blacksquare|$ denotes the measure of the set. The apparent melt pool area is illustrated in Figure 2 (d) where pixels above a threshold have been flagged (white pixels) for determining the value for the feature. The value for the melt pool area is assigned to the voxel that corresponds to the centroid of the melt pool; therefore, some voxels may not be assigned a value.

The thermal features extracted from the time domain included the time above threshold, the maximum radiance, the maximum radiance decrease rate, and the radiance sum above threshold. Saturation in the time series SWIR imaging measurements due to excessive radiance must be considered for thermal features based on the maximum

values, or total radiance. The time above threshold is a feature proportional to the local melt pool size where larger melt pool sizes lead to more re-melting, which results in an increased time above threshold for a voxel. Since the time above threshold is a time domain thermal feature, each voxel has a value. The time above threshold is

$$\tau(x,y) = \left| \left\{ t : L(x,y,t) \geq threshold \right\} \right|. \tag{3}$$

The time above threshold is illustrated in Figure 2 (d). This feature is determined by interpolating the time from the point the radiance crosses the threshold during heating to the point the radiance drops below the threshold value during cooling. The time above threshold thermal feature for a single pixel is the sum of all the interpolated times corresponding to the melting and (possible) re-melting events that occur during LPBF processing.

The temporal thermal features, including the maximum radiance and maximum radiance decrease rate, are the least computationally expensive to determine; however, they cannot be computed if the SWIR imaging data saturates. The maximum radiance is

$$L_{\max}(x,y) = \left| \left\{ t : \max\left[L(x,y,t) \right] \right\} \right| \tag{4}$$

and the maximum radiance decrease rate is

$$\Delta L_{\max}(x,y) = \left| \left\{ t : -\min\left[\frac{L(x,y,t+1) - L(x,y,t)}{\Delta t} \right] \right\} \right|. \tag{5}$$

The thermal feature of the radiance sum above threshold is

$$\sum L(x,y) = \left| \left\{ t : \mathrm{sum}\left[L(x,y,t) \geq threshold \right] \right\} \right|. \tag{6}$$

While saturation would inhibit the determination of the maximum radiance, the maximum radiance decrease rate, and the radiance sum above threshold, the time above

threshold should remain unaffected. In this work, the remaining temporal thermal features were determined through preventing saturation of the data in experiments by sufficiently increasing the *f*/# of the SWIR imaging camera.

Threshold selection is a critical part of thermal feature extraction. In this work, a radiance threshold corresponding to the physical property of solidification was selected. Additionally, the signal to noise ratio a threshold provides should be considered. While not included, a study was ran to determine the threshold that led the highest signal to noise ratio. The threshold based on solidification was found to provide the highest signal to noise ratio. The threshold value used in this work was 7120 a.u. and corresponds to the measured radiance of the apparent phase transition region during solidification. The apparent phase transition region during solidification is observed in the time series SWIR imaging data plotted in Figure 2 (d) and is well below the saturation limit. The threshold value was determined through multiple observations in the time series radiance data from various pixels over several layers.

3.2. RESULTS OF THERMAL FEATURE EXTRACTION

The time above threshold will be the primary thermal feature used to demonstrate the capabilities of the layer-to-layer SWIR imaging framework. Figure 3 contains the time above threshold voxel based reconstruction of the various parameters recording sample illustrated in Figure 1 (c). The voxel based data can be sliced for inspection and further processing. The slicing is demonstrated in the two cross-section views of the recording sample's voxel based reconstruction. The first slice of the voxel based data in the *x*-*z* plane shows qualitatively clear differences in the time above threshold for the

various process parameter combinations. The slice of the voxel data in the *x-y* plane shows uniform time above threshold values in the center of the part with higher values at the edges of the part due to the increased dwell times where the laser corners and border scans are performed. Spatial filtering was applied to avoid the observable effects of the border scan areas on thermal feature distributions. The spatial filtering is demonstrated in Figure 3 (b) using the time above threshold map for the nominal process parameter set. Data in a map was only kept for analysis if it corresponded to the interior of the part cross-section away from the border scan area. While not included here, the remaining thermal features were also extracted for the various process parameters recording sample to generate reconstruction maps. The distributions of the various thermal features for a layer processed with the nominal parameter set are discussed below along with analysis of the layer-to-layer variation for the time above threshold.

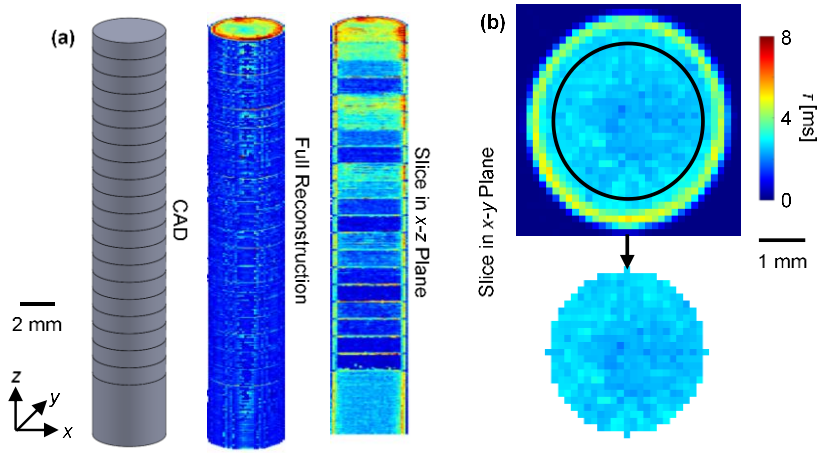

Figure 3. (a) Voxel based time above threshold reconstruction of various process parameters recording sample with slicing of experimental data and (b) demonstration of spatial filtering in *x-y* plane slice to exclude effects of border scan area data.

The distributions of the various thermal features for a nominal layer are plotted in Figure 4. The thermal feature maps are included as insets in Figure 4 with the mean feature values, μ, and standard deviations, σ, for the layer listed. The variations in the thermal features were compared by quantifying the percentage of pixel values within one standard deviation of the mean. The time above threshold demonstrated the best distribution with 71% of the pixel values within one standard deviation of the mean while the apparent melt pool area resulted in only 42%. The maximum radiance, maximum radiance decrease rate, and radiance sum above threshold resulted in 62%, 64%, and 67% of pixels within one standard deviation of the mean, respectively. The melt pool area performed poorly when compared to the other features because of several pixels with 0 values, which was a result of the spatial nature of the feature. An interesting result in Figure 4 is that the time above threshold and radiance sum above threshold have similar appearance for their respective maps, but dissimilar distributions. The results in Figure 4 show that time above threshold is the most uniform feature overall in both the map appearance for the layer and the distribution of the pixel values (excluding border scan region).

Figure 5 (a) contains color maps of the 18 layers processed with the nominal laser parameter set. The thermal feature distributions of the part cross-section excluding border scan data are plotted in Figure 5 (b) for layers 1, 9, and 18 of the nominal section. Both the color maps and distributions show that there was minimal layer-to-layer variation that exists for the time above threshold. The slight differences that existed in the time above threshold were because of the laser raster pattern rotation and layer-to-layer powder bed variation, but these effects did not significantly impact the thermal history.

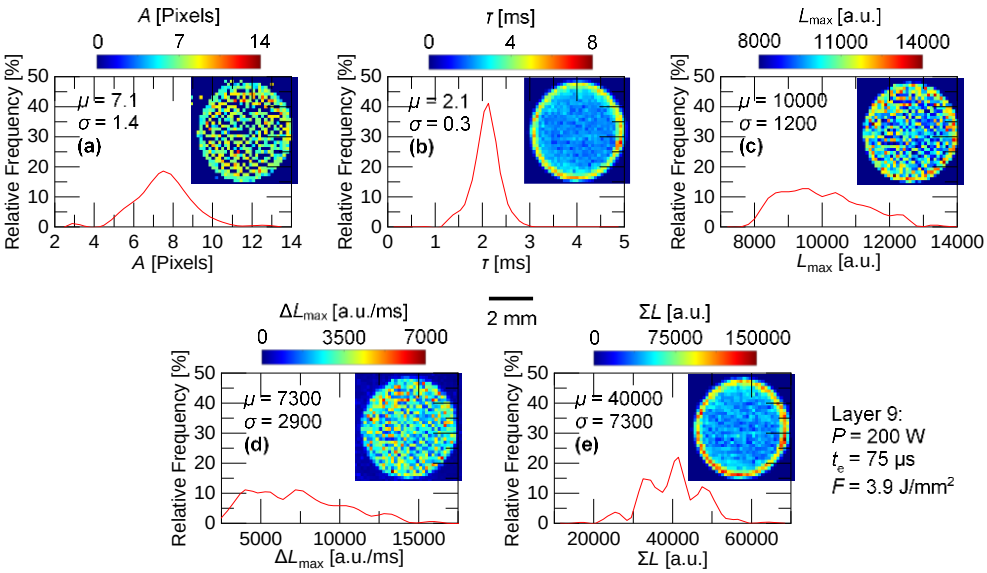

Figure 4. Distributions of the (a) apparent melt pool area, (b) time above threshold, (c) maximum radiance, (d) maximum radiance decrease rate, and (e) radiance sum above threshold, all excluding border scan data for a layer processed with the nominal laser parameter set.

The results in Figure 5 were consistent for the sections processed with other fluence values. This is demonstrated in Figure 6 (a) where the averages and standard deviations of the time above threshold for the minimum, nominal, and maximum fluence are plotted for each layer of the respective sections. Figure 6 (a) shows that no significant variation from layer-to-layer exists for the fluence values analyzed. This result means that the thermal features in the volume of each section in various process parameters recording sample can be treated as continuous distributions. The various sections in the recording sample were processed to determine an average and standard deviation for each thermal feature as a function of the fluence input. The data was first averaged across the build direction within the section corresponding to a single parameter. Figure 6 (b) contains the averaged time above threshold color maps for the cross-section of the

recording sample plotted for the various laser powers and exposure times used to manufacture the 20 partitions.

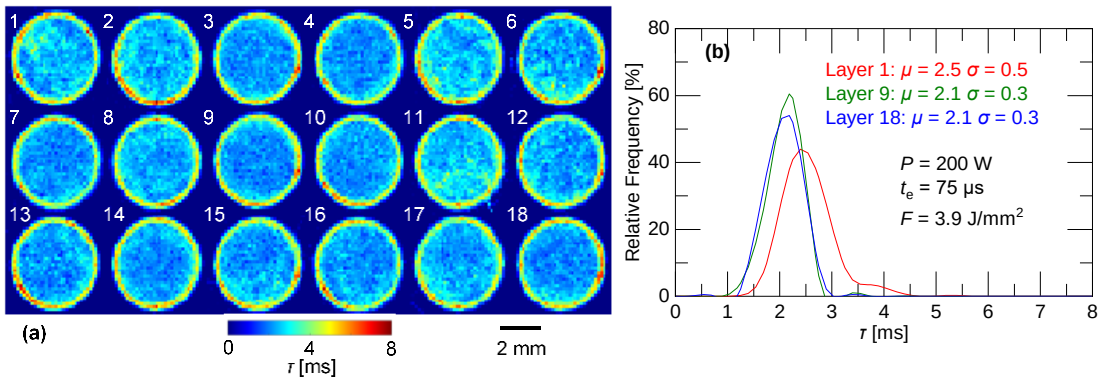

Figure 5. (a) Time above threshold maps for the layers processed with the nominal laser parameter set with (b) the feature value distributions for selected layers excluding border scan data.

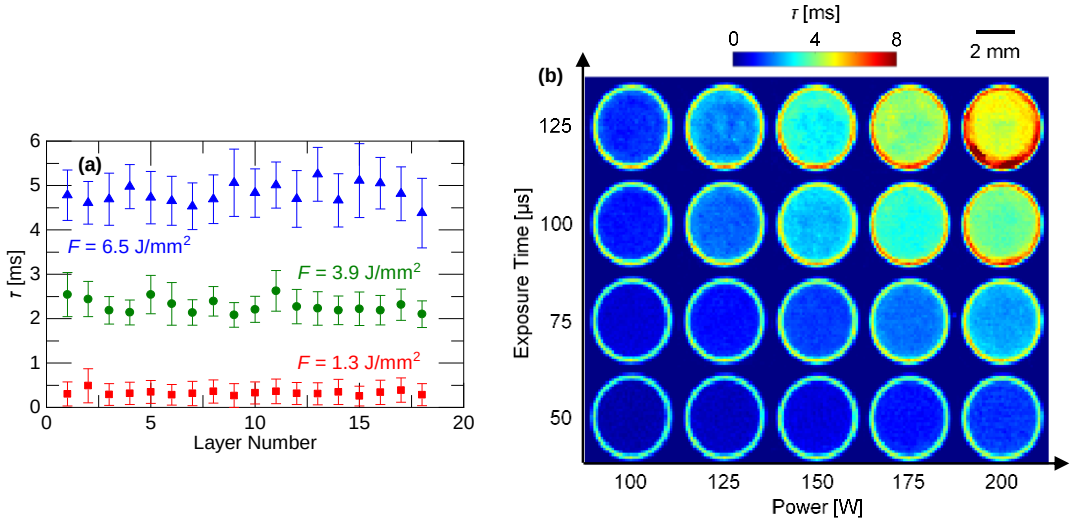

Figure 6. (a) Time above threshold for the layers corresponding to minimum, nominal, and maximum fluence input showing layer-to-layer consistency and (b) averaged time above threshold color maps for 20 process parameter sets of recording sample.

A qualitative observation of Figure 6 (b) shows there is an increase in the time above threshold with both increasing laser power and exposure time. The color maps in Figure 6 (b) also demonstrate the impacts that the laser cornering and border scans have on thermal feature extraction at the part edges for all process parameter combinations. Data sets similar to the time above threshold plots in Figure 6 (b) were generated for the remaining thermal features to determine their averages and standard deviations. These averaged thermal feature data sets were used to develop correlations with the fluence and part properties. The averaging was performed after spatially filtering the color maps to exclude the data from the border regions. The average thermal features with standard deviations are correlated with fluence in Figure 7 (a-e).

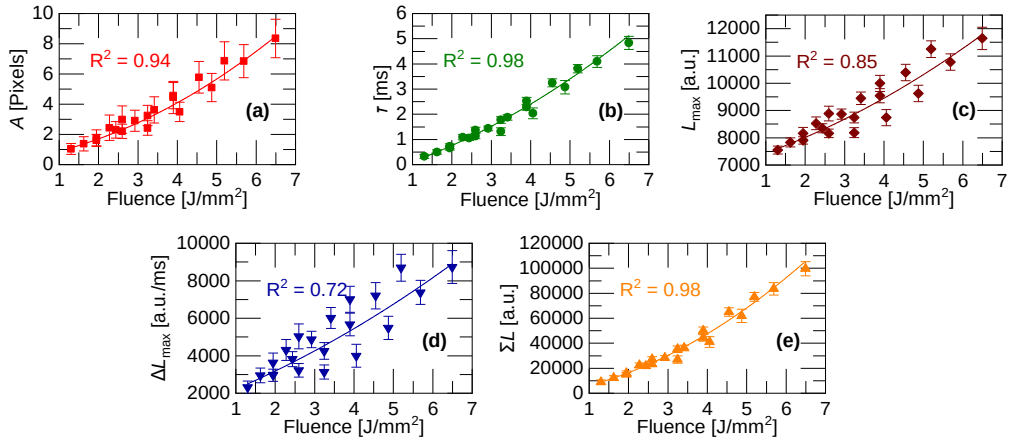

Figure 7. Correlations between (a) melt pool area, (b) time above threshold, (c) maximum radiance, (d) maximum radiance decrease rate, and (e) radiance sum above threshold and fluence.

Figure 7 shows the thermal features all increase with increasing fluence. The correlations for the various thermal features were fit to a second-order model for

evaluation of the strength of fit. The time above threshold and radiance sum above threshold were found to correlate the strongest with the fluence. This result is due to the similar integrated information captured by the extraction of those thermal features. The remaining thermal features have weaker correlations due to more spread across the fluence inputs. This is a result of increased sensitivity to the laser exposure time for those features. The thermal features are further evaluated in the next section by comparing their correlation strengths with bulk part properties.

4. CORRELATIONS OF THERMAL FEATURES WITH PART PROPERTIES

4.1. CORRELATIONS WITH BULK PART PROPERTIES

Figure 8 is the correlation of the averaged time above threshold with the part properties of yield strength and area percentage porosity. This correlation is representative of the trends observed for each thermal feature. As each thermal feature increased in value, the yield strength increased and then saturated at a maximum value, while the porosity decreased and then saturated at a minimum value. The capabilities of the thermal features extracted from the SWIR imaging data to predict LPBF part properties were evaluated by curve fitting the correlations with heuristic non-linear models. The non-linear model for the correlations between thermal features and the yield strength was

$$\sigma_y = A_1 \cdot \left[1 - \mathrm{e}^{-B_1 \cdot (x - C_1)}\right] \tag{7}$$

and the model for the correlations of the thermal features with the area percentage porosity was

$$\varphi = A_2 \cdot \mathrm{e}^{-B_2 \cdot (x - C_2)} . \quad (8)$$

In the models, *A*, *B*, and *C* are fitting parameters, and *x* is the thermal feature. The fits for the part properties as a function of the thermal feature are plotted as a black line. The 95% confidence intervals, CI, of the fit and the 95% prediction intervals, PI, for new data points were determined for each thermal feature by the non-linear regression. The 95% CI band for the fit is plotted in blue and the 95% PI band for a new data point is plotted in red in Figure 8. The plots demonstrate that the prediction intervals for yield strength allow more confidence in estimation of part performance than porosity. This is because the band widths for porosity are wider than the optimum less than 1% typically achieved during LPBF with nominal parameters. The band widths for yield strength are a small percentage of the mean values, which creates higher confidence.

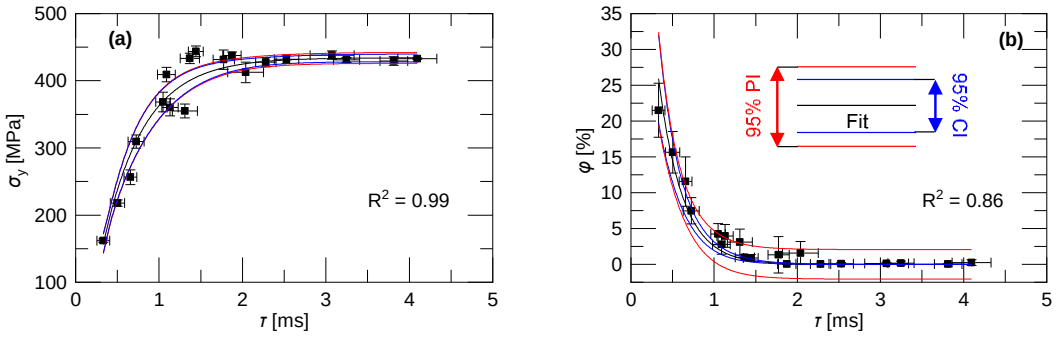

Figure 8. Correlations of (a) yield strength and (b) area percentage porosity with thermal feature of time above threshold.

The strength of fits, predictive capabilities, and processing times (Dell OptiPlex 5040, Intel Core i7-6700 CPU, 3.4 GHz) for the thermal features are reported in Table 2 for comparison. The correlation coefficients for the thermal features and the yield

strength were all similar. The correlation coefficients for the porosity fitting demonstrated that the thermal features again performed similarly except for a noticeably smaller value for maximum radiance decrease rate. All the thermal features can effectively be used by themselves to model and have the potential to predict the part properties. However, benefits exist in using the time above threshold, even though its processing time is the largest as seen in Table 2, and include its very strong correlation with both yield strength and area percentage porosity. Additionally, limitations to the other thermal features must be considered. One limitation is the influences of exposure time on the melt pool area, the maximum radiance, and the maximum radiance decrease rate slightly reduce their modeling ability when compared to the time above threshold because separate curves for these thermal features begin to appear with increasing exposure time. This is especially noticeable in the spread of the maximum radiance decrease rate plotted in Figure 7 (d). Also, digitization of the apparent melt pool area due to the camera's limited spatial resolution may lead to higher uncertainties in the thermal features [51].

Table 2. Correlation coefficients with fluence input, minimum prediction interval band widths from non-linear regression, and extraction processing times for various thermal features.

Thermal Feature	**Correlation Strength with Fluence**	**Correlation Strength with Yield Strength**	**Correlation Strength with Porosity**	**Yield Strength Prediction Interval [MPa]**	**Porosity Prediction Interval [%]**	**Processing Time for 900 Layers [s]**
A	0.94	0.99	0.84	±8	±2.2	910
τ	0.98	0.99	0.86	±8	±2.1	1370
L_{max}	0.85	0.98	0.87	±10	±1.9	490
ΔL_{max}	0.72	0.97	0.77	±13	±2.6	690
ΣL	0.98	0.99	0.84	±9	±2.1	1000

The results in Figure 6 through Figure 8 establish the process parameter effects observable by the SWIR imaging framework. While in these nominal cases the part properties could be correlated directly to the process parameters, the framework can be extended to various scenarios where the direct relationships could fail. The scenarios include large variances in the thermal histories of parts processed with complex scan pathing due complicated geometries and machine state changes. Examples of machine state change include a drop in the recirculated Argon flow due to filter contamination and attenuation of the fluence reaching the powder bed due to deposition of vaporized material on the *f*-θ lens' protective window. The deposition can be non-uniform across the window and lead to sub-optimal fluence input (causing defects) for specific areas on the build plate. The SWIR imaging framework would automatically monitor the variation in the thermal features and indicate the corresponding mechanical property values for parts manufactured in these scenarios.

4.2. DISTINGUISHING PROCESSING MODES

The use of multiple thermal features in the development of correlations provided a unique advantage over the use of a single feature in distinguishing the processing modes that led to differences in part properties. The thermal features were first correlated with each other and then a color map was assigned based on the corresponding part property values to demonstrate this ability. Figure 9 summarizes the correlation between the various thermal features and the time above threshold (taken as baseline for this analysis due to discussed strengths). The correlation of the maximum radiance decrease rate with

the time above threshold is plotted in Figure 9 (a) and the correlation coefficients for a linear fit are tabulated in Figure 9 (b) for the remaining thermal features.

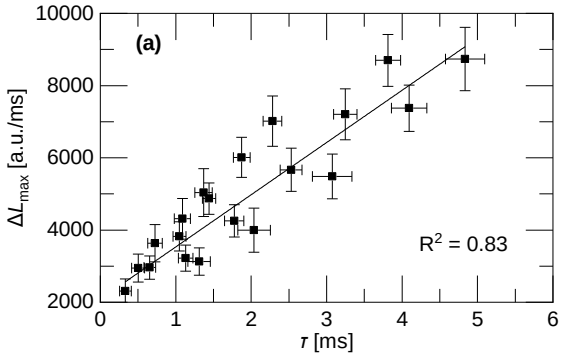

(b)

Thermal Feature	Correlation Strength with τ
A	0.99
L_{max}	0.93
ΔL_{max}	0.83
ΣL	0.99

Figure 9. (a) Correlation of the maximum radiance decrease rate with the time above threshold and (b) summary of the linear correlation strengths for the various thermal features with the time above threshold.

Figure 10 demonstrates the use of the maximum radiance decrease rate with the time above threshold to distinguish part performance by developing color maps of the yield strength and porosity. The maximum radiance decrease rate was selected because it had the weakest correlation with time above threshold, which resulted in a larger feature space in the part property mapping. Figure 10 (a) is the map for yield strength (color scale is linear) and Figure 10 (b) is the map for porosity (color scale is logarithmic). Porosity modes were assigned to the thermal feature space in Figure 10 (a) and (b) based on observations in optical micrographs. Porosity mode 1 corresponds to lack of fusion porosity and occurs in the low time above threshold and maximum radiance decrease rate space. Porosity mode 2 is the minimization of lack of fusion and keyhole porosity and occurs for a narrow band in the time above threshold and maximum radiance decrease rate space. Porosity mode 3 is an increase in porosity due to keyholing that corresponds

to a larger band in the higher time above thresholds and radiance decrease rate space. Figure 10 (c) demonstrates the various porosity modes in representative optical micrographs. Figure 10 (a) shows that the optimum yield strength value was found for each porosity case indicating a lack of sensitivity to processing mode. The thermal feature mapping distinguishes the processing modes and can be used to determine parts with excessive porosity, even though they may have the nominal yield strength. The results suggest that the weakly related thermal features are capturing different phenomenon in LPBF and can be used to provide guidance in the future development of more instructive thermal features that can distinguish processing modes with their standalone use.

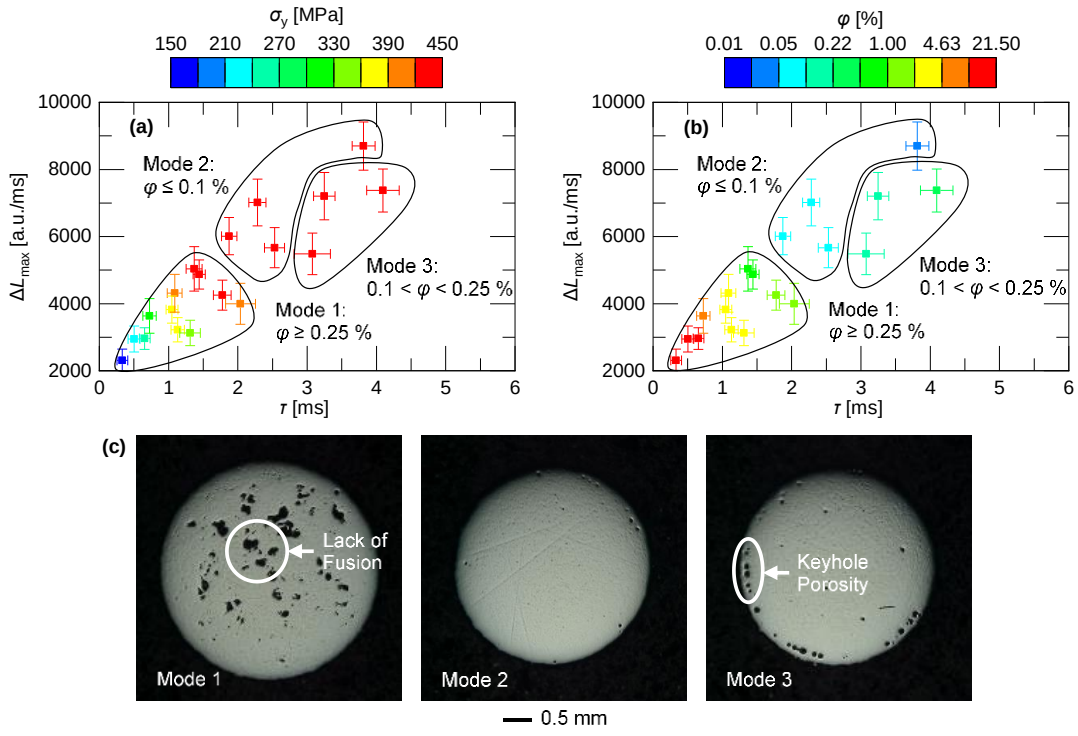

Figure 10. (a) Yield strength and (b) porosity mapped correlation of maximum radiance decrease rate with time above threshold and (c) various porosity modes in optical micrographs of polished sample cross-sections.

4.3. RELATIONSHIPS WITH LOCAL STATE

The correlation of bulk part properties with SWIR imaging data can be expanded to a comparison of in-situ thermal feature reconstruction characteristics with local state information obtained by ex-situ μCT scanning. A 4 mm diameter cylindrical sample was built with an embedded feature. The feature consisted of internal scan pathing with increased complexities due to embedded text, *KCNSC – MST*, processed with an off nominal laser power of 100 W. The bulk of the sample was processed with the nominal parameters (P = 200 W, t_e = 75 μs) and internal border scans around the feature were applied. Processing the sample with the embedded feature resulted in different phenomena, which included insufficient melting due to the low laser power and differences in state due to re-melting effects. While these features were driven by the embedded text, they correspond to events that occur naturally in LPBF due to complex scan pathing, or attenuation in the fluence.

Figure 11 (a) and (b) contain the voxel reconstructions from μCT scanning and SWIR imaging of the embedded feature sample, respectively. The μCT voxel data contains gray scale values of arbitrary units and the SWIR imaging data is the time above threshold. Figure 11 (a) and (b) include a sliced view parallel to the build direction at the middle of the sample volume, a magnification of the *MST*, and three layers (326,424,442) for both reconstructions. The layers were selected based on the representative features that they contained for the sample. Layer 326 contains differences in local state due to the low laser power, layer 424 contains features from re-melting effects, and layer 442 is nominal. A qualitative comparison of the reconstructions demonstrates that the SWIR imaging data contains features that indicate the differences in local state measured by

µCT. The differences in local state corresponded to the defect of porosity within the volume of the sample. Some discrepancies exist between the µCT data and SWIR imaging reconstruction due to re-melting effects from layer-to-layer and keyhole porosity appearing below the layer indicating the defect. This is because keyhole porosity generally forms at the bottom of the melt pool during a collapse.

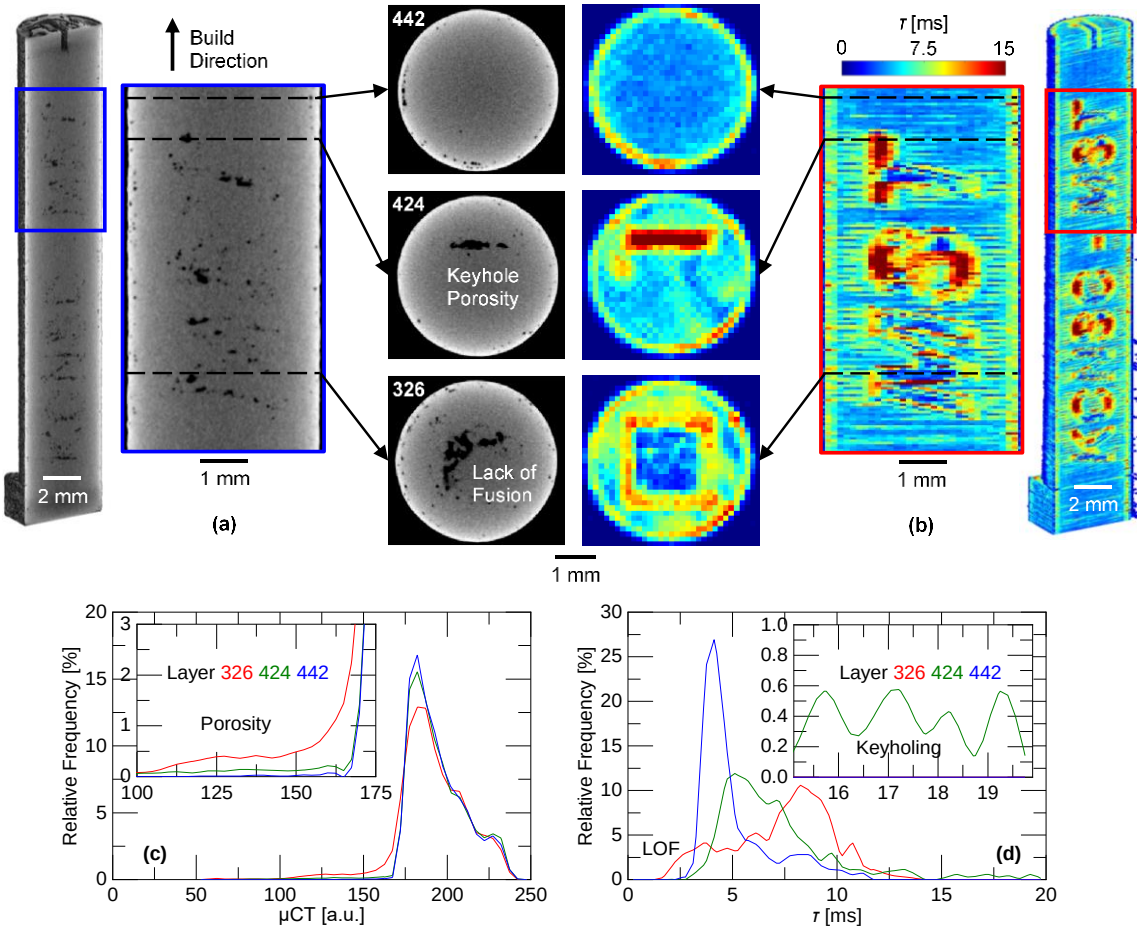

Figure 11. (a) ex-situ µCT scan results, (b) time above threshold reconstruction for the embedded feature sample and distributions of (c) the µCT data and (d) the thermal feature data for the selected layers.

In addition to qualitative observations, the three layers' uniformities were compared by plotting the distributions of the voxel values for both data sets in Figure 11 (c) and (d). The distribution plots exclude data outside of the sample's border. An inset demonstrating the values corresponding to porosity in the μCT data is included in Figure 11 (c). Layer 326 has the largest amount of porosity in the μCT reconstruction and the most voxels less than 3 ms in the time above threshold data. An interesting result for this layer is observed in Figure 11 (d) where the distribution is shifted towards higher time above threshold values. This is unexpected for a layer with an area processed by the suboptimal laser power and is due to an increased time above threshold for the shorter scan path lengths used to process the surrounding nominal geometry. Layer 424 contains an increase in interior porosity due to re-melting at the *T*. This is demonstrated in the histogram for the μCT data by an increase in voxel values less than 175 a.u. and for the SWIR data by a broadening of the distribution and multiple voxels with values greater than 15 ms that are observable in Figure 11 (d)'s inset. The interior of layer 442 is uniform for both the μCT and SWIR imaging reconstructions, while the periphery contains porosity and higher time above threshold values due to the laser cornering and border scans.

Keyholing is likely to be the cause of the large porosity in layer 424 based on the very high time above threshold values present at the defect location; however, the cause of the porosity in layer 326 is not obvious. The methods discussed in Section 4.2 were applied to determine the processing mode present in layer 326. The area of layer 326 with the majority of porosity at the interior experienced a low time above threshold and a very low maximum radiance decrease rate (not shown). This corresponds to processing mode

1 (lack of fusion). The edges of this area were processed with border scans and contain porosity with a more spherical morphology consistent with mode 3. This was confirmed by the higher time above threshold and a low maximum radiance decrease rate present at the border areas. These results further suggest that the SWIR imaging framework is able to distinguish the processing mode present, even if there is mixed mode processing, for a LPBF sample built with complex scan pathing.

The results in Figure 11 demonstrate that the in-situ SWIR imaging framework's voxel based reconstructions capture the differences in the physical features observed in the μCT data of the sample and validate the promising opportunity in future work to locally predict and non-destructively qualify part properties. Additionally, analysis of the SWIR data on a layer-by-layer basis lends itself to application in statistical process control. For example, the distribution of the thermal features in a nominal layer could be used to establish control charts. Layers with enough voxels outside of tolerance could be flagged as defective. In the study presented here, observation of Figure 11 (d) shows that layers 326 and 424 would be flagged relative to the nominal layer. Applying this technique in-situ provides the opportunity to make corrections on a layer-to-layer basis in addition to part qualification.

5. SUMMARY AND CONCLUSIONS

In this paper, an in-situ LPBF process monitoring framework incorporating layer-to-layer SWIR imaging was used to generate voxel data for parts based on thermal features extracted from time-series data. The framework was used for processing 304L

stainless steel with a Renishaw AM250, but has the capability to be adapted to different part materials and machine platforms. The use of this framework in the construction and subsequent averaging approach processing of voxel based thermal data for LPBF parts enabled the correlation of various extracted thermal features to bulk properties including the yield strength and the area percentage porosity. The predictive capabilities of the various thermal features extracted in this work were compared by evaluating their respective correlation strengths with the part properties. The thermal feature of time above threshold, radiance sum above threshold, and melt pool area resulted in the strongest correlations with the yield strength (0.99) and the maximum radiance correlated the best with the area percentage porosity (0.87). Through the averaging approach analysis, it was found that the time above threshold and the melt pool area demonstrated the strongest predictive capabilities for the yield strength. The maximum radiance resulted in the strongest predictive capability for the area percentage porosity. The correlations developed for the thermal features have the possibility to estimate the yield strength to ±8 MPa and porosity levels to ±1.9% for new measurements. The voxel based framework was also used to generate a full 3D reconstruction of a sample with an embedded internal feature for comparison with μCT data.

The quantitative analysis with bulk properties and the demonstration of the relationship between thermal features and local state from ex-situ μCT scanning in this work motivate the use of SWIR imaging measurements to qualify LPBF parts consisting of simple geometries processed with complex scan pathing. The information obtained in the thermal feature analysis provides the opportunity to flag parts with predicted mechanical properties that are suboptimal, or that include defects on a localized basis.

While the SWIR imaging framework has shown success, there are some limitations. The predictive capabilities of the bulk part property models should be validated for complex geometries where cooling paths are significantly different (e.g., overhang structures, lattice geometries) before implementation in qualification. The framework should also be tested for the accuracy of predictions in cases of significant changes in the layer-to-layer processing time where the differences in temperature for parts at the start of the layer may impact the thermal feature values input into the part property models. Finally, the framework may fail to capture the negative effects of global events that occur at lower temperatures such as part deformation due to thermal stress. The developed framework will be further evaluated for local part properties predictions by comparing thermal feature voxel based data with results from experimental measurements.

ACKNOWLEDGEMENT

This work was funded by Honeywell Federal Manufacturing & Technologies under Contract No. DE-NA0002839 with the U.S. Department of Energy. The United States Government retains and the publisher, by accepting the article for publication, acknowledges that the United States Government retains a nonexclusive, paid up, irrevocable, world-wide license to publish or reproduce the published form of this manuscript, or allow others to do so, for the United States Government purposes.

REFERENCES

[1] Z. Wang, T.A. Palmer, A.M. Beese, Effect of processing parameters on microstructure and tensile properties of austenitic stainless steel 304L made by directed energy deposition additive manufacturing, Acta Mater. 110 (2016) 226–235. https://doi.org/10.1016/j.actamat.2016.03.019.

[2] M. Taheri Andani, R. Dehghani, M.R. Karamooz-Ravari, R. Mirzaeifar, J. Ni, A study on the effect of energy input on spatter particles creation during selective laser melting process, Addit. Manuf. 20 (2018) 33–43. https://doi.org/10.1016/j.addma.2017.12.009.

[3] C. Gobert, E.W. Reutzel, J. Petrich, A.R. Nassar, S. Phoha, Application of supervised machine learning for defect detection during metallic powder bed fusion additive manufacturing using high resolution imaging., Addit. Manuf. 21 (2018) 517–528. https://doi.org/10.1016/j.addma.2018.04.005.

[4] V. Gunenthiram, P. Peyre, M. Schneider, M. Dal, F. Coste, I. Koutiri, R. Fabbro, Experimental analysis of spatter generation and melt-pool behavior during the powder bed laser beam melting process, J. Mater. Process. Technol. 251 (2018) 376–386. https://doi.org/10.1016/j.jmatprotec.2017.08.012.

[5] M. Abdelrahman, E.W. Reutzel, A.R. Nassar, T.L. Starr, Flaw detection in powder bed fusion using optical imaging, Addit. Manuf. 15 (2017) 1–11. https://doi.org/10.1016/j.addma.2017.02.001.

[6] J.A. Kanko, A.P. Sibley, J.M. Fraser, In situ morphology-based defect detection of selective laser melting through inline coherent imaging, J. Mater. Process. Technol. 231 (2016) 488–500. https://doi.org/10.1016/j.jmatprotec.2015.12.024.

[7] M. Grasso, V. Laguzza, Q. Semeraro, B.M. Colosimo, In-Process Monitoring of Selective Laser Melting: Spatial Detection of Defects Via Image Data Analysis, J. Manuf. Sci. Eng. Trans. ASME. 139 (2017) 1–16. https://doi.org/10.1115/1.4034715.

[8] U. Scipioni Bertoli, G. Guss, S. Wu, M.J. Matthews, J.M. Schoenung, In-situ characterization of laser-powder interaction and cooling rates through high-speed imaging of powder bed fusion additive manufacturing, Mater. Des. 135 (2017) 385–396. https://doi.org/10.1016/j.matdes.2017.09.044.

[9] G. Repossini, V. Laguzza, M. Grasso, B.M. Colosimo, On the use of spatter signature for in-situ monitoring of Laser Powder Bed Fusion, Addit. Manuf. 16 (2017) 35–48. https://doi.org/10.1016/j.addma.2017.05.004.

[10] M. Doubenskaia, S. Grigoriev, I. Zhirnov, I. Smurov, Parametric analysis of SLM using comprehensive optical monitoring, Rapid Prototyp. J. 22 (2016) 40–50. https://doi.org/10.1108/RPJ-04-2014-0046.

[11] F. Imani, A. Gaikwad, M. Montazeri, P. Rao, H. Yang, E. Reutzel, Process mapping and in-process monitoring of porosity in laser powder bed fusion using layerwise optical imaging, J. Manuf. Sci. Eng. Trans. ASME. 140 (2018). https://doi.org/10.1115/1.4040615.

[12] L. Scime, J. Beuth, Using machine learning to identify in-situ melt pool signatures indicative of flaw formation in a laser powder bed fusion additive manufacturing process, Addit. Manuf. 25 (2019) 151–165. https://doi.org/10.1016/j.addma.2018.11.010.

[13] B. Cheng, J. Lydon, K. Cooper, V. Cole, P. Northrop, K. Chou, Infrared thermal imaging for melt pool analysis in SLM: a feasibility investigation, Virtual Phys. Prototyp. 13 (2018) 8–13. https://doi.org/10.1080/17452759.2017.1392685.

[14] S. Price, K. Cooper, K. Chou, Evaluations of temperature measurements by near-infrared thermography in powder-based electron-beam additive manufacturing, Proceedings of Solid Freeform Fabrication Symposium (2012).

[15] D. Ye, J.Y. Hsi Fuh, Y. Zhang, G.S. Hong, K. Zhu, In situ monitoring of selective laser melting using plume and spatter signatures by deep belief networks, ISA Trans. 81 (2018) 96–104. https://doi.org/10.1016/j.isatra.2018.07.021.

[16] Y. Zhang, J.Y.H. Fuh, D. Ye, G.S. Hong, In-situ monitoring of laser-based PBF via off-axis vision and image processing approaches, Addit. Manuf. 25 (2019) 263–274. https://doi.org/10.1016/j.addma.2018.10.020.

[17] B. Cheng, J. Lydon, K. Cooper, V. Cole, P. Northrop, K. Chou, Melt pool sensing and size analysis in laser powder-bed metal additive manufacturing, J. Manuf. Process. 32 (2018) 744–753. https://doi.org/10.1016/j.jmapro.2018.04.002.

[18] S. Price, B. Cheng, J. Lydon, K. Cooper, K. Chou, On Process Temperature in Powder-Bed Electron Beam Additive Manufacturing: Process Parameter Effects, J. Manuf. Sci. Eng. Trans. ASME. 136 (2014) 1–10. https://doi.org/10.1115/1.4028485.

[19] N. Boone, C. Zhu, C. Smith, I. Todd, J.R. Willmott, Thermal near infrared monitoring system for electron beam melting with emissivity tracking, Addit. Manuf. 22 (2018) 601–605. https://doi.org/10.1016/j.addma.2018.06.004.

[20] J. Heigel, B. Lane, The effect of powder on cooling rate and melt pool length measurements using in situ thermographic techniques, Proceedings of Solid Freeform Fabrication Symposium (2017).

[21] J.C. Heigel, B.M. Lane, Measurement of the Melt Pool Length during Single Scan Tracks in a Commercial Laser Powder Bed Fusion Process, J. Manuf. Sci. Eng. Trans. ASME. 140 (2018) 1–7. https://doi.org/10.1115/1.4037571.

[22] M. Montazeri, P. Rao, Sensor-Based Build Condition Monitoring in Laser Powder Bed Fusion Additive Manufacturing Process Using a Spectral Graph Theoretic Approach, J. Manuf. Sci. Eng. Trans. ASME. 140 (2018). https://doi.org/10.1115/1.4040264.

[23] B. Lane, S. Moylan, E.P. Whitenton, L. Ma, Thermographic measurements of the commercial laser powder bed fusion process at NIST, Rapid Prototyp. J. 22 (2016) 778–787. https://doi.org/10.1108/RPJ-11-2015-0161.

[24] M.A. Doubenskaia, I.V. Zhirnov, V.I. Teleshevskiy, P. Bertrand, I.Y. Smurov, Determination of true temperature in selective laser melting of metal powder using infrared camera, Mater. Sci. Forum. 834 (2015) 93–102. https://doi.org/10.4028/www.scientific.net/MSF.834.93.

[25] J. Raplee, A. Plotkowski, M.M. Kirka, R. Dinwiddie, A. Okello, R.R. Dehoff, S.S. Babu, Thermographic Microstructure Monitoring in Electron Beam Additive Manufacturing, Sci. Rep. 7 (2017) 1–16. https://doi.org/10.1038/srep43554.

[26] H. Krauss, C. Eschey, M. Zaeh, Thermography for monitoring the selective laser melting process, Proceedings of Solid Freeform Fabrication Symposium (2012).

[27] M. Grasso, A.G. Demir, B. Previtali, B.M. Colosimo, In situ monitoring of selective laser melting of zinc powder via infrared imaging of the process plume, Robot. Comput. Integr. Manuf. 49 (2018) 229–239. https://doi.org/10.1016/j.rcim.2017.07.001.

[28] E. Rodriguez, J. Mireles, C.A. Terrazas, D. Espalin, M.A. Perez, R.B. Wicker, Approximation of absolute surface temperature measurements of powder bed fusion additive manufacturing technology using in situ infrared thermography, Addit. Manuf. 5 (2015) 31–39. https://doi.org/10.1016/j.addma.2014.12.001.

[29] M. Grasso, B.M. Colosimo, A statistical learning method for image-based monitoring of the plume signature in laser powder bed fusion, Robot. Comput. Integr. Manuf. 57 (2019) 103–115. https://doi.org/10.1016/j.rcim.2018.11.007.

[30] M. Khanzadeh, W. Tian, A. Yadollahi, H.R. Doude, M.A. Tschopp, L. Bian, Dual process monitoring of metal-based additive manufacturing using tensor decomposition of thermal image streams, Addit. Manuf. 23 (2018) 443–456. https://doi.org/10.1016/j.addma.2018.08.014.

[31] M. Mahmoudi, A.A. Ezzat, A. Elwany, Layerwise Anomaly Detection in Laser Powder-Bed Fusion Metal Additive Manufacturing, J. Manuf. Sci. Eng. Trans. ASME. 141 (2019) 1–13. https://doi.org/10.1115/1.4042108.

[32] P.A. Hooper, Melt pool temperature and cooling rates in laser powder bed fusion, Addit. Manuf. 22 (2018) 548–559. https://doi.org/10.1016/j.addma.2018.05.032.

[33] J. Mireles, S. Ridwan, P.A. Morton, A. Hinojos, R.B. Wicker, Analysis and correction of defects within parts fabricated using powder bed fusion technology, Surf. Topogr. Metrol. Prop. 3 (2015). https://doi.org/10.1088/2051-672X/3/3/034002.

[34] T. Craeghs, S. Clijsters, J.P. Kruth, F. Bechmann, M.C. Ebert, Detection of Process Failures in Layerwise Laser Melting with Optical Process Monitoring, Phys. Procedia. 39 (2012) 753–759. https://doi.org/10.1016/j.phpro.2012.10.097.

[35] Z. Li, X. Liu, S. Wen, P. He, K. Zhong, Q. Wei, Y. Shi, S. Liu, In situ 3D monitoring of geometric signatures in the powder-bed-fusion additive manufacturing process via vision sensing methods, Sensors (Switzerland). 18 (2018). https://doi.org/10.3390/s18041180.

[36] J.L. Bartlett, F.M. Heim, Y. V. Murty, X. Li, In situ defect detection in selective laser melting via full-field infrared thermography, Addit. Manuf. 24 (2018) 595–605. https://doi.org/10.1016/j.addma.2018.10.045.

[37] H. Krauss, T. Zeugner, M.F. Zaeh, Layerwise monitoring of the Selective Laser Melting process by thermography, Phys. Procedia. 56 (2014) 64–71. https://doi.org/10.1016/j.phpro.2014.08.097.

[38] J.C. Heigel, E. Whitenton, Measurement of thermal processing variability in powder bed fusion, Proc. - 2018 ASPE Euspen Summer Top. Meet. Adv. Precis. Addit. Manuf. 69 (2018) 242–247.

[39] H. Krauss, T. Zeugner, M.F. Zaeh, Thermographic process monitoring in powderbed based additive manufacturing, AIP Conf. Proc. 1650 (2015) 177–183. https://doi.org/10.1063/1.4914608.

[40] V. Carl, Monitoring system for the quality assessment in additive manufacturing, AIP Conf. Proc. 1650 (2015) 171–176. https://doi.org/10.1063/1.4914607.

[41] M. Bisht, N. Ray, F. Verbist, S. Coeck, Correlation of selective laser melting-melt pool events with the tensile properties of Ti-6Al-4V ELI processed by laser powder bed fusion, Addit. Manuf. 22 (2018) 302–306. https://doi.org/10.1016/j.addma.2018.05.004.

[42] S. Coeck, M. Bisht, J. Plas, F. Verbist, Prediction of lack of fusion porosity in selective laser melting based on melt pool monitoring data, Addit. Manuf. 25 (2019) 347–356. https://doi.org/10.1016/j.addma.2018.11.015.

[43] D. Alberts, D. Schwarze, G. Witt, In Situ Melt Pool Monitoring and the Correlation to Part Density of Inconel 718 for Quality Assurance in Selective Laser Melting, Proceedings of Solid Freeform Fabrication Symposium (2017).

[44] A. Gökhan Demir, C. De Giorgi, B. Previtali, Design and Implementation of a Multisensor Coaxial Monitoring System with Correction Strategies for Selective Laser Melting of a Maraging Steel, J. Manuf. Sci. Eng. Trans. ASME. 140 (2018) 1–14. https://doi.org/10.1115/1.4038568.

[45] S.J. Foster, K. Carver, R.B. Dinwiddie, F. List, K.A. Unocic, A. Chaudhary, S.S. Babu, Process-Defect-Structure-Property Correlations During Laser Powder Bed Fusion of Alloy 718: Role of In Situ and Ex Situ Characterizations, Metall. Mater. Trans. A Phys. Metall. Mater. Sci. 49 (2018) 5775–5798. https://doi.org/10.1007/s11661-018-4870-2.

[46] S. Yoder, P. Nandwana, V. Paquit, M. Kirka, A. Scopel, R.R. Dehoff, S.S. Babu, Approach to qualification using E-PBF in-situ process monitoring in Ti-6Al-4V, Addit. Manuf. 28 (2019) 98–106. https://doi.org/10.1016/j.addma.2019.03.021.

[47] Q.Y. Lu, N.V. Nguyen, A.J.W. Hum, T. Tran, C.H. Wong, Optical in-situ monitoring and correlation of density and mechanical properties of stainless steel parts produced by selective laser melting process based on varied energy density, J. Mater. Process. Technol. 271 (2019) 520–531. https://doi.org/10.1016/j.jmatprotec.2019.04.026.

[48] ASTM E8/E8M Standard Test Methods for Tension Testing of Metallic Materials, ASTM International, West Conshohocken, PA, (2016).

[49] ASTM E2109 Determining Area Percentage Porosity in Thermal Sprayed Coatings, ASTM International, West Conshohocken, PA, (2014).

[50] P. Wang, X. Tan, C. He, M.L.S. Nai, R. Huang, S.B. Tor, J. Wei, Scanning optical microscopy for porosity quantification of additively manufactured components, Addit. Manuf. 21 (2018) 350–358. https://doi.org/10.1016/j.addma.2018.03.019.

[51] X. Wang, C.S. Lough, D.A. Bristow, R.G. Landers, E.C. Kinzel, Effects of thermal camera resolution on feature extraction in selective laser melting, Proceedings of Solid Freeform Fabrication Symposium (2018).

III. LOCAL PREDICTION OF LASER POWDER BED FUSION POROSITY BY SHORT-WAVE INFRARED IMAGING

Cody S. Lough[1], Tao Liu[1], Xin Wang[1], Ben Brown[2], Robert G. Landers[1], Douglas A. Bristow[1], James A. Drallmeier[1], Edward C. Kinzel[3]

[1]Department of Mechanical and Aerospace Engineering, Missouri University of Science and Technology, Rolla, MO 65409

[2]Kansas City National Security Campus*, Kansas City, MO 64147

[3]Department of Aerospace and Mechanical Engineering, University of Notre Dame, Notre Dame, IN 46556

*The Department of Energy's Kansas City National Security Campus is operated and managed by Honeywell Federal Manufacturing & Technologies, LLC under contract number DE-NA0002839.

ABSTRACT

The local thermal history can significantly vary in parts during metal Additive Manufacturing (AM) leading to local defects. The sequential layer-by-layer nature of AM facilitates in-situ part voxelmetric observations. The challenge is to relate this local radiometric data with local defect information to estimate process error likelihood. These predictions have application in both part qualification and control. This paper uses a Short-Wave Infrared (SWIR) camera to record the temperature history for parts manufactured with Laser Powder Bed Fusion (LPBF). The defects from a simple cylindrical specimen are measured by ex-situ micro-computed tomography (μCT). Data from the SWIR camera of this specimen, combined with the μCT data, are used to train thermal feature-based porosity probability models. The porosity predictions made by

various SWIR thermal feature-porosity probability models of a specimen with a complex geometry are scored against the true porosity obtained via μCT. The results from the complex specimen demonstrate that approximately 88% of the porosity identified in μCT data is correctly predicted, with a 27% false positive rate, through the utilization of the constructed probability models.

1. INTRODUCTION

The expanding presence of metal Additive Manufacturing (AM) in industry has increased the need for qualification of parts with complexities unseen in those built by traditional manufacturing processes. Laser Powder Bed Fusion (LPBF) is an established AM technology that produces intricate part geometries with high resolutions by leveraging micron scale melt pool sizes and layer thicknesses. Parts manufactured with this laser driven process experience significant thermal variations at a local level due to changing scan pathing and heat transfer boundary conditions. The defects (e.g., lack of fusion, keyholing porosity, balling) depend on the melting modes and are difficult, if not impossible, to design out of the process due to the inherent thermal variations. An understanding of the correlation between the measured thermal history and defects is needed for part/process qualification. The layer-to-layer material addition in LPBF permits the ability to interrogate the thermal history at every point in a part through in-situ radiometry. The information obtained from the non-contact measurements can identify part thermal variances and, thus, the locations with a high probability for defects.

The development of local part property prediction maps based on thermal measurements allows microstructure state estimation to aid the qualification of mission critical parts.

Porosity is an extensively studied defect for LPBF due to the difficulties eliminating it from the manufacturing process and the negative impacts it has on the mechanical performance of parts. Various types of porosity exist with classifications based on the dynamics leading to its formation. Gong et al. defined four processing regimes for LPBF of Ti-6Al-4V according to the resulting porosity/defect type [1]. The regimes include fully dense, over melting, incomplete melting, and overheating. The porosity occurring in the over melting regime is primarily a result of keyholing. The incomplete melting, or lack of fusion, porosity occurs when insufficient energy to sinter the powder particles is delivered to the powder bed. The porosity types are minimized in the nominal region. Wide ranging studies have aimed understand under what conditions the various porosity types occur. King et al. implemented a normalized enthalpy calculation based on LPBF parameters to determine where conduction mode melting transitioned to keyholing and applied this analysis to single track experiments [2]. Wang et al. combined analytically determined melt pool measurements with powder packing information to understand lack of fusion porosity's sensitivity to processing parameters [3]. Hojjatzadeh et al. used high-speed X-ray imaging to determine various phenomenon leading to LPBF porosity formation including, and beyond keyholing [4]. These studies help guide LPBF process development towards a reduction of porosity by understanding the physics; however, porosity will still exist in real manufacturing scenarios. This motivates the need for in-situ measurement-based porosity detection.

Studies have used various in-line, or staring configured instruments including visible cameras, infrared cameras, pyrometers, and photodiodes to obtain information (apparent melt pool geometry, intensity/temperature, laser spatter, etc.) from radiometric signals during powder bed fusion AM. Craeghs et al. demonstrated that the melt pool area from time series imaging measurements can be processed into 2D feature maps that indicate part failures [5]. Krauss et al. evaluated how averaged mapped measurements progress layer-wise [6]. Methods implementing thermography and pyrometry have identified embedded voids and naturally occurring porosity in powder bed fusion AM parts. Mireles et al. acquired infrared camera images to detect various geometry voids down to 600 μm designed into a part manufactured by Electron Beam Melting (EBM) [7]. Bartlett et al. used Long-Wave Infrared (LWIR) images captured after the raster in LPBF to identify subsurface defects for samples manufactured with baseline and porosity promoting parameters [8]. Yoder et al. demonstrated that features in voxel reconstructions based on static Near Infrared (NIR) images captured after each layer correlate to porosity resulting from a decrease in layer-to-layer time in EBM of Ti-6Al-4V [9]. Mitchell et al. detected voids manufactured within a LPBF part down to 120 μm by volumetric reconstructions of thermal data and successfully correlated locations of natural porosity with outlier melt pool images through two color pyrometry [10]. Mohr et al. found promising results when analyzing the overlap of porosity from micro-computed tomography (μCT) scanning and anomalies in volumetric thermal feature data for a single LPBF sample manufactured with three parameter sets, and two overhang conditions [11]. They demonstrated that approximately 71% of the pores in the sample's CT data were encompassed by the anomalous thermal features. These studies strongly

suggest local prediction of porosity is possible via in-situ measurements. Coeck et al. demonstrated the porosity prediction potential for LPBF of Ti-6Al-4V in a study that implemented measurements from two off-axis photodiodes [12]. The photodiode data produced melt pool intensity reconstructions of samples for which anomalies were correlated with porosity in CT scans. The framework identified 54 out of 93 pores with 61 false positives (36 true positives out of 39 pores that were 0.0015 mm^3 or larger).

Machine learning is one possible way to predict porosity, and some works that classify thermal measurements have been conducted. Khanzadeh et al. used supervised learning to categorize thermography acquired melt pool images as pores or nominal for laser engineered net shaping [13]. For powder bed based AM, Kwon et al. implemented deep neural networks to identify melt pool images measured with a high speed camera according to the laser power used in manufacturing [14]. Scime and Beuth used unsupervised machine learning to link high speed imaging melt pools with parameter spaces associated defects by multiple gradient features for LPBF of IN718 [15]. Baumgartl et al. identified areas in a thermal image acquired during LPBF that corresponded to delamination by a convolutional neural deep network [16]. Gaikwad et al. reported in-situ measurement classifications are improved for processing regime physics informed machine learning in an exhaustive 316L stainless steel single-track study [17]. Statistical training is a less complex alternative to machine learning for porosity prediction. Forien et al. studied the correlation between in-situ pyrometry measurements and porosity obtained by ex-situ X-ray imaging for single laser scans of 316L stainless steel [18]. Thermal and porosity data sets from various laser parameters provided pyrometer signal distributions corresponding to nominal material and pores.

These distributions defined the probability of keyholing porosity for a given pyrometer measurement. Forien et al. concluded that probabilistic predictions of keyholing porosity during LPBF is possible.

In-situ radiometry has been established as a feasible tool to identify porosity in LPBF parts through thermal history anomaly correlations. Studies demonstrated that machine learning is a powerful, but complex, way to categorize anomalies in thermal measurements for prediction applications. One study reveals a simpler method to classify thermal measurements by statistical mappings that define the probability at which porosity occurs. This leads us to explore the knowledge gap: can statistical maps informed by in-situ thermographic measurements be used to locally predict porosity in LPBF parts for real manufacturing scenarios? In this paper, probability maps based on Short-Wave Infrared (SWIR) imaging data produce local porosity predictions for a stainless steel part fabricated by LPBF. The SWIR camera has high sensitivity at wavelengths corresponding to peak emission of stainless steel's melting temperature making it suitable to capture porosity formation signatures. Recording the spatial and temporal components of the LPBF thermal history allows multiple features to be included for predictions of porosity. This goes beyond the information provided by single point intensities from photodiodes, or single images captured for layers post fusion. Thermal feature data (i.e., time above threshold and maximum temperature) from a cylindrical part built with various process parameters that cover the nominal fabrication space, as well as situations where lack of fusion and keyhole porosity occurs, trains the porosity probability maps. The maps predict the porosity of a complex part by only using its thermal data. The complex part contains porosity from naturally occurring thermal

history variances. A comparison with μCT ground truth scores the porosity probability models' predictions for the complex part.

2. EXPERIMENTAL SETUP

2.1. LPBF SYSTEM WITH IN-SITU SWIR CAMERA

A Renishaw AM250 LPBF system processing 304L stainless steel manufactured the cylindrical part and complex geometry part (CAD models included as Figure 1 (a)). The Renishaw AM250 employs an SPI Lasers fiber laser (P_{max} = 200 W, λ = 1070 nm) to build parts with a point-to-point exposure strategy. A staring configured FLIR SC6201 SWIR imaging camera (sensitivity: λ = 0.9–1.7 μm) recorded manufacturing layer-by-layer through a custom window. A 0.05 μm FWHM band pass filter centered at 1.45 μm (Edmund Optics #85-913) provided unsaturated SWIR data. Figure 1 (b) is a schematic of the camera observing the powder bed. The 640×512 focal plane array camera's 130 μm/pixel *x*-direction and 135 μm/pixel *y*-direction instantaneous field of view produced an 83×69 mm^2 total field of view. The camera recorded with an integration time of 5 μs at a frame rate of 2585 Hz by windowing to 80×80 pixels. A non-uniformity correction (NUC) accounted for the emission signal's cosine dependence from measurements at ~15° off normal and vignetting caused by the viewing window.

The SWIR camera provides radiation data in arbitrary units. A combination of experimental blackbody temperature data and theoretical Planck distribution exitance data calibrates the SWIR measurements. The temperature calibration permits data reporting with engineering units instead of arbitrary units and will not impact the

findings. The Renishaw's process laser heated a LPBF manufactured blackbody for the calibration experiment. Thermocouples measured the blackbody's temperature and the SWIR camera simultaneously recorded raw radiation. Integrating the Planck distribution over the camera's observation wavelengths provides theoretical blackbody exitance at a given temperature. The theoretical blackbody exitance from this integration scales with temperature to the 5.6th power. This relationship combined with the thermocouple measurements produces the theoretical exitance emitted by the blackbody during the heating experiment. The SWIR camera's raw radiation measurements linearly transforms to the theoretical blackbody exitance. The theoretical temperature-exitance relationship inverse calibrates the transformed SWIR data to temperature with units of Kelvin. This calibration assumed the emissivity of the 304L stainless steel to be 1, neglecting the temperature and phase dependence. The calibrated SWIR data is reported as the equivalent blackbody temperature, T_{BB}.

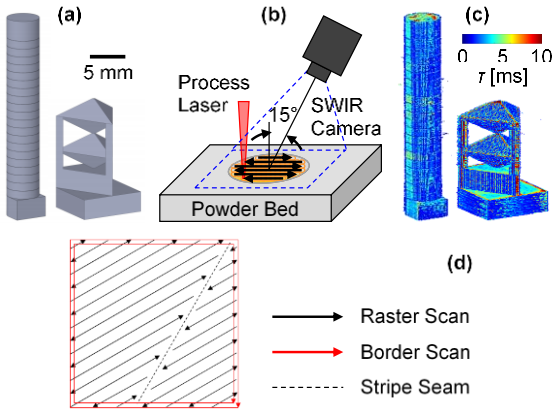

Figure 1. (a) Cylindrical sample and complex sample CAD models, (b) SWIR camera observation of the LPBF process, (c) SWIR time above 1700 K reconstructions of samples, and (d) laser scan path schematic showing raster vector stripes and border vectors.

Thermal features were extracted from the time series SWIR measurements. A thermal feature is a physics-based metric obtained from a part's local thermal history. Thermal features quantitatively describe process phenomenon indirectly seen in time series data via the reduction of the data to a single measure per pixel. This process compresses a part's data set from gigabytes to megabytes and produces 3D point clouds for decision making. A number of thermal features have been proposed in literature, including melt pool dimensions (Cheng et al., 2018), maximum temperature (Krauss et al., 2014), cooling rates (Heigel and Whitenton, 2018), and time above threshold (Mohr et al., 2020). This study uses the temporal features of the time above threshold and the maximum temperature. The selected features compare the performance of a single point measurement in maximum temperature with an integration of spatiotemporal effects in time above threshold. The time above threshold is the total time a pixel measures above a set temperature for the current layer. The threshold used during feature extraction depends on the physics of interest. At the melting temperature, the time above threshold is proportionate to the physical melt pool size, with larger melt pools corresponding to an increased value. Figure 1 (c) shows the time above 1700 K (approximate melting temperature) point clouds for the cylindrical and complex 304L stainless steel samples. The time above threshold at temperatures below the melting point informs the fusion quality since it is more dependent on the part's cooling paths. Typically, the reduction in the conduction path resulting from lack of fusion porosity causes slower cooling rates at lower temperatures in the SWIR data, leading to higher values of the time above threshold. Extraction of the time above threshold in the higher temperature regime potentially informs the area above vaporization, which gives keyholing insight. This

threshold is lower than the physical vaporization temperature due to the simultaneous interrogation of cooler temperatures with the keyhole depression region. A single pixel collects signal corresponding to vaporization temperatures and cooler temperatures as the melt pool rasters past its 130×135 μm^2 instantaneous field of view. The effective averaging of the signal over the interrogated pixel area reduces the measured temperature. The same phenomenon occurs for all measurements and is embedded in the maximum temperature thermal feature.

2.2. MICRO-COMPUTED TOMOGRAPHY

Micro-computed tomography scanning established the porosity ground truth for the samples. The µCT X-ray image slices' gray scale intensities correlate to beam attenuation. The part's porosity reduces the beam's attenuation which indicates a relative density decrease. The relative density slices combine to form a 3D point cloud for a part. The µCT data sets in this study have a voxel resolution of 15 µm/pixel in the *x*-*y* plane and 10 µm/pixel in the *z*-direction. Figure 2 outlines the procedure used to register the µCT data with SWIR imaging thermal feature reconstructions. The registration procedure requires simultaneous down-sampling of the µCT data to the SWIR data resolution by averaging and production of a binary part state map. The binary map states include porosity and fully dense (nominal). A down-sampled voxel is porosity in the binary map if more than 5% of the original resolution data within that voxel corresponds to porosity. The 5% criterion produces binary maps that flag the fine porosity features observable in the original µCT data. After manual build direction (*z*-direction) alignment, the procedure automatically registers the µCT binary state with the SWIR data in the *x*-*y* plane layer-

by-layer through translations. The registration produces thermal feature maps with voxels classified as porosity, or nominal.

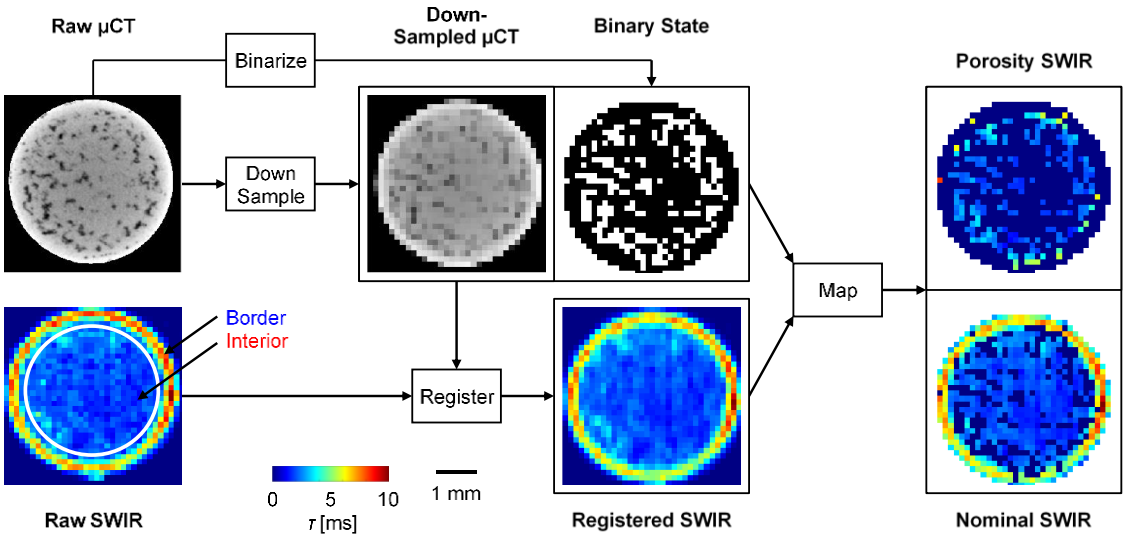

Figure 2. Registration of µCT data and time above 1700 K for voxel-by-voxel thermal feature class assignment to porosity, or nominal.

3. RESULTS AND DISCUSSION

3.1. CYLINDRICAL GEOMETRY BASELINE

The cylindrical sample's data demonstrates the SWIR imaging measurements' abilities to locally correlate with µCT porosity and to build prediction models. The cylindrical sample's diameter is 4 mm and has 20 sections, each 20 layers thick. Randomized combinations of laser power, P = 100 – 200 W (25 W increments) and exposure time, t_e = 50 – 125 µs (25 µs increments) processed the samples sections. These process parameter combinations produced lack of fusion porosity, keyholing porosity, or

nominal material. The laser point distance, d_p = 60 µm, and hatch spacing, d_h = 85 µm, were constant over the sample. Figure 3 demonstrates the local correlation of anomalies in various SWIR measurements and porosity in the µCT results for the cylindrical part's layers 306 (a), 350 (b), and 429 (c). Nominal material locations serve as a comparison baseline within those layers. The SWIR measurements include time series temperature data, melt pool images at the time of maximum temperature for the analyzed locations, time above 1700 K maps, and maximum temperature maps. The blue temperature curves, highlighted images, and pixels in Figure 3 correspond to porosity in the µCT data, while the red curves, highlighted images, and pixels correlate to nominal material.

Figure 3 (a) contains SWIR measurements corresponding to significant lack of fusion porosity. This porosity occurs when there is insufficient thermal energy and typically has irregular morphologies due to fused but not fully melted powder. The time series data indicates the porosity by the qualitatively significant temperature buildup with slower cooling when compared to the nominal data. Similarly, the blue highlighted melt pool image suggests an issue by a large area of the layer remaining above 1700 K. Nominal melt pools produce sharper temperature gradients as shown by the red highlighted image. The slow cooling at layer 306's porosity locations results in time above threshold values greater than 10 ms producing an obvious local correlation. The porosity is not reflected in layer 306's maximum temperature map. The application of border scans after the laser raster increases the time above threshold and the maximum temperature at the part's periphery. Figure 1 (d) depicts the laser raster–border scan interaction. The significant porosity in layer 306 is a result of the transition from manufacturing with a nominal laser power and a 125 µs exposure time to a 100 W laser

power and a nominal exposure time. Manufacturing with the high exposure time produced layers with a slightly concave surface for the cylindrical sample, and thus uneven powder deposition. After the process parameter change, the low laser power sufficiently fused the powder at the part's edges but failed to melt the interior. This led to agglomeration of the powder in the part's middle, which produced the slow cooling and high time above threshold. The porosity is not observable in the maximum temperature map since the laser passed over the entire cross-section and produced a similar temperature value regardless of the final fusion quality.

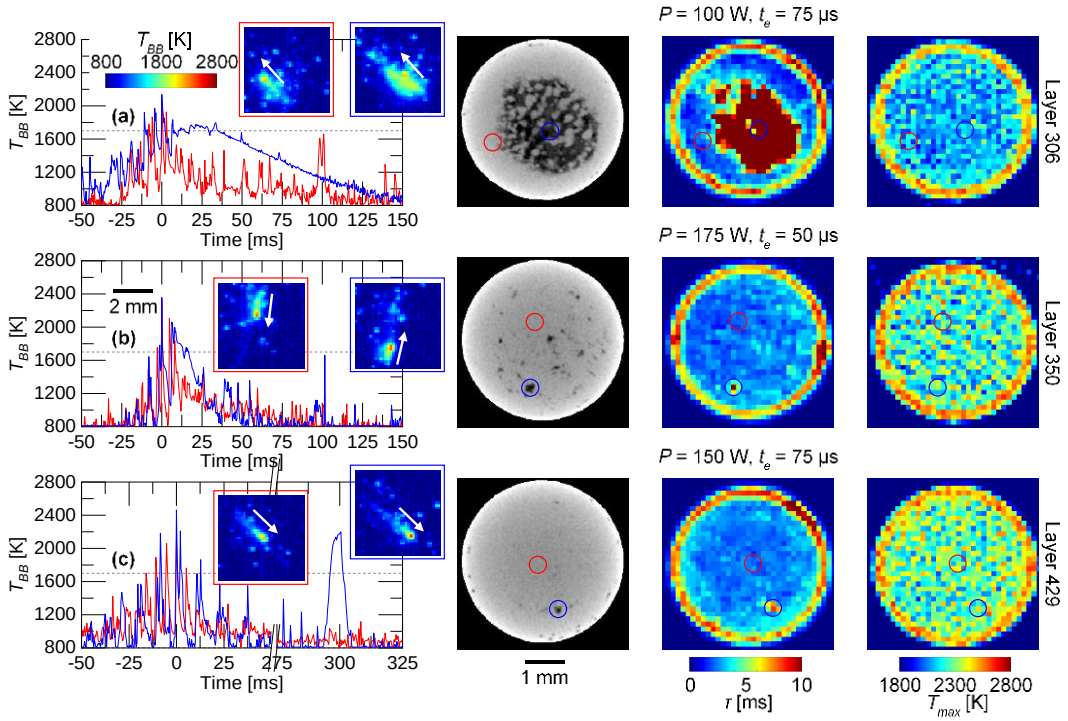

Figure 3. Comparison of time series temperature data, melt pool images, and thermal features local correlations with porosity in cylindrical sample's layers for (a,b) lack of fusion/powder agglomeration, and (c) laser spatter induced cases with nominal material baseline.

The porosity for layer 350 analyzed in Figure 3 (b) occurred during processing with P = 175 W and t_e = 50 µs. A portion of the porosity location's time series temperature data (red) demonstrates slower cooling occurred when compared to the nominal baseline (blue); however, the melt pool images are similar for the layer. The blue highlighted anomaly in the time above 1700 K map matches the pore location in the µCT slice, while there is no obvious correlation seen in the maximum temperature map. Powder agglomeration induced the lack of fusion pore in this layer. The porosity is localized and stochastic for processing with near nominal laser parameters. The lack of fusion reducing the conduction path and agglomeration resulted in the slow cooling at that location. The local nature of the porosity caused the melt pool to retain a nominal appearance. The slow cooling results in the time above threshold increase at the porosity location for layer 350, with the maximum temperature appearing similar as in layer 306.

Figure 3 (c) is thermal data that correlates to a laser spatter induced pore in layer 429. The time series data and melt pool images for this layer both indicate nominal processing except for the temperature spike in the blue curve at approximately 300 ms after the laser passes nearest to the pixel that corresponds to the pore. This led to an increase in the time above 1700 K map of that pixel, while leaving the maximum temperature map unchanged. The temperature spike in the time series data, the increase in the time above 1700 K, and the porosity are the result of a molten laser spatter landing on the part. The spatter event does not appear in the maximum temperature map since it did not exceed the value experienced during the laser raster. Layer 429 was processed with P = 150 W and t_e = 75 µs, which normally produces a nominal layer. This result

indicates that spatter induced defects may be missed by analysis based on the maximum temperature alone.

The results in Figure 3 demonstrate that thermal feature anomalies can indicate obvious, and localized porosity. Figure 3 (b) suggests that porosity formation for near nominal processing is random. This is further explored in Figure 4, where the cylindrical geometry sample's μCT data slices are compared with thermal feature results for various LPBF processing regimes. The keyholing and lack of fusion regimes are defined by the resulting porosity class (lack of fusion discussed for Figure 3) and are due to above nominal exposure time and below nominal laser power, respectively. Keyholing porosity occurs when the vaporization depressed region of the melt pool (i.e., keyhole) collapses trapping gas from vaporized material, or the build chamber atmosphere. This porosity is typically smooth and spherical and becomes more frequent for higher laser energy inputs. The nominal processing regime is defined as the laser parameter space where lack of fusion and keyholing porosity are minimized. The μCT data slice and time above 1700 K map for the cylindrical part's cross-section are plotted in Figure 4 (a) and Figure 4 (b), respectively. A qualitative comparison of the various partitions in Figure 4 (a) and Figure 4 (b) informs the global relationship between the thermal feature values and porosity amount. Significant porosity in the cylindrical sample correlates to low thermal feature values and is a result of lack of fusion from insufficient energy input. A range of thermal features correspond to minimized porosity in the sample, and then there is a porosity increase for higher thermal feature values due to keyholing from higher energy inputs.

The thermal feature–porosity correlations are analyzed locally for the three processing regimes in Figure 4 (c-e), where μCT data and time above 1700 K maps for

representative layers are plotted with time series temperature data. The nominal layer μCT data in Figure 4 (c) manufactured with P = 200 W and t_e = 75 μs shows no porosity in the interior and a small amount of porosity at the periphery. Two interior locations, indicated by circles on the μCT slice and time above 1700 K map, are selected to provide a comparison of time series temperature data. The time series temperature plot shows slight variances occurred in the layer's interior thermal history. The variances are reflected in the time above 1700 K map. The minimized porosity in the nominal layer's interior is a result of enough energy for fusion with high keyhole stability minimizing collapses. The thermal history variances observable in the time series and time above 1700 K data are within the stable range. The porosity at the nominal layer's periphery is keyholing porosity caused by the laser's increased dwell time at its turning point. This phenomenon has been observed by in-situ X-ray imaging [21].

Figure 4 (d) shows the results from a layer processed with a 200 W and a 125 μs exposure time, which resulted in keyholing porosity. The time series data is for nominal material (red), and a pore (blue) with locations highlighted on the CT and time above 1700 K map. The time series data demonstrates the difficulty in distinguishing the nominal thermal history from the keyholing pore producing thermal history. This is also the case for the time above 1700 K thermal feature map. Areas with a larger time above 1700 K do not always correspond to pore formation. The saturated location in the thermal feature map is where the laser raster ends and is caused by the heat accumulation during scanning. Even though this location experienced a much higher time above threshold, it does not correspond to an increase in porosity. The overall increase in keyholing porosity in Figure 4 (d) when compared to Figure 4 (a) is a result of manufacturing with a higher

exposure time. The higher exposure time leads to increased keyholing depth and instability, which produces more pore causing collapses. The porosity is stochastic due to the randomness of keyhole collapses. Additionally, there is the potential for pore offsetting in the *z*-direction due to the trapping of pores at the bottom of the melt pool.

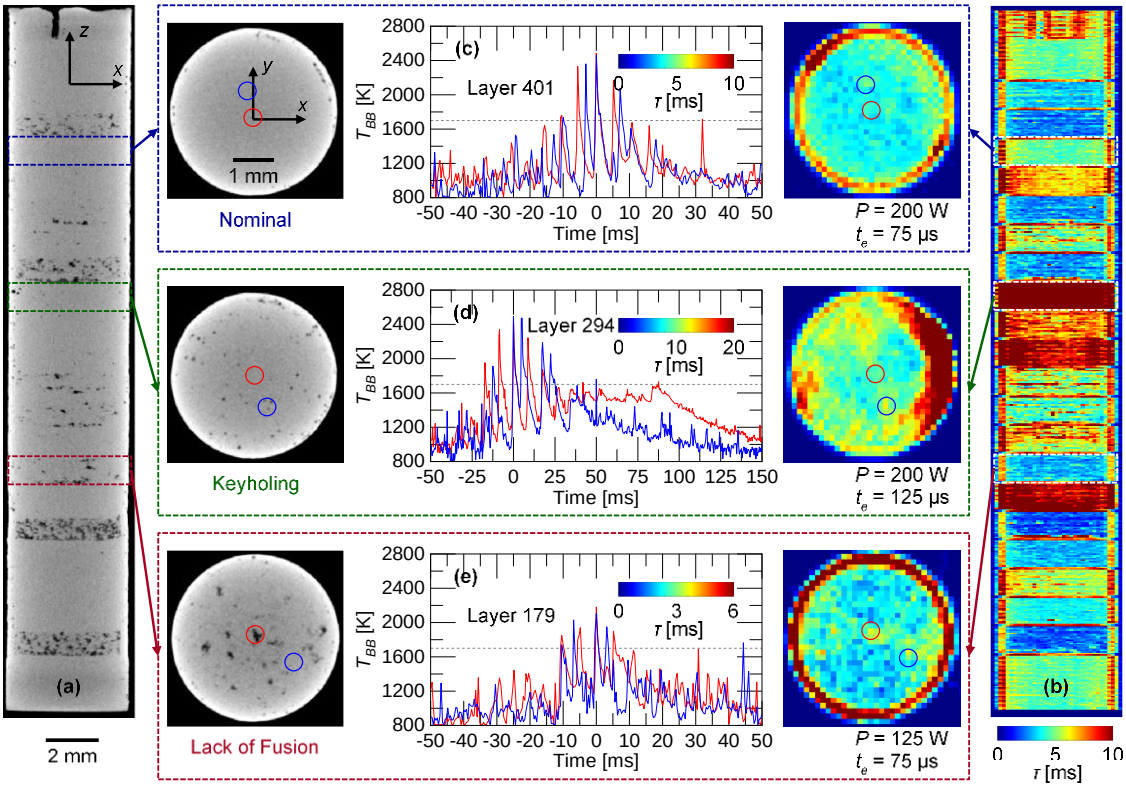

Figure 4. Cylindrical geometry sample (a) µCT and (b) time above 1700 K thermal feature slices with representative layers and time series data for (c) nominal, (d) keyholing, and (e) lack of fusion processing regimes demonstrating local correlation complexities for near nominal manufacturing.

The µCT and thermal data for a layer that experienced lack of fusion are plotted in Figure 4 (e). A laser power of 125 W and an exposure time of 75 µs processed this layer. The time series data is from locations corresponding to a pore (red), and nominal

material (blue), which are highlighted on the μCT slice and the time above 1700 K map. The time series data corresponding to the pore includes a region with slower cooling, but the overall thermal history is difficult to distinguish from the nominal. The thermal feature map has various areas of higher time above 1700 K. Some of those areas correspond to pores, while some appear nominal in the μCT data. The data slices show that the lack of fusion porosity forms randomly. The slight disturbances in the cooling rate near the porosity locations is caused by a decrease in the conduction paths as in Figure 3 (b). This leads to the increased time above 1700 K. The random nature of the lack of fusion porosity is most likely due to the powder bed packing for that layer. Some areas of the powder bed produce agglomerates or are not fully melted when exposed by the laser, while others are sufficiently fused. The effects of re-melting from subsequent layers may drive some differences between the μCT slice's porosity and time above 1700 K's anomalies.

The random porosity formation demonstrated by the results in Figure 4 (d-e) adds complexity in establishing local correlations with thermal features for prediction model development. A specific thermal feature value, or a range in values does not always correspond to porosity. This paper uses porosity probability models to address this local correlation complexity. These models empirically define the probability of porosity for a given thermal feature value. The probability model method assumes that the thermal history experienced during the layer is the most critical factor in porosity formation, and thus neglected layer-to-layer effects. The thermal features classified by the procedure in Figure 2 produce probability density functions for the data corresponding to porosity, and nominal material. These data sets combine to produce a total probability density function

for the thermal feature space. Spatial filtering separates the part's interior and border thermal features due to the differences in the dynamics of porosity formation where the laser corners during rastering. Radially, the three outermost voxels in the part's thermal feature map correspond to the border scan and laser cornering locations. The cylindrical sample's time above 1700 K and the maximum temperature probability density functions, both total (i.e., porosity and nominal) and porosity only, are plotted in Figure 5 (a) and Figure 5 (b), respectively. The dashed lines in Figure 5 (a) and Figure 5 (b) are the cylindrical part's total thermal feature probability density functions with red denoting interior data and blue border data. These functions consist of ~300,000 data points produced from 23 GB of SWIR data and 1.3 GB of µCT data. The solid lines in Figure 5 (a) and Figure 5 (b) are the porosity distributions (red: interior, blue: borders). Increases in the thermal features' means are clearly observable for the part's border. The fewer number of porosity voxels is a result of processing most of the sample with nominal, or near nominal laser parameter sets. The increase in the time above 1700 K and maximum temperature means at the border area is caused by the increased dwell time when the laser corners. An additional increase in the time above 1700 K mean is a result of the border scans re-melting the part's edges.

The data plots in Figure 5 (a) and Figure 5 (b) are the bases for porosity probability model derivation. The probability of porosity, denoted φ, given a thermal feature (e.g., time above threshold, τ) is

$$P(\varphi \mid \tau) = \frac{P(\varphi \cap \tau)}{P(\tau)} \tag{1}$$

where $P(\varphi \cap \tau)$ is the probability density function of the porosity and the time above threshold, and $P(\tau)$ is the probability density function of the time above threshold. In Figure 5 (a), $P(\varphi \cap \tau)$ is the solid red line and $P(\tau)$ is the red dashed line for the cylindrical sample's interior. The porosity probability models for a given time above 1700 K and maximum temperature are plotted in Figure 5 (c) and Figure 5 (d), respectively. The red curves are the porosity probabilities for the interiors of parts, and the blue curves are for the border areas. From low to high thermal feature values, the porosity probabilities start high, decrease to a minimum, and then increase. The slope magnitude for the decreasing region is higher than that for the increasing region. Also, the curves for the interior and borders are similar in the decreasing region of both porosity probability models.

The minimum porosity probability magnitudes are less for the interiors of parts. The porosity probabilities are higher for the borders of parts when compared to the interiors as the thermal feature values increase past the mean. There is also a higher slope in that thermal feature region for the border areas. Lack of fusion causes the high porosity probabilities for thermal feature values less than the mean. Keyholing causes the increases in porosity probability past the porosity probabilities' minimum range. Lack of fusion occurring over a narrower thermal feature range produces the higher slope magnitudes in Figure 5 (c) and Figure 5 (d) for low thermal feature values. The interior and border porosity probability curves are similar in the lack of fusion region because that porosity type equally occurs near the edges of parts, and in the middle for the laser parameter sets resulting in a significant amount. The minimum interior porosity

probabilities are less because keyholing porosity is not as frequent. The border area porosity probability is increased and more sensitive for the higher thermal feature values because the laser cornering raises the chance for keyholing.

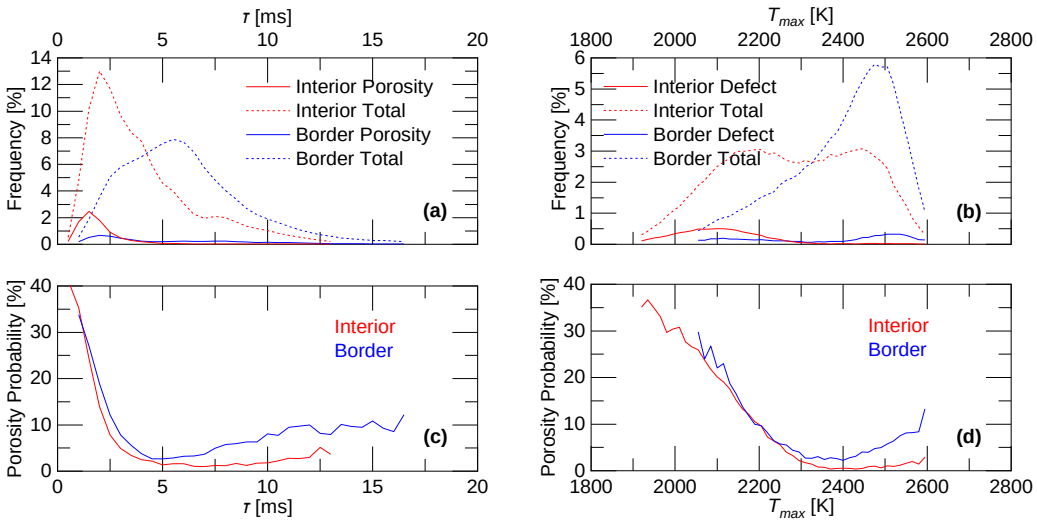

Figure 5. (a) Time above 1700 K and (b) maximum temperature probability density functions for all voxels and porosity voxels at the interior and borders of cylindrical geometry with respective porosity probabilities (c,d).

A combination of thermal features generates 2D porosity probability models. This is demonstrated for the time above 1700 K and maximum temperature in Figure 6. The porosity probability models for the interiors and borders determined in the maximum temperature and time above 1700 K space are plotted in Figure 6 (a) and Figure 6 (b), respectively. The color map value in Figure 6 is the probability of porosity for a given time above 1700 K and maximum temperature. The interior map in Figure 6 (a) contains a region of minimum porosity probability with some locally higher values and increases as maximum temperature and time above threshold both decrease. The border region map

in Figure 6 (b) has higher porosity probabilities at the extremes in the time above 1700 K and maximum temperature space.

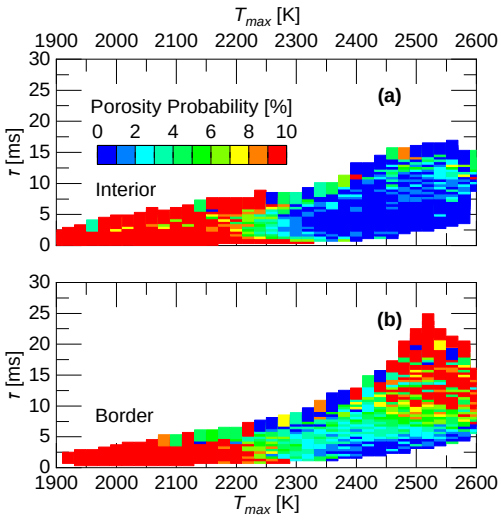

Figure 6. Porosity probability models for (a) interior and (b) border of cylindrical geometry part in time above 1700 K and maximum temperature space.

A continuous region of minimum porosity occurs for high maximum temperatures and low time above thresholds at the borders. The 2D porosity probability models provide a smaller predictable magnitude for the minimum porosity when compared to the single thermal feature models. The interior data contains a larger region of small porosity probability in the thermal feature space due to the concentration of the results for near nominal processing. The local increases within that region are from keyholing porosity. The change from a nominal processing mode to lack of fusion produces the clear transition from a low porosity probability to a high porosity probability. For the border model, the regions of increased porosity probability in the low time above threshold and

maximum temperature space are capturing lack of fusion porosity. Keyholing produces the increase in porosity probability for the high time above 1700 K and maximum temperature for that model. The area of minimum porosity probability for high maximum temperature and low time above 1700 K for the border is a result of the inner most voxel moving towards interior manufacturing behavior. The 2D porosity probability models provide a smaller predictable magnitude due to an increased ability to distinguish nominal manufacturing from the other processing regimes.

3.2. COMPLEX GEOMETRY PREDICTION

Porosity predictions for the complex geometry sample establish the performance of the porosity probability model framework. The complex sample's rectangular cross-section is 7×8 mm^2, the equilateral triangular cross-section has 8 mm side lengths, and the triangular pyramids consists of 8 mm base side lengths with 45° face angles. A single nominal laser parameter set (P = 200 W, t_e = 75 μs) and scan path striping manufactured the complex sample. Scan path striping, illustrated in Figure 1 (d), is the division of a layer's cross-sectional area into shorter sets of laser raster vectors. As a result, the laser corners in the part's interior and seams occurs where the stripes overlap. The striping orientation and seam positions change from layer-to-layer producing laser raster vector length and cornering dwell location differences. This combined with the complex part's geometry dependent heat transfer boundary conditions (supported, or overhang) induced the natural thermal history variations. The complex sample's time above 1700 K and maximum temperature data produced the 2D probability density function set plotted in Figure 7. The 2D probability density function set shows that most of the complex

sample's data lies within the thermal feature space used to train the defect probability models in Figure 5 and Figure 6. There are some voxels in the border data that have time above thresholds outside of the training space. The interior data in Figure 7 (a) is clustered in the region corresponding to minimum porosity probability in Figure 6 (a) since it was manufactured with a nominal parameter set. The border data outside of the bounds of the training model is due to the complex part's overhang boundary condition. This is demonstrated by a cross-section view in Figure 7 (c) where the overhang portions experience higher time above 1700 K due to slower cooling.

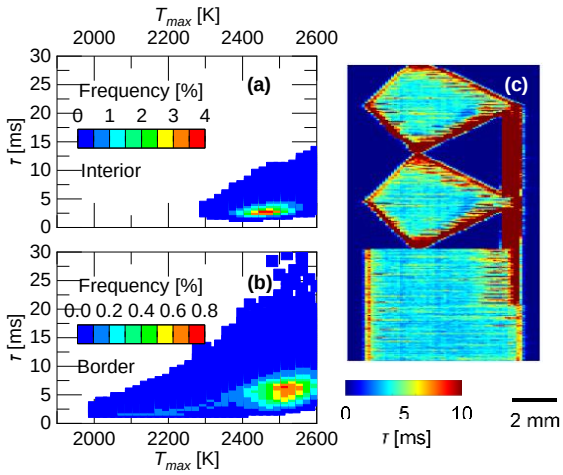

Figure 7. (a) Interior and (b) border area time above 1700 K and maximum temperature 2D probability density functions for entire volume of complex sample with (c) time above 1700 K reconstruction cross-section.

While not all plotted in this paper, the procedures discussed for Figure 5 and Figure 6 produced additional single feature models and 2D models (maximum temperature and time above threshold) based on the cylindrical geometry's time above threshold extracted at various temperatures. The models' temperature thresholds range

from 1100 K (low temperature) to 2100 K (high temperature), which includes temperatures for the lack of fusion oriented time above threshold and the keyholing sensitive time above threshold. Time above threshold at temperatures over 2100 K produces insufficient data sets for porosity probability modeling. The time above threshold, maximum temperature, and 2D porosity probability models convert the complex sample's respective thermal feature measurements to make local predictions. Both the interior and border models predict the complex sample's porosity, where the border model only applies to the three outermost pixels within the part's layers. The prediction framework saturates pixels with measurements that fall outside of the models' thermal feature space. Figure 8 contains example prediction results for the complex sample obtained by using the combined maximum temperature and time above 1700 K porosity probability model in Figure 6. The complex sample's μCT cross-section is the center plot in Figure 8. Color coding highlights the locations of selected layers from the various geometry sections. The layer data includes μCT slices and the corresponding porosity probability model predictions. The μCT data shows the sample's porosity is small and primarily occurred at its borders. Additionally, the μCT data reveals geometry deviations at the sample's overhangs. The model from Figure 6 (a) generally predicts low porosity probabilities for the part's interior regardless of cross-sectional geometry and overhang case. The probability predictions for the borders of the rectangular cross-section, triangular cross-section, and supported pyramids are higher than the interior. The probability prediction magnitudes are much higher for the border areas of the overhang pyramids. The pore size and locations in Figure 8's μCT data are characteristics of the keyholing porosity that occurs during nominal processing discussed for Figure 4 (c).

Overheating producing agglomeration at the overhangs causes the geometry deviations. Porosity probability model training did not account for that defect type. The low predictions for the complex part's rectangular cross-section, triangular cross-section, and supported pyramid interiors match the expectations for the processing mode. The border area porosity probability increase for those sections also tracks the observations and discussion for nominal processing. An interesting result for the overhang geometries is the sharp transition predicted for the defect probability at the sections' interiors. The probability model predicts a very small chance for porosity at locations in the overhang geometries fused with enough conduction paths. The µCT slices confirm these predictions. This result shows that sufficient conduction paths occur within a short distance from the overhang.

An operating point transforms a model's porosity probability predictions to binary for voxel-by-voxel scoring with the ground truth from µCT. Predictions falling below the operating point are nominal, and predictions above are porosity. For example, if the operating point is a porosity probability of 5%, then predictions above that value are defined as porosity, and the remaining are assumed nominal. Comparing the converted prediction data with the binary µCT ground truth provides the true positives (i.e., prediction and truth are both porosity), false positives (i.e., prediction is porosity, but truth is no porosity), true negatives (i.e., prediction and truth are both no porosity), and false negatives (i.e., prediction is no porosity, but truth is porosity). Calculations based on those metrics yield the true positive and false positive rates. The true positive rate, *TPR*, is the total number of true positives divided by the sum of the true positives and false negatives. The false positive rate, *FPR*, is the total number of false positives divided by

the sum of false positives and true negatives. Sweeping the operating point over a range and calculating the respective prediction rates generates a Receiver Operating Characteristic (ROC) curve for a porosity probability model. The ROC curve is a plot of the true positive rate against the false positive rate. Figure 9 demonstrates the ROC development process for the maximum temperature only model's porosity prediction results over an operating range from 0 to 40%. This porosity probability model's predictions are the baseline for comparisons of the various time above threshold, and the 2D models' results. The true positive rate (blue) and false positive rate (red) are plotted as a function of the operating point in Figure 9 (a). The inset of the maximum temperature model's predictions for the complex geometry in Figure 9 (b) qualitatively informs where the porosity occurred for a given operating point. Both the true and false rates start at 1 and then follow different curves as they decrease to 0 at higher operating points. For very low operating points, every voxel in the predictions will be assigned as porosity. This produces the high true and false positive rates. The rates fall with increasing the operating point because less data is flagged as defective. The spread between the true positive rate and false positive rate corresponds to the performance of the prediction model. This is easily observable through the ROC plot in Figure 9 (b). The ROC curve describes the performance of the porosity probability model, with more accurate predictions producing curves shifted up and to the left. A perfect detector will produce a ROC curve that only contains true positive rates of 1 and false positive rates of 0, regardless of operating point. Real detectors/frameworks produce a ROC with an inflection point, where the difference between the true positive rate and false positive rate is maximized. This point for the maximum temperature porosity probability model corresponds to a true positive rate of

0.89, and a false positive rate of 0.32. A common way to quantify the overall performance of the porosity probability model is the area under the ROC curve (*AUC*). The *AUC* for the maximum temperature porosity model is 0.82.

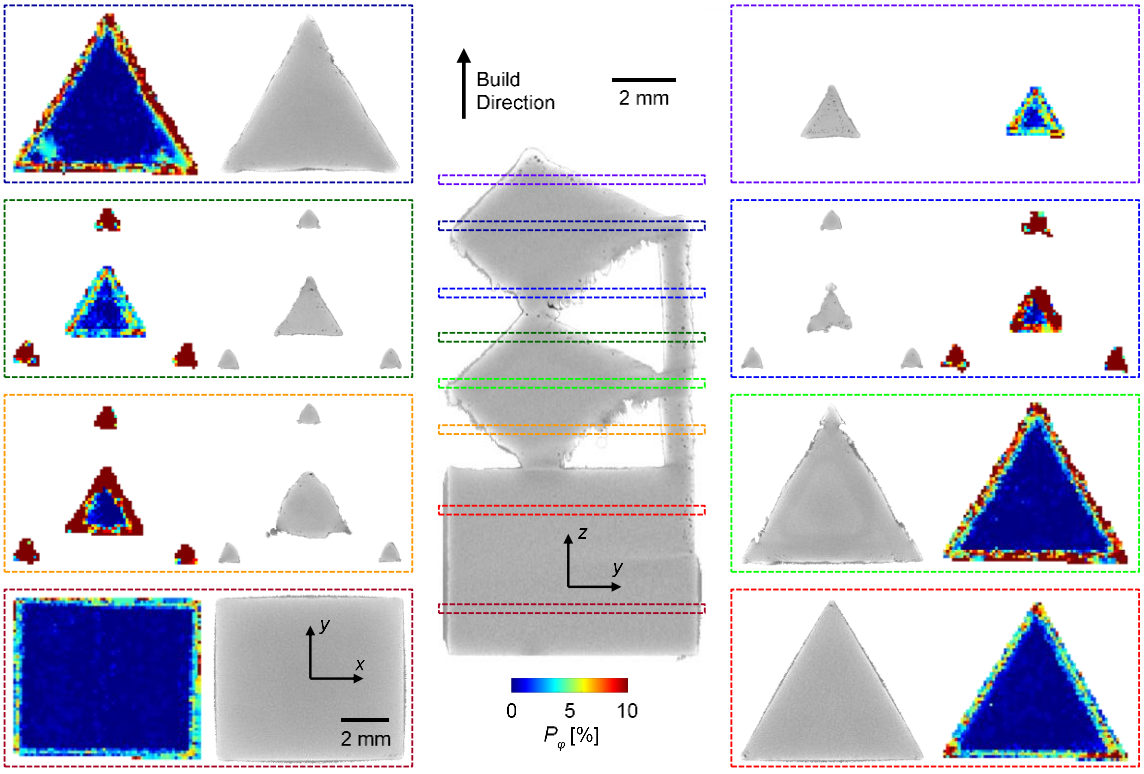

Figure 8. Complex sample µCT data slices with corresponding porosity probability predictions using 2D time above 1700 K and maximum temperature model for layers selected from various geometries.

The ROC curve for the maximum temperature model in Figure 9 shows that the false positive rates become large for true positive rates greater than 0.9. This is a result of uncertainties inherent to the SWIR imaging process, and registration with the µCT data. The instantaneous field of view for the SWIR camera is larger than most keyholing

porosity. The camera measurements can flag where this porosity is likely to occur, but the pixel size combined with the random nature of the porosity formation produces error. The registration between the SWIR thermal features and µCT data contains errors due to thermally driven part deformation that occurs during manufacturing. An example of this is observable in Figure 8 for the structures supporting the complex geometry's pyramids. Additionally, the final locations of some keyholing porosity formed during manufacturing may occur below the correctly registered data slices. This keyhole offsetting leads to increase in false positives. These reasons for error will be common to all porosity probability models used for prediction which means a contrast of their performance is still possible.

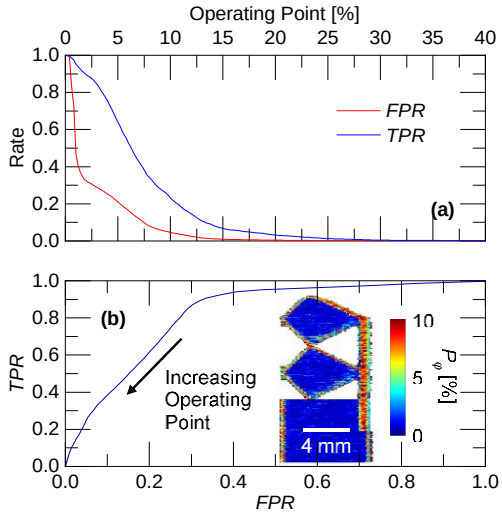

Figure 9. (a) Complex geometry porosity probability prediction false positive and true positive rates at various operating points for maximum temperature model with (b) corresponding ROC curve and inset of prediction for sample's cross-section.

Figure 10 compares the performance of the various porosity probability models. The ROC curves for the time above threshold only models' predictions are plotted in Figure 10 (a) with a shared legend in Figure 10 (b). The ROC curves in Figure 10 (a) show that prediction performance increases for higher thresholds. The 1100 K and 1300 K models are the worst performing with the false positive exceeding the true positive rate for all operating points since the curves fall below the line with a slope of unity. The predictions based on the threshold of 1300 K and below fail due to the lack of contrast in the thermal feature data corresponding to porosity and nominal material. This is a result of the low thresholds producing very high time above threshold values where noise from laser spatter is significant.

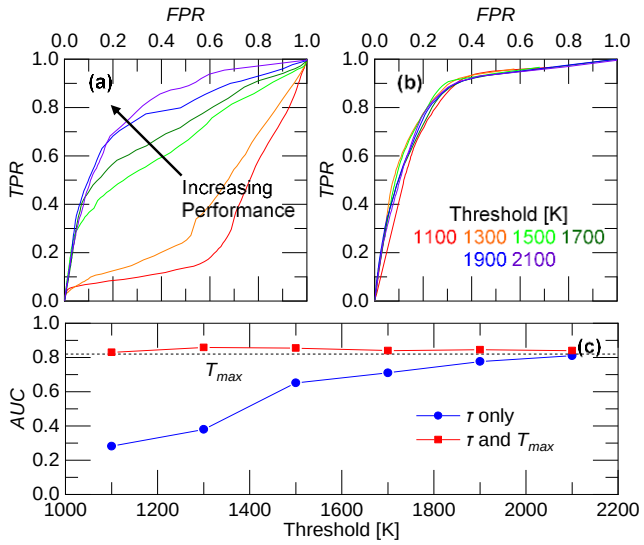

Figure 10. ROC curves for (a) time above threshold only and (b) 2D porosity probability models with (c) a comparison of the AUC's for the various models.

The increase in prediction performance for the time above threshold models in Figure 10 (a) is explained by observations from their respective porosity probability models. The interior and border porosity probability models for the time above threshold at 1500-2100 K are plotted in Figure 11 (a) and Figure 11 (b), respectively. These models demonstrate similar characteristic as those discussed for Figure 5. The porosity probability starts at a high level, decreases to a minimum, and then rises with increasing time above threshold. This behavior with increasing time above threshold respectively corresponds to the progression through the lack of fusion, nominal, and keyholing processing regimes. Figure 11 shows that the sensitivity of the models for thermal feature values away from the nominal region increases for the higher temperature threshold features. This is especially the case for keyholing porosity in the border area models plotted in Figure 11 (b). The sensitivity increase is a result of a narrowing in the thermal feature probability density functions informing the porosity models. The reduction in the thermal history space leads to an increase in porosity frequency at the bounds since it has fewer time above threshold values for correspondence. The increased frequencies drive the higher sensitivity in the porosity probability as the thermal feature value moves away from the nominal location. The nominal location in the porosity probability models retain a low magnitude. Therefore, the time above threshold probability models perform better in Figure 10 (a) for the complex sample as the temperature extraction threshold increases. The models trained with the time above threshold at higher temperatures have more ability to distinguish thermal histories that result in porosity and nominal material.

The ROC curves for the predictions made by the 2D porosity probability models in time above threshold and maximum temperature space are plotted in Figure 10 (b).

The combined models provide predictions with similar ROC curves regardless of the temperature threshold. This occurs because the 2D thermal feature space produces clear regions in the porosity probability models that correspond to the lack of fusion, nominal, and keyholing processing regimes. The definitions of the processing regions in the 2D models are more defined than for a single thermal feature. This permits a more accurate determination of porosity probability, which explains the drastic performance increase for the models using the time above threshold extracted at lower temperatures. The *AUC* was calculated for the ROC curves in Figure 10 (a) and Figure 10 (b). The results are benchmarked against the maximum temperature porosity probability model's *AUC* in Figure 10 (c). The *AUC* for the time above threshold only porosity probability models are plotted in blue, and the *AUC* for the 2D probability models are plotted in red. The data is plotted as a function of the time above threshold extraction temperature. The maximum temperature model's *AUC* is the dashed line. The time above threshold only models' predictions approaches the maximum temperature result with increasing threshold until 2300 K. The combined features slightly outperform the maximum temperature only predictions for the models based on time above threshold at 1100 K through 2100 K. As discussed for Figure 10 (a), the increasing temperature threshold for time above threshold extraction produces porosity probability models with increased sensitivity. As the threshold increases, the results converge to the information provided by the maximum temperature producing the similar *AUC*. The 2D porosity probability models leverage the information provided by both the maximum temperature and time above threshold to inform the porosity probability more accurately, which yields the performance increase.

The matched performance by the time above 1900 K model and the slightly better performances for the 2D models suggest that the maximum temperature only model may be enough to locally predict porosity. This must be viewed in the context of the results in Figure 3 and Figure 8. In Figure 3, the maximum temperature does not identify porosity, while clear local correlations are observable for the time above 1700 K. This of course is not the case for every porosity location in the part due to the complexities discussed in Figure 4, and overall, the maximum temperature provides strong contrast for the thermal histories resulting in porosity and nominal material. The time above threshold adds to the maximum temperature's baseline, which permits the ability to detect porosity more accurately.

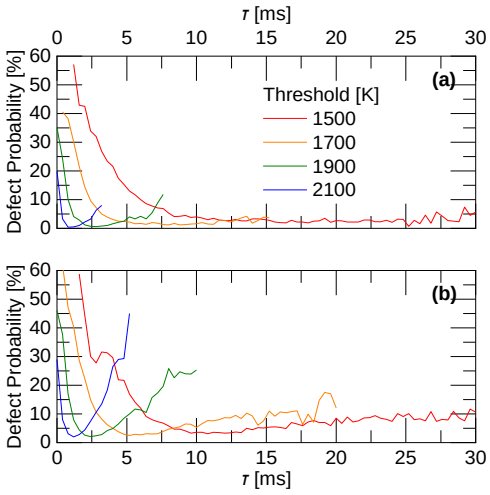

Figure 11. Time above threshold porosity probability models from the cylindrical geometry sample for (a) interior and (b) border regions.

Prediction of the geometry variations discussed for Figure 8 is not included, but they are considered defects. Anomalies in the time above threshold strongly correlate to

the locations where the geometry variations occur, especially when it is extracted at lower temperatures. This further explains the relative decrease in performance for those porosity probability models. The higher time above threshold models are more sensitive to porosity than the geometry variations, which is why they produced prediction results like the maximum temperature. The maximum temperature's lower sensitivity to the overhang effects increases its porosity prediction performance. The strength of the time above threshold to identify geometry variations is beyond the scope of this work but should be explored. With further training, the information the 2D thermal feature space models provide may permit a wider range of predictable defects than single feature models.

Analyzing the complex part on a section-by-section basis produces marginal ROC improvements. The part's three section types are nominal (i.e., the rectangular and triangular), overhang pyramid, and supported pyramid. This analysis uses the maximum temperature model and the time above 1500 K combined models since they perform best for the entire sample. Figure 12 contains the sectioned ROC curves using those models with the part's sections highlighted on the maximum temperature prediction slice inset in Figure 12 (a). The curves in Figure 12 (a) and Figure 12 (b) demonstrate that both models perform better for the nominal and supported pyramid data than for the overhang pyramid data. The models' performances increase for the rectangular and triangular cross-sections because those geometries were manufactured with heat transfer boundary conditions most like the training data. The combined feature model performs better for the supported pyramid when compared to the overhang because the layers had enough conduction paths for time above threshold to contribute effectively. The maximum temperature and

combined models perform worse at the overhangs due to the absence of training data for that boundary condition. The *AUC* for these results are listed in Table 1. The *AUC* clearly shows the 2D feature space model provides more accurate predictions than the maximum temperature for the nominal and supported sections, which is due to the increased ability to recognize the processing regime. The results also demonstrate that the overhang data likely reduces the performance for all models analyzed in this study, which solidifies the need to train for that boundary condition in the future. Moreover, further classification and training porosity probability models by geometry type, like bulk and thin wall structures with interior and border subregions, would make this approach applicable to any geometry.

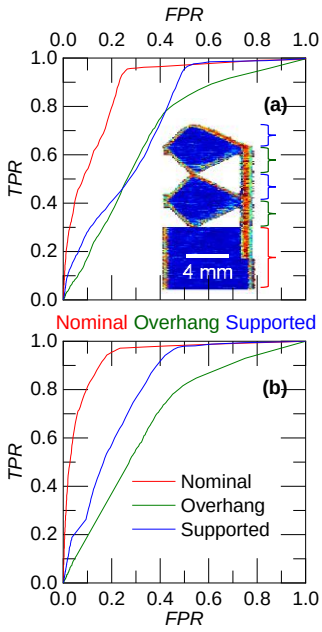

Figure 12. ROC curves from (a) maximum temperature and (b) 2D maximum temperature and time above 1500 K porosity probability models for various sections of complex sample.

Table 1. *AUC* for maximum temperature and 2D maximum temperature and time above 1500 K porosity probability models based on each section of complex sample.

Section	T_{max} *AUC*	τ_{1500} and T_{max} *AUC*
Nominal	0.88	0.94
Overhang	0.69	0.69
Supported	0.74	0.81

4. SUMMARY AND CONCLUSIONS

In this paper, porosity probability models informed by SWIR imaging thermal features locally predicted porosity for a LPBF manufactured 304L stainless steel sample. The porosity probability model approach addressed the difficulties that arise in developing local correlations between SWIR thermal features and porosity in µCT data. Thermal feature data from a cylindrical part manufactured with various parameters trained the porosity probability models which spanned lack of fusion, keyholing, and nominal processing. The models converted SWIR measurements from a nominally manufactured complex geometry sample to porosity probability, and Receiver Operating Characteristic curves scored the predictions. Approximately 1% of the complex geometry sample's volume corresponded to porosity, and the framework predicted those at an 88% true positive rate, with a 27% false positive rate using the best performing model. This result is promising, but it reveals the challenges of high false positive rates in the local porosity predictions. The local porosity probability predictions must be completed with recognition that this will occur during operation due to the random nature of pore

formation, the size of the pores relative to the thermal camera's instantaneous field of view, and some impact from data indexing errors.

The results in this paper demonstrated that porosity predictions made by 2D thermal feature models had the best performance due to an increase in the ability to locally distinguish the processing regime. The porosity prediction rate improved when only considering the complex sample's non-overhang geometries. The combined maximum temperature and time above 1500 K porosity probability model reduced the false positive rate by an average of 8% in those sections when compared to the maximum temperature only predictions. Future work should improve the porosity probability models by considering the keyhole offsetting in data registration, which may reduce the false positives in predictions. While beyond the scope of this work, the baseline for predictions must be expanded to include overhang and thin wall structures to better account for porosity and geometry deviations. This training may require algorithms with increased complexity such as machine learning but will produce multi-thermal feature-based models that predict additional defect types beyond porosity.

ACKNOWLEDGEMENT

This work was funded by Honeywell Federal Manufacturing & Technologies under Contract No. DE-NA0002839 with the U.S. Department of Energy. The United States Government retains and the publisher, by accepting the article for publication, acknowledges that the United States Government retains a nonexclusive, paid up,

irrevocable, world-wide license to publish or reproduce the published form of this manuscript, or allow others to do so, for the United States Government purposes.

REFERENCES

[1] H. Gong, K. Rafi, H. Gu, T. Starr, B. Stucker, Analysis of defect generation in Ti-6Al-4V parts made using powder bed fusion additive manufacturing processes, Addit. Manuf. 1 (2014) 87–98. https://doi.org/10.1016/j.addma.2014.08.002.

[2] W.E. King, H.D. Barth, V.M. Castillo, G.F. Gallegos, J.W. Gibbs, D.E. Hahn, C. Kamath, A.M. Rubenchik, Observation of keyhole-mode laser melting in laser powder-bed fusion additive manufacturing, J. Mater. Process. Technol. 214 (2014) 2915–2925. https://doi.org/10.1016/j.jmatprotec.2014.06.005.

[3] W. Wang, J. Ning, S.Y. Liang, Prediction of lack-of-fusion porosity in laser powder-bed fusion considering boundary conditions and sensitivity to laser power absorption, Int. J. Adv. Manuf. Technol. (2020). https://doi.org/10.1007/s00170-020-06224-7.

[4] S.M.H. Hojjatzadeh, N.D. Parab, Q. Guo, M. Qu, L. Xiong, C. Zhao, L.I. Escano, K. Fezzaa, W. Everhart, T. Sun, L. Chen, Direct observation of pore formation mechanisms during LPBF additive manufacturing process and high energy density laser welding, Int. J. Mach. Tools Manuf. 153 (2020) 103555. https://doi.org/10.1016/j.ijmachtools.2020.103555.

[5] T. Craeghs, S. Clijsters, J.P. Kruth, F. Bechmann, M.C. Ebert, Detection of Process Failures in Layerwise Laser Melting with Optical Process Monitoring, Phys. Procedia. 39 (2012) 753–759. https://doi.org/10.1016/j.phpro.2012.10.097.

[6] H. Krauss, T. Zeugner, M.F. Zaeh, Layerwise monitoring of the Selective Laser Melting process by thermography, Phys. Procedia. 56 (2014) 64–71. https://doi.org/10.1016/j.phpro.2014.08.097.

[7] J. Mireles, S. Ridwan, P.A. Morton, A. Hinojos, R.B. Wicker, Analysis and correction of defects within parts fabricated using powder bed fusion technology, Surf. Topogr. Metrol. Prop. 3 (2015). https://doi.org/10.1088/2051-672X/3/3/034002.

[8] J.L. Bartlett, F.M. Heim, Y. V. Murty, X. Li, In situ defect detection in selective laser melting via full-field infrared thermography, Addit. Manuf. 24 (2018) 595–605. https://doi.org/10.1016/j.addma.2018.10.045.

[9] S. Yoder, P. Nandwana, V. Paquit, M. Kirka, A. Scopel, R.R. Dehoff, S.S. Babu, Approach to qualification using E-PBF in-situ process monitoring in Ti-6Al-4V, Addit. Manuf. 28 (2019) 98–106. https://doi.org/10.1016/j.addma.2019.03.021.

[10] J.A. Mitchell, T.A. Ivanoff, D. Dagel, J.D. Madison, B. Jared, Linking pyrometry to porosity in additively manufactured metals, Addit. Manuf. 31 (2020). https://doi.org/10.1016/j.addma.2019.100946.

[11] G. Mohr, S.J. Altenburg, A. Ulbricht, P. Heinrich, D. Baum, C. Maierhofer, K. Hilgenberg, In-situ defect detection in laser powder bed fusion by using thermography and optical tomography—comparison to computed tomography, Metals (Basel). 10 (2020). https://doi.org/10.3390/met10010103.

[12] S. Coeck, M. Bisht, J. Plas, F. Verbist, Prediction of lack of fusion porosity in selective laser melting based on melt pool monitoring data, Addit. Manuf. 25 (2019) 347–356. https://doi.org/10.1016/j.addma.2018.11.015.

[13] M. Khanzadeh, S. Chowdhury, M. Marufuzzaman, M.A. Tschopp, L. Bian, Porosity prediction: Supervised-learning of thermal history for direct laser deposition, J. Manuf. Syst. 47 (2018) 69–82. https://doi.org/10.1016/j.jmsy.2018.04.001.

[14] O. Kwon, H.G. Kim, M.J. Ham, W. Kim, G.H. Kim, J.H. Cho, N. Il Kim, K. Kim, A deep neural network for classification of melt-pool images in metal additive manufacturing, J. Intell. Manuf. (2018). https://doi.org/10.1007/s10845-018-1451-6.

[15] L. Scime, J. Beuth, Using machine learning to identify in-situ melt pool signatures indicative of flaw formation in a laser powder bed fusion additive manufacturing process, Addit. Manuf. 25 (2019) 151–165. https://doi.org/10.1016/j.addma.2018.11.010.

[16] H. Baumgartl, J. Tomas, R. Buettner, M. Merkel, A deep learning-based model for defect detection in laser-powder bed fusion using in-situ thermographic monitoring, Prog. Addit. Manuf. 5 (2020) 277–285. https://doi.org/10.1007/s40964-019-00108-3.

[17] A. Gaikwad, B. Giera, G.M. Guss, J.B. Forien, M.J. Matthews, P. Rao, Heterogeneous sensing and scientific machine learning for quality assurance in laser powder bed fusion – A single-track study, Addit. Manuf. (2020) 101659. https://doi.org/10.1016/j.addma.2020.101659.

[18] J.B. Forien, N.P. Calta, P.J. DePond, G.M. Guss, T.T. Roehling, M.J. Matthews, Detecting keyhole pore defects and monitoring process signatures during laser powder bed fusion: A correlation between in situ pyrometry and ex situ X-ray radiography, Addit. Manuf. 35 (2020) 101336. https://doi.org/10.1016/j.addma.2020.101336.

[19] B. Cheng, J. Lydon, K. Cooper, V. Cole, P. Northrop, K. Chou, Infrared thermal imaging for melt pool analysis in SLM: a feasibility investigation, Virtual Phys. Prototyp. 13 (2018) 8–13. https://doi.org/10.1080/17452759.2017.1392685.

[20] J.C. Heigel, E. Whitenton, Measurement of thermal processing variability in powder bed fusion, Proc. - 2018 ASPE Euspen Summer Top. Meet. Adv. Precis. Addit. Manuf. 69 (2018) 242–247.

[21] A.A. Martin, N.P. Calta, S.A. Khairallah, J. Wang, P.J. Depond, A.Y. Fong, V. Thampy, G.M. Guss, A.M. Kiss, K.H. Stone, C.J. Tassone, J. Nelson Weker, M.F. Toney, T. van Buuren, M.J. Matthews, Dynamics of pore formation during laser powder bed fusion additive manufacturing, Nat. Commun. 10 (2019) 1–10. https://doi.org/10.1038/s41467-019-10009-2.

IV. RAPID THERMAL HISTORY PREDICTION FOR LASER POWDER BED FUSION BY EXPERIMENTALLY INFORMED SUPERPOSITION MODEL

Cody S. Lough[1], Robert G. Landers[1], Douglas A. Bristow[1], James A. Drallmeier[1], Edward C. Kinzel[2]

[1]Department of Mechanical and Aerospace Engineering, Missouri University of Science and Technology, Rolla, MO 65409

[2]Department of Aerospace and Mechanical Engineering, University of Notre Dame, Notre Dame, IN 46556

ABSTRACT

This paper evaluates experiment-based superposition thermal modeling for Laser Powder Bed Fusion (LPBF) with a pulsed laser. An analytical pulsed laser thermal model establishes the modeling procedure. The framework inverts an experimental powder bed's single pulse temperature response from spatiotemporal Short-Wave Infrared (SWIR) camera data. Superimposing this response along a scan path simulates multi-pulse LPBF. Results show the experimentally informed superposition model rapidly and accurately predicts a layer's temperature history. The model has applications in correction of thermally driven LPBF errors and in-situ part qualification.

1. INTRODUCTION

Laser Powder Bed Fusion (LPBF) fabricates high resolution, complex, metal parts layer-by-layer. Part geometry variances and changing laser scan pathing drive thermal

differences within layers that produce defects [1]. Analytical [2], numerical [3], and high fidelity [4] thermal models aim to understand LPBF's underlying physics causing those variations with significant computational expense. Controls-oriented superposition thermal models quickly predict a layer's temperature history. The superposition approach's linear assumptions reduce a layer's computation time from days, or weeks, to minutes, making it feasible for application in real-time process correction.

Moran et al. combined Rosenthal's moving point heat source solution with FEA to perform superposition simulations of a laser scanning Ti-6Al-4V [5]. Moran et al. found their model provides results accurate to FEA only simulations with a significant decrease in computation time. The computation time reduction makes large scale simulations practical. Schwalbach et al. used Green's function methodology to develop a thermal model for LPBF with a continuous wave (CW) laser [6]. Schwalbach et al.'s model approximates a scanning CW laser by superimposing the temperature response from distinct heat sources seeded along the raster path. Schwalbach et al. demonstrated their model's temperature results agree with analytical solutions, calibration provides accurate melt pool dimension predictions, and the approach indicates thermal history spatial variations.

Temperature and state dependent thermal properties, latent heat effects from melting and solidification, and material vaporization make the LPBF process highly non-linear. This limits analytical superposition models to qualitatively predicting part geometry-scan path interaction effects. A superposition model informed by thermal camera data would provide quantitative predictions with LPBF's physics embedded, but this requires the experimental measurements to behave linearly. The quantitative analysis

may improve decision making capability, and baseline in-situ measurements to assist part qualification.

This paper presents an LPBF superposition thermal model constructed with Short-Wave Infrared (SWIR) thermal camera measurements. A theoretical superposition model's derivation for pulsed laser LPBF reveals the methodology for experiment-based modeling. The superposition modeling process gauges the SWIR camera measurement's linearity. Processing simulation and experimental data with an in-situ framework evaluates the superposition model's ability to predict real thermal history variances.

2. MOTIVATING THEORY

The theoretical pulsed laser superposition model's derivation follows Schwalbach et al.'s work for CW systems [6]. The pulsed laser's volumetric heat source model, $\dot{q}(x,y,z,t)$, is [7]

$$\dot{q}(x,y,z,t)=\frac{2(1-R)P}{\delta_p \pi \omega^2}\exp\left(-2\frac{x^2+y^2}{\omega^2}\right)\exp\left(-\frac{|z|}{\delta_p}\right)\left[1-\Theta(t-t_e)\right], \tag{1}$$

where (x,y,z) are the spatial coordinates, t is the time, R is the reflectance, P is the laser power, δ_p is the laser's optical penetration depth, ω is the beam waist, Θ is the Heaviside function, and t_e is the exposure time. The temperature field, $T(x,y,z,t)$, a single laser pulse produces in a semi-infinite domain is

$$T(x,y,z,t) = T_0 + \frac{2(1-R)P}{\delta_p \pi \rho c_p} \int_0^t \frac{\left[1-\Theta(t_0-t_e)\right]\Theta(t-t_0)}{8\alpha(t-t_0)+\omega^2} \exp\left(\frac{-2(x^2+y^2)}{8\alpha(t-t_0)+\omega^2}\right) \cdot \frac{1}{2}\left(\begin{array}{l} \exp\left(\frac{\alpha(t-t_0)-\delta_p z}{\delta_p^2}\right)\operatorname{erfc}\left(\frac{2\alpha(t-t_0)-\delta_p z}{\sqrt{4\alpha(t-t_0)}\delta_p}\right) \\ +\exp\left(\frac{\alpha(t-t_0)+\delta_p z}{\delta_p^2}\right)\operatorname{erfc}\left(\frac{2\alpha(t-t_0)+\delta_p z}{\sqrt{4\alpha(t-t_0)}\delta_p}\right) \end{array}\right) dt_0 , \quad (2)$$

where T_0 is the initial temperature and α is the thermal diffusivity. The relative temperature change, $T(x,y,z,t)-T_0$, is the laser pulse's basis function. The *x*-*y* plane radially symmetric basis function, $G(r,t)$, at $z = 0$ is

$$G(r,t) = \frac{2(1-R)P}{\delta_p \pi \rho c_p} \int_0^t \frac{\left[1-\Theta(t_0-t_e)\right]\Theta(t-t_0)}{8\alpha(t-t_0)+\omega^2} \exp\left(\frac{-2r^2}{8\alpha(t-t_0)+\omega^2}\right) \cdot \exp\left(\frac{\alpha(t-t_0)}{\delta_p^2}\right)\operatorname{erfc}\left(\frac{\sqrt{\alpha(t-t_0)}}{\delta_p}\right) dt_0 , \quad (3)$$

where $r = \sqrt{x^2+y^2}$.

Superimposing single pulse basis function copies shifted in space and time simulates multiple laser pulses. The basis function copies offset spatially according to the laser scan path and temporally by the pulse period. The temperature for a multi-pulse simulation at $z = 0$ is

$$T(x,y,t) = T_0 + \sum_{k=1}^{K} G_k(r,t'), \quad (4)$$

where G_k is the k^{th} laser pulse's basis function. The k^{th} pulse's radius, r, to a given (x,y) and its relative time, t', are

$$\begin{cases} r = \sqrt{\left(x - x_{0,k}\right)^2 + \left(y - y_{0,k}\right)^2} \\ t' = t - t_{0,k} \end{cases}, \tag{5}$$

where $\left(x_{0,k}, y_{0,k}\right)$ are its exposure coordinates and $t_{0,k}$ is when exposure begins.

Figure 1 demonstrates superposition for six laser pulses (P = 200 W, t_e = 70 µs, ω = 70 µm, δ_p = 60 µm) striking 304L stainless steel (k = 15 W/m·K, ρ = 7800 kg/m^3, c_p = 500 J/kg·K). Figure 1 (a) contains the pulses' basis function profile plots (purple to red curves) at their relative times, offset in space by the laser point-to-point distance (60 µm). The profiles demonstrate the basis function's temperature magnitude decreases, and its waist increases after the exposure time as heat conducts away from the exposure location. Adding the pulses' temperatures at a particular spatial point produces that location's total temperature. Figure 1 (a) shows the final superposition result by a profile plot (black curve) from the 2D temperature map in Figure 1 (b).

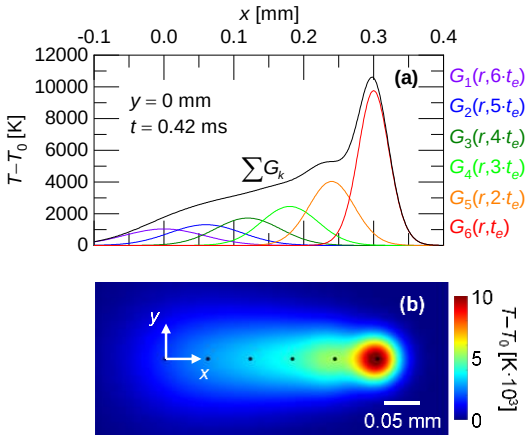

Figure 1. (a) Theoretical laser pulse basis function profiles with resulting superposition temperature and (b) 2D temperature map with coordinate system and exposure points.

A matrix algebra approach equivalently provides the superposition results in Figure 1. Equation 4 in matrix notation is

$$\vec{T} = T_0 + \boldsymbol{A}\vec{G}, \tag{6}$$

where $\vec{T}$ is the temperature vector, $\boldsymbol{A}$ is a matrix tracking the active basis function components for each (x, y, t), and $\vec{G}$ is the basis function vector. The laser's scan path and relative exposure time information build $\boldsymbol{A}$. Inverting Eq. 6 solves for an unknown basis function by utilizing known scan pathing and spatiotemporal temperature data like Figure 1 (b). The temperature data's samplings in space and time can provide, but do not limit, the inverted basis function's radial and temporal resolutions. Equation 6's inversion yields $\vec{G}$ exactly for theoretical cases with a full rank $\boldsymbol{A}$.

3. EXPERIMENTAL BASIS FUNCTION INVERSION

A SWIR camara observing a Renishaw AM250 (pulsed laser) rastering a 5×5 mm^2, 50 µm thick, 304L stainless steel layer provides the spatiotemporal thermal data for basis function inversion. The camera samples at 3345.8 Hz with 130 µm/pixel and 135 µm/pixel *x* and *y* instantaneous field of views, respectively (see [8] for further details). The raw camera data calibrates to temperature using a procedure like [9]. Figure 2 (a) shows a calibrated image with the laser's exposure points (white dots) and parameters annotated. The laser scans with a 0° rotation angle, a 60 µm point-to-point distance, d_p, and an 85 µm hatch spacing, d_h. Each image supplies an $\boldsymbol{A}$ sub-matrix and a $\vec{T}$ sub-vector. Since $\boldsymbol{A}$'s columns must equal $\vec{G}$'s length, the procedure builds $\boldsymbol{A}$ sub-matrices

by assuming $\vec{G} \to 0$ after 10 ms, or beyond a radius of 0.78 mm. Also, the process assumes $\vec{G}$ has resolutions of Δt = 150 µs and Δr = 130 µm. Data from 500 consecutive thermal images assemble $\boldsymbol{A}$ and $\vec{T}$ to invert $\vec{G}$. Multiple images provide a full rank $\boldsymbol{A}$ and reduce $\vec{G}$'s noise. Least squares produces $\vec{G}$ with minimum error by

$$\vec{G} = \left(\boldsymbol{A}^T \boldsymbol{A}\right)^{-1} \boldsymbol{A}^T \left(\vec{T} - T_0\right) \tag{7}$$

Figure 2 (b-d) contain the experimental basis function. The basis function's temperature magnitude decreases with increasing radius. For each radial component, the basis function's temperature magnitude quickly reaches a maximum, and then decreases with increasing time. Sampling rate variances and scan path location uncertainty cause the basis function's noise. The inversion success reveals the SWIR temperature data's linearity.

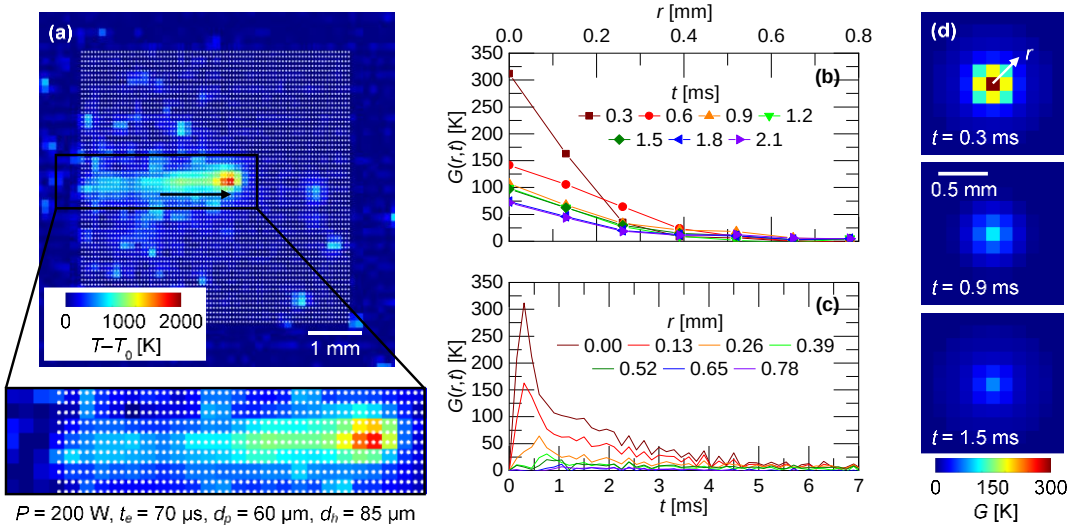

Figure 2. (a) SWIR melt pool image with laser exposure points and experimental basis function (b) plotted as a function of radius for various times, (c) plotted as a function of time for all radial components, and (d) mapped for various times.

4. SIMULATION RESULTS

The superposition model simulates the LPBF temperature field the SWIR camera measures by applying the experimental basis function in Eq. 6. The model predicts the 5×5 mm^2 layer's thermal history in 4 minutes (Dell OptiPlex 5050, Intel Core i-7700 CPU, 3.6 GHz). Figure 3 compares the superposition predictions with the layer's experimental temperature results. Figure 3 (a-c) show selected pixels' temporal data relative to their respective times at experimental maximum temperature. The data in Figure 3 (a-c) illustrate thermal history differences arise when the laser progresses from a corner to the raster's middle. The superposition simulation predicts those differences with the root mean square errors (RMSE) annotated on Figure 3 (a-c). The melt pool images in Figure 3 (d-f) demonstrate the spatial temperature agreement between the experiment's measurements and the simulation's predictions.

Thermal features capture the layer's entire thermal history by compressing each pixels' temporal data to a single metric. This process produces a thermally based data map for layers. Thermal features have application in part property correlations and in-situ defect detection. A layer's thermal feature map also clearly show how the laser's scan path affects the thermal history. Two common thermal features are the maximum temperature [10] and the time above threshold [11]. Figure 4 evaluates the superposition simulation's predictions of those thermal features. Figure 4 contains experimental and simulated thermal feature profile plots and maps. The maximum temperature, T_{max}, predictions in Figure 4 (a) and (c) match the experiments in the interior but deviate at the layer's edges. This suggests a linearity reduction where the laser corners. The entire

layer's maximum temperature RMSE is 177 K. Figure 4 (b) and (d) illustrate the simulation successfully predicts the experimental time above threshold, τ. Time above threshold experimental deviations occur at some locations due to balling. The time above threshold prediction has a 1.2 ms RMSE.

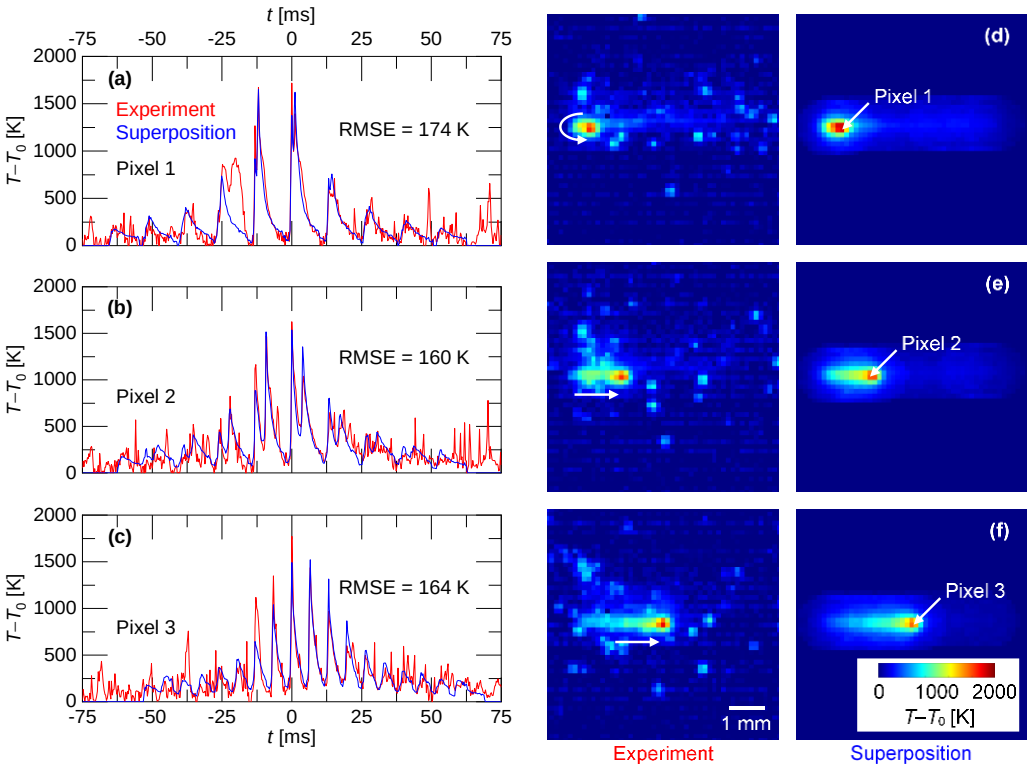

Figure 3. Experiment and superposition simulation (a,b,c) temperature histories and (d,e,f) melt pool images for various locations along a laser raster in the 5×5 mm^2 layer.

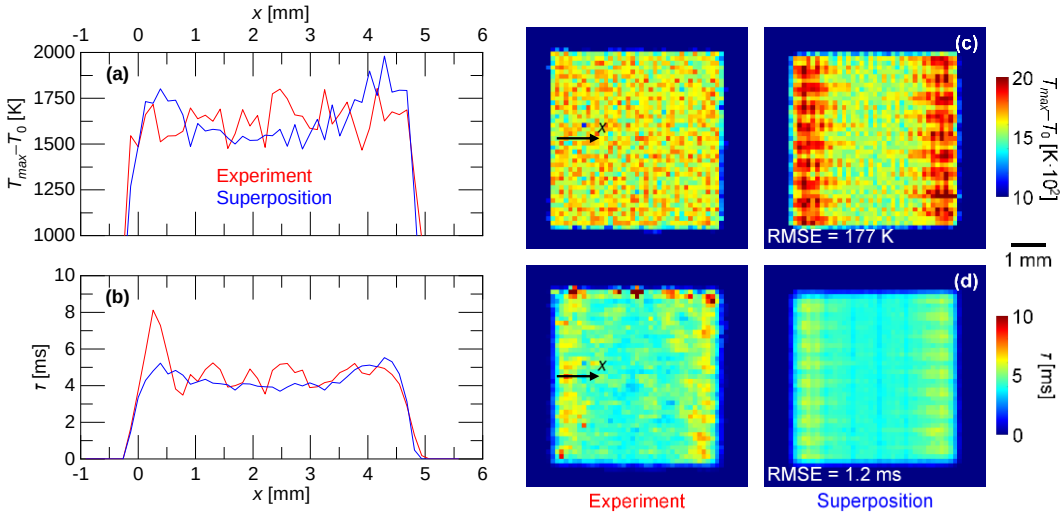

Figure 4. Experiment and superposition (a) maximum temperature and (b) time above threshold profile plots from 2D (c) maximum temperature and (d) time above threshold maps.

5. CONCLUSIONS

Inverting a basis function (i.e. the temperature response from a single laser pulse) from SWIR camera data enables experiment-based superposition thermal modeling for LPBF. The successful basis function inversion demonstrates the SWIR camera temperature data's linearity for nominal manufacturing. The superposition approach simulates a simple 5×5 mm^2 layer in 4 minutes. The simulation's analyzed time series data fits the experiment's data with a maximum 174 K RMSE. Simulation thermal features track experimental results with a 177 K maximum temperature RMSE and a 1.2 ms time above threshold RMSE. The pulsed laser experimental superposition framework should adapt to CW LPBF systems since thermal cameras have finite sampling rates. The superposition model's applications include laser scan path effects prediction to baseline

experimental data in part qualification, and feedforward controls. Future work will explore experimental superposition for various LPBF manufacturing cases and evaluate the ability to flag defects in parts.

ACKNOWLEDGMENT

This work was funded by Honeywell Federal Manufacturing & Technologies under Contract No. DE-NA0002839 with the U.S. Department of Energy. The United States Government retains and the publisher, by accepting the article for publication, acknowledges that the United States Government retains a nonexclusive, paid up, irrevocable, world-wide license to publish or reproduce the published form of this manuscript, or allow others to do so, for the United States Government purposes.

REFERENCES

[1] Druzgalski CL, Ashby A, Guss G, King WE, Roehling TT, Matthews MJ. Process optimization of complex geometries using feed forward control for laser powder bed fusion additive manufacturing. Addit Manuf 2020;34:101169. https://doi.org/10.1016/j.addma.2020.101169.

[2] Ning J, Sievers DE, Garmestani H, Liang SY. Analytical modeling of part porosity in metal additive manufacturing. Int J Mech Sci 2020;172:105428. https://doi.org/10.1016/j.ijmecsci.2020.105428.

[3] Bruna-Rosso C, Demir AG, Previtali B. Selective laser melting finite element modeling: Validation with high-speed imaging and lack of fusion defects prediction. Mater Des 2018;156:143–53. https://doi.org/10.1016/j.matdes.2018.06.037.

[4] Khairallah SA, Anderson AT, Rubenchik A, King WE. Laser powder-bed fusion additive manufacturing: Physics of complex melt flow and formation mechanisms of pores, spatter, and denudation zones. Acta Mater 2016;108:36–45. https://doi.org/10.1016/j.actamat.2016.02.014.

[5] Moran TP, Li P, Warner DH, Phan N. Utility of superposition-based finite element approach for part-scale thermal simulation in additive manufacturing. Addit Manuf 2018;21:215–9. https://doi.org/10.1016/j.addma.2018.02.015.

[6] Schwalbach EJ, Donegan SP, Chapman MG, Chaput KJ, Groeber MA. A discrete source model of powder bed fusion additive manufacturing thermal history. Addit Manuf 2019;25:485–98. https://doi.org/10.1016/j.addma.2018.12.004.

[7] Mishra AK, Aggarwal A, Kumar A, Sinha N. Identification of a suitable volumetric heat source for modelling of selective laser melting of Ti6Al4V powder using numerical and experimental validation approach. Int J Adv Manuf Technol 2018;99:2257–70. https://doi.org/10.1007/s00170-018-2631-4.

[8] Lough CS, Wang X, Smith CC, Landers RG, Bristow DA, Drallmeier JA, et al. Correlation of SWIR imaging with LPBF 304L stainless steel part properties. Addit Manuf 2020;35:101359. https://doi.org/10.1016/j.addma.2020.101359.

[9] Lane B, Moylan S, Whitenton EP, Ma L. Thermographic measurements of the commercial laser powder bed fusion process at NIST. Rapid Prototyp J 2016;22:778–87. https://doi.org/10.1108/RPJ-11-2015-0161.

[10] Krauss H, Zeugner T, Zaeh MF. Layerwise monitoring of the Selective Laser Melting process by thermography. Phys Procedia 2014;56:64–71. https://doi.org/10.1016/j.phpro.2014.08.097.

[11] Mohr G, Altenburg SJ, Ulbricht A, Heinrich P, Baum D, Maierhofer C, et al. In-situ defect detection in laser powder bed fusion by using thermography and optical tomography—comparison to computed tomography. Metals (Basel) 2020;10. https://doi.org/10.3390/met10010103.

SECTION

2. CONCLUSIONS

This dissertation establishes in-situ inspection methods for metal Laser Powder Bed Fusion Additive Manufacturing. Optical Emission Spectroscopy (OES) was performed for LPBF by collecting signal through the laser beam path. The spectra measured during laser melting 304L stainless steel correlates with the melt pool size. The OES framework also demonstrates that spectra strongly depend on the build chamber's atmospheric conditions including pressure and composition. Thermal features extracted from Short-Wave Infrared (SWIR) data correlate with bulk properties of 304L stainless steel. The SWIR thermal feature voxel based data for parts can successfully predict their local porosity using a probability mapping but this occurs with high false positive rates. Multiple SWIR thermal features provide improved correlation and prediction capabilities. Finally, superposition thermal modeling based on experimental SWIR data is achieved. The model predicts the effects laser scan pathing has on the thermal history for application in LPBF process correction.

BIBLIOGRAPHY

[1] W.E. King, A.T. Anderson, R.M. Ferencz, N.E. Hodge, C. Kamath, S.A. Khairallah, A.M. Rubenchik, Laser powder bed fusion additive manufacturing of metals; physics, computational, and materials challenges, Appl. Phys. Rev. 2 (2015) 041304. https://doi.org/10.1063/1.4937809.

[2] L. Scime, J. Beuth, Melt pool geometry and morphology variability for the Inconel 718 alloy in a laser powder bed fusion additive manufacturing process, Addit. Manuf. 29 (2019) 100830. https://doi.org/10.1016/j.addma.2019.100830.

[3] A. Leicht, P. Camille, M. Rashidi, U. Klement, N. Lars, E. Hryha, Effect of part thickness on the microstructure and tensile properties of 316L parts produced by laser powder bed fusion, Adv. Ind. Manuf. Eng. 2 (2021) 100037. https://doi.org/10.1016/j.matchar.2020.110309.

[4] A. du Plessis, X-ray tomography for the advancement of laser powder bed fusion additive manufacturing, J. Microsc. 00 (2020) 1–10. https://doi.org/10.1111/jmi.12930.

[5] T.H. Becker, N.M. Dhansay, Influence of porosity on the fatigue life of laser powder bed fusion–produced Ti6Al4V, Mater. Des. Process. Commun. 3 (2021) 1–7. https://doi.org/10.1002/mdp2.141.

[6] M. Grasso, B.M. Colosimo, Process defects and in situ monitoring methods in metal powder bed fusion: A review, Meas. Sci. Technol. 28 (2017). https://doi.org/10.1088/1361-6501/aa5c4f.

[7] H. Krauss, T. Zeugner, M.F. Zaeh, Layerwise monitoring of the Selective Laser Melting process by thermography, Phys. Procedia. 56 (2014) 64–71. https://doi.org/10.1016/j.phpro.2014.08.097.

[8] C.S. Lough, X. Wang, C.C. Smith, R.G. Landers, D.A. Bristow, J.A. Drallmeier, B. Brown, E.C. Kinzel, Correlation of SWIR imaging with LPBF 304L stainless steel part properties, Addit. Manuf. 35 (2020) 101359. https://doi.org/10.1016/j.addma.2020.101359.

[9] G. Mohr, N. Scheuschner, K. Hilgenberg, In situ heat accumulation by geometrical features obstructing heat flux and by reduced inter layer times in laser powder bed fusion of AISI 316L stainless steel, Procedia CIRP. 94 (2020) 155–160. https://doi.org/10.1016/j.procir.2020.09.030.

[10] M.M. Collur, T. Debroy, Emission spectroscopy of plasma during laser welding of AISI 201 stainless steel, Metall. Mater. Trans. B. 20 (1989) 277–286. https://doi.org/10.1007/BF02825608.

[11] C.B. Stutzman, A.R. Nassar, E.W. Reutzel, Multi-sensor investigations of optical emissions and their relations to directed energy deposition processes and quality, Addit. Manuf. 21 (2018) 333–339. https://doi.org/10.1016/j.addma.2018.03.017.

[12] J. Shin, J. Mazumder, Composition monitoring using plasma diagnostics during direct metal deposition (DMD) process, Opt. Laser Technol. 106 (2018) 40–46. https://doi.org/10.1016/j.optlastec.2018.03.020.

[13] W. Ren, J. Mazumder, In-situ porosity recognition for laser additive manufacturing of 7075-Al alloy using plasma emission spectroscopy, Sci. Rep. 10 (2020) 1–11. https://doi.org/10.1038/s41598-020-75131-4.

[14] A.J. Dunbar, A.R. Nassar, Assessment of optical emission analysis for in-process monitoring of powder bed fusion additive manufacturing, Virtual Phys. Prototyp. 13 (2018) 14–19. https://doi.org/10.1080/17452759.2017.1392683.

[15] P.W. Tse, G. Wang, Sub-surface defects detection of by using active thermography and advanced image edge detection, J. Phys. Conf. Ser. 842 (2017). https://doi.org/10.1088/1742-6596/842/1/012029.

[16] G. Mohr, S. Nowakowski, S.J. Altenburg, C. Maierhofer, K. Hilgenberg, Experimental determination of the emissivity of powder layers and bulk material in laser powder bed fusion using infrared thermography and thermocouples, Metals (Basel). 10 (2020) 1–36. https://doi.org/10.3390/met10111546.

[17] J.C. Heigel, B.M. Lane, Measurement of the Melt Pool Length during Single Scan Tracks in a Commercial Laser Powder Bed Fusion Process, J. Manuf. Sci. Eng. Trans. ASME. 140 (2018) 1–7. https://doi.org/10.1115/1.4037571.

[18] J.C. Heigel, E. Whitenton, Measurement of thermal processing variability in powder bed fusion, Proc. - 2018 ASPE Euspen Summer Top. Meet. Adv. Precis. Addit. Manuf. 69 (2018) 242–247.

[19] B. Liu, G. Fang, L. Lei, An analytical model for rapid predicting molten pool geometry of selective laser melting (SLM), Appl. Math. Model. 92 (2021) 505–524. https://doi.org/10.1016/j.apm.2020.11.027.

[20] S.A. Khairallah, A.T. Anderson, A. Rubenchik, W.E. King, Laser powder-bed fusion additive manufacturing: Physics of complex melt flow and formation mechanisms of pores, spatter, and denudation zones, Acta Mater. 108 (2016) 36–45. https://doi.org/10.1016/j.actamat.2016.02.014.

[21] Y. Li, D. Gu, Thermal behavior during selective laser melting of commercially pure titanium powder : Numerical simulation and experimental study &, Addit. Manuf. 1–4 (2014) 99–109. https://doi.org/10.1016/j.addma.2014.09.001.

[22] E.J. Schwalbach, S.P. Donegan, M.G. Chapman, K.J. Chaput, M.A. Groeber, A discrete source model of powder bed fusion additive manufacturing thermal history, Addit. Manuf. 25 (2019) 485–498. https://doi.org/10.1016/j.addma.2018.12.004.

[23] T.P. Moran, P. Li, D.H. Warner, N. Phan, Utility of superposition-based finite element approach for part-scale thermal simulation in additive manufacturing, Addit. Manuf. 21 (2018) 215–219. https://doi.org/10.1016/j.addma.2018.02.015.

VITA

Cody Shannon Lough was born in Rolla, Missouri. He graduated with a Bachelor of Science in Mechanical Engineering from Missouri University of Science and Technology in May 2017. As an undergraduate, he researched thermal modeling of Laser Powder Bed Fusion and active spatiotemporal thermography under the direction of Dr. Edward C. Kinzel. This experience led him to pursue a PhD in Mechanical Engineering under Dr. Kinzel at Missouri University of Science and Technology. In his graduate research, he developed in-situ inspection methods for Laser Powder Bed Fusion. He obtained his Doctor of Philosophy in Mechanical Engineering from Missouri S&T in May 2021.